공학박사 학위논문

Tailoring martensitic transformation behavior in TiCu-based super-elastic alloys and their composites

TiCu계 초탄성 합금 및 복합재의 마르텐사이트 상변태 거동 제어

2018년 1월

서울대학교 대학원

재료공학부

류 욱 하

Tailoring martensitic transformation behavior in TiCu-based super-elastic alloys and their composites

TiCu계 초탄성 합금 및 복합재의
마르텐사이트 상변태 거동 제어

지도교수 박 은 수

이 논문을 공학박사 학위논문으로 제출함
2018년 1월

서울대학교 대학원
재료공학부
류 욱 하

류욱하의 공학박사 학위논문을 인준함
2018년 1월

위 원 장 _____ 주 영 창 _____ (인)

부위원장 _____ 박 은 수 _____ (인)

위   원 _____ 김 도 향 _____ (인)

위   원 _____ 한 흥 남 _____ (인)

위   원 _____ 염 종 택 _____ (인)

Abstract

Tailoring martensitic transformation behavior in TiCu-based super-elastic alloys and their composites

Wookha Ryu

Department of Materials Science and Engineering

College of Engineering

Seoul National University

Shape memory alloys (SMAs) have opened up an area of new material called multifunctional materials representing sensing and actuation capabilities. SMAs can be utilized for various applications according to temperature, stress field and magnetic field change by utilizing reversible martensitic phase transformation. One of the modes, superelasticity, that utilize the martensitic phase transformation is to lower the phase transformation temperature than the operating environment, so that the forward martensitic phase transformation occurs when the stress is applied and the reverse martensitic phase transformation occurs when the stress is relaxed. Recently, It have attracted great interest in research that inducing work hardening behavior and improvement of toughness into bulk metallic glass by precipitating a superelastic secondary phase, and utilizing the elastic calorie effect through the release and absorption of latent heat generated during the martensitic phase transformation. However, there are few studies on the development of new

superelastic alloys with optimized characteristics. Most of the reports are mainly focused on the application of conventional alloys. Since an alloy system exhibiting reversible martensitic phase transformation mainly forms an intermetallic compound phase, superelastic alloys can be manufactured only in a few specific alloy systems such as NiTi, CuZn, and NiMgGa, and the solubility of the third and fourth alloying elements is very limited. In this study, in order to overcome the limitation of the alloy design, we devised a method to expand the solid solution limit of the superelastic phase (B2, BCC, etc.) reported on the known phase diagram. The phase showing reversible martensitic phase transformation is mostly stable at high temperatures, and precipitates tend to occur as the alloy system becomes complicated. When precipitates are suppressed, and primary phase is stabilized, the superelastic alloy can be produced in an extended composition range. In the NiTiCu alloy system, which is known to be possibly used as an elastocaloric material and amorphous matrix composite, it has been found that the addition of a small amount of Si can effectively inhibit the precipitation of superfine B2 phase and other intermediate compound phases. In particular, as the Cu content increases, the amount of energy dissipation due to the internal friction occurring during the phase transformation of martensite is reduced, which is advantageous for the superelastic characteristics. We aimed to maximize the Cu content in B2 phase. As a result, it was confirmed that superelastic B2 alloys can be manufactured by employing Cu up to "43 at. %", and shows very low hysteresis and mechanical energy dissipation during the phase transformation. In order to utilize the TiCuNiSi superelastic alloy, it is essential to optimize the phase transformation temperature and mechanical properties. In this study, we tried to control the phase

transformation temperature by adding Sn element which is known to decrease the phase transformation temperature of Ti alloys. The Sn element was employed up to 5 at. %, which showed a sharp increase in strength, unlike the general solid solution hardening phenomenon. First principle calculations have confirmed that the mechanism is hardening effect by antisite defect, and compared with general solid solution hardening theory. The change of phase transformation temperature due to solid solution hardening is closely related to the change of yield strength. Especially, the correlation between critical stress for martensitic transformation and yield strength was investigated. It is suggested that the temperature and strength of TiCuNiSiSn superalloy can be easily controlled through the correlation between alloy composition and antisite defect hardening. The alloying composition of TiCuNiSiSn alloy system was designed to show the excellent elastocaloric effect through the process of controlling the temperature of the phase transformation. The coefficient of performance and fatigue characteristics were analyzed. As a result, the alloys developed through this study showed the most efficient elastocaloric effect than all the superelastic alloy systems reported so far.

The TiCuNiSiSn alloys with high Cu contents are capable of producing bulk metallic glass and confirmed that bulk metallic glass with a maximum diameter of 4 mm or more can be produced by adding elements such as Zr and Nb. We also developed a composite material with a bulk metallic glass as a matrix and a superelastic alloy as a second phase, and modulated the volume fraction of the second phase by controlling quenching rate. In addition, the enhancement of the mechanical properties of the amorphous matrix composites was found to be due to the increase of the work hardening ability of the second phase by applying the solid

solution hardening by antisite defect caused by Sn addition. As a result, bulk metallic glass matrix composite materials having high yield strength and excellent work hardening ability of about 1 GPa or more were developed.

In this paper, we present a unique alloy design method and theoretical considerations that have not been attempted. We have extended the maximum solid solubility limit of alloying element in B2 phase, and proposed a method to control the characteristic temperature of martensitic transformation and mechanical properties of SMAs. In addition, it is considered that this work has an important meaning not only in the academic aspect but also in the industry as well, by developing a material having excellent elastocaloric performance and an excellent mechanical property. Especially, since the B2 phase stability can be enhanced by suppressing precipitations, it will be the core technology that will lead the fourth industrial revolution by utilizing sputtering and 3-D printing. The same concept of alloy design can be applied to other alloy systems as well as the TiCuNi alloy system proposed in this paper, which can be used as a guideline for further study.

Table of Contents

List of Figures

composition of $(Ti_{51}Cu_{41}Ni_7Si_1)_{100-x}Sn_x$ (x=1, 2, 3, 4, and 5 at.%). With increasing Sn contents, stress-strain curves systematically changes depending on the martensite transformation related characteristics such as transformation stress (σ_{Ms}, first yielding) and yield stress B19 martensite phase (σ_y, second yielding). (b) In-situ neutron diffraction spectra of as-cast $(Ti_{51}Cu_{41}Ni_7Si_1)_{98}Sn_2$ cylindrical specimen having a diameter of 3 mm under uniaxial compressive loading.

or 1.94(this work).

amount of maximum change of temperature is saturated, in which the sample is considered to be under quasi-adiabatic condition.

according to the loading direction.

metallic glass matrix composite by stress induced martensitic transformation of polymorphically precipitated B2 secondary phases. Uniaxial compression test conducted on the as-cast 2mm rod sample.

List of Tables

Chapter 1.

Introduction

1.1. Shape memory effect and Superelasticity

Shape memory effect (SME) is a phenomenon that a deformed alloy to recover the original shape at the high temperature over characteristic temperature of martensitic phase transformation. Shape memory alloys (SMAs) exhibit shape memory effect by the change of temperature, stress or magnetic field[1-4]. Superelasticity (SE) takes place by reversible stress-induced martensitic transformation (MT) at a temperature higher than the characteristic temperature. Superelastic alloys (SEAs) recover strains induced by stress field during unloading of the material [1-10]. SME and SE are a consequence of reversible MT, which are described in Fig. 1.1. MT is a solid to solid diffusion-less phase transformation from austenite, a high temperature stable phase, to martensite, a low temperature stable phase, upon cooling, inducing of magnetic field, or loading of the material, as depicted in Fig 1.2. During MT, the alloying atoms in the unit cell undergo a shuffling of a specific atomic plane, shear movement along certain direction, for a short distance. Generally, the crystal structure of the austenite is cubic, but that of martensite is diverse, which is cubic, hexagonal, monoclinic, orthorhombic, rhombohedral, etc. The larger the difference between the structure of the martensite phase and the structure of the austenite phase, the larger the entropy difference at the phase transformation. The transformation strain induced from the formation of martensite in austenite depends on the difference in the lattice structure, lattice

parameters. In SMA systems, the transformation strain is originated from formation and movement of twin boundaries in martensite phase. Under stress free condition, twinned martensite structure consisting of several different pairs of martensite variants forms. The number of the pair of martensite variants depends on the crystallographic relationship between austenite and martensite. For instance, there are 6 lattice (3 pairs) correspondence variants for B2 (ordered BCC) austenite to B19 (orthorhombic) MT [12]. Each martensite variant has a different crystallographic relationship with the austenite phase and the variant pairs can minimize the lattice misfit induced from the lattice structure difference between austenite and martensite. The larger the lattice misfit, the finer the martensite variant pairs, and the interface between variant pair have twin structure to minimize formation energy of martensite phase. Therefore, there is no macroscopic transformation strain induced by MT under stress free condition, due to the formation of a number of self-accommodated pairs of martensite variants. However, in the case of MT under external stress is applied, energetically favorable variant is preferentially generated rather than the other orientation of variants. The favorable variant induces a macroscopic transformation strain in the shape memory effect and superelasticity. Fig. 1.1 shows the MT driven by the change of temperature or application of stress field. The austenite phase transforms to self-accommodated martensite, which is twinned martensite with different pairs of variants, upon cooling and it transforms to detwinned martensite under stress field. By heating, detwinned martensite transforms to austenite and at the conditions where there is no external application of stress, the austenite will go back to self-accommodated twinned martensite structure by cooing.
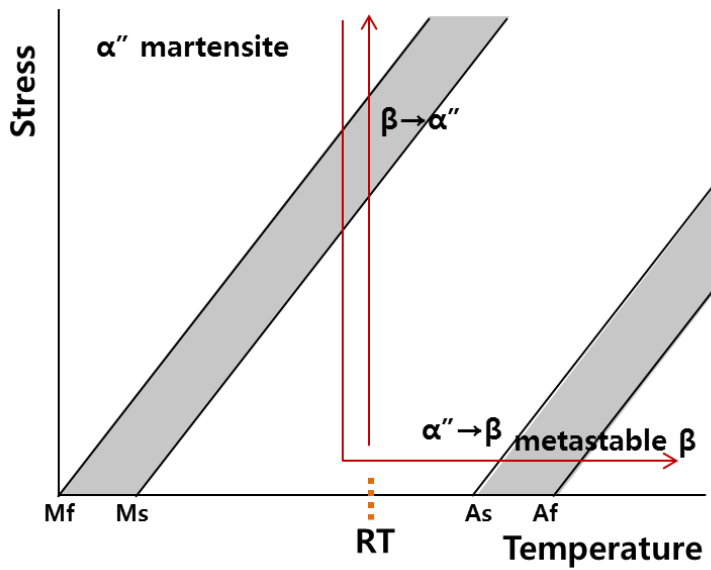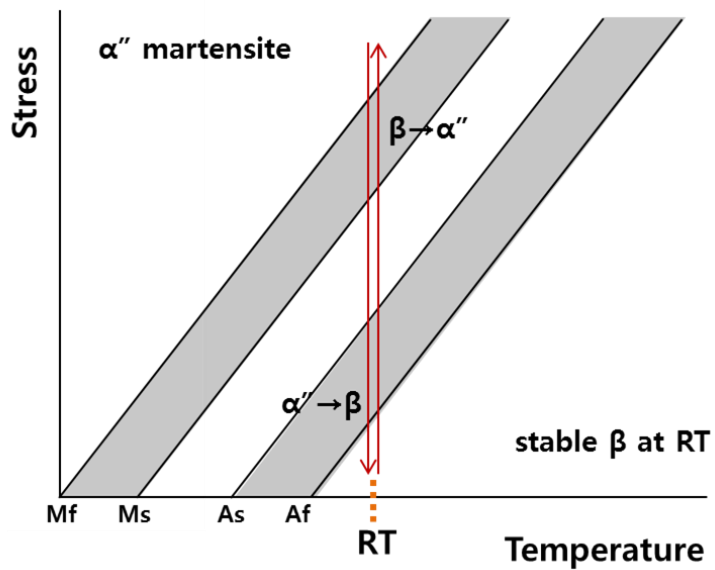
Fig. 1.1. Demonstration of a $\sigma - T$ phase diagram of an SMA for a martensitic transformation. The material is fully austenite above A_f and fully martensite below M_f.
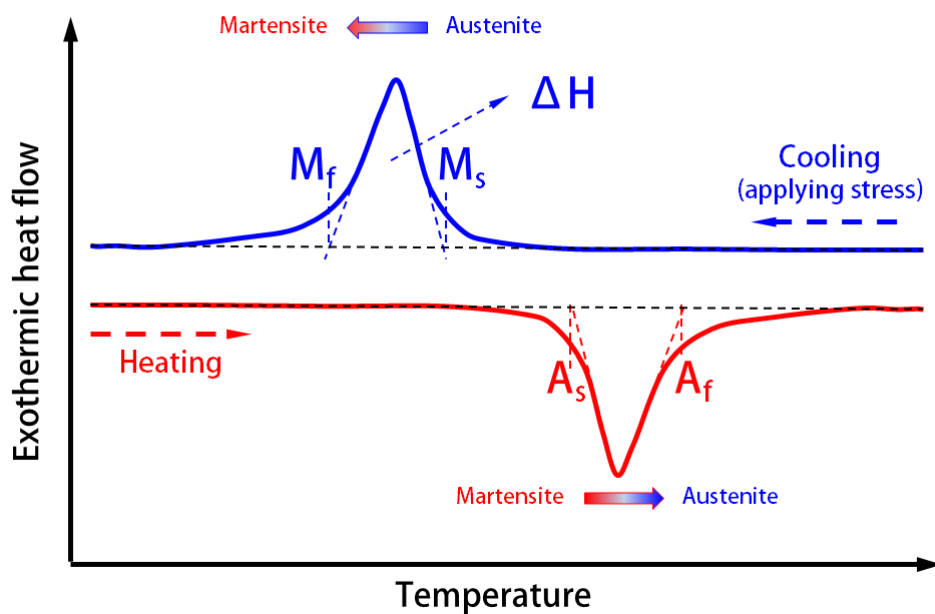
Fig. 1.2. A schematic illustration of heat flow vs. temperature curves. High temperature stable austenite phase can be transformed into low temperature stable martensite phase by cooling of applying stress. The reverse transformation occurs by heating of releasing stress.

The MT in SMAs takes place over at a certain temperature and applied stress. The temperature where austenite starts to transform into martensite is defined as martensite start temperature, M_s. The temperature in which the forward MT is completed, is defined as the martensite finish temperature, M_f. For the reverse transformation, from martensite to austenite phase, the temperature where austenite starts and complete to form is the austenite start temperature, A_s, and the austenite finish temperature, A_f. The four characteristic temperatures have a linear correlation with applied stress, known as the Clausius-Clapeyron relationship. If the Claisus-Clapeyron relationship for all transformation temperatures is drawn in the σ – T diagram, the phase diagram of the SMA SEA is generated. Such examples of phase diagrams are shown in Fig. 1.1., which also describe the deformation behavior of the SMA and SEA as a function of pressure. The self-accommodated twinned martensite varinats undergo detwinning (reorientation of martensite variants) to a monolithic variant by applying stress at a temperature below M_f. When the stress released, the detwinned monolithic variant tends to maintain the reoriented state while still keeping macroscopic shape. Following heating over A_f, and subsequent cooling below M_f, the martensite phase go back to self-accommodated twinned structure in stress free conditions (Fig. 1.1) and the alloy recover the original macroscopic shape by the SME. If an SMA deformed to a certain strain level at a temperature above A_f, the material exhibits a stress-induced MT. When the applied stress released, the material transform back to the austenite phase and recover its original macroscopic shape in the case of no plastic deformation. This is the deformation mechanism of superelasticity.

1.2. Characteristics of shape memory alloys

In recent years, there is a growing demand for SMA development for smart systems that can be used in complex operating environments [2,3]. It has been reported in the literature that shape memory alloys (SMAs) have been used widely in various fields such as actuators [11, 12]. For the applications, the martensitic transformation (MT) characteristics such as transformation temperature, stress, hysteresis and interval should be carefully managed. For instance, small temperature hysteresis and large transformation interval are favorable for microelectromechanical systems (MEMS) actuator materials [13]. In addition, large transformation intervals are preferred in practical applications, because the deformation process is more often controlled by load than displacement. For small deformation intervals, the material can be deformed in an unstable manner over the range of the MT [5]. It is also essential to make the securance of the mechanical properties and fatigue according to operating conditions. In particular, a high work output induced by MT can be achieved when working in high pressure environment, development of SMAs that can be operated at ultra-high pressure of 1 GPa or more has attracted increasing attention recently. Another point of interest is the material cost. In the case of the NiTi-based alloys, high strength, functionally stable SMAs have recently been successfully developed with expensive substitution elements of Pd, Pt, Au, Hf, Nb or Zr, , which is considered to be a limitation in terms of commercialization. The Cu-based SMAs, such as CuZnAl, have advantages of low cost, but due to limitations of mechanical properties, there are restrictions on application in various environments such as high temperature and high pressure. Therefore, in order to promote the commercialization of SMA, it

is necessary to develop a novel alloy system containing a large amount of low-cost elements such as Cu and exhibiting excellent phase transformation characteristics and mechanical properties. However, it is limited to develop a SMA with new composition. Most of the investigations on SMAs are based on known phase diagrams in systems based on alloy systems developed in the 1960s and 1970s, which are listed in Table 1.1.

Table. 1. Binary alloy systems forming shape memory alloys

Austenitic phase	System	M_s (K)
Ordered BCC	NiAl	456
	NiMn	967
	RuNb	1158
	RuTa	1403
	AgCd	199
	AuCd	337
	TiPd	818
	TiNi (1960s~)	**320**
	ZrRh	753
	CuZr	413
	AgZn	136
	CuZn (1950s~)	**222**
	Cu3Sn	164
	Fe3Al	-
Disordered BCC	TiNb	315
	TiTa	673
	CuAl	650
	UNb(tet)	410
	UNb(mono)	490
FCC	Fe3Pt	77
	CoAl	373
	CoNi	535
	FeMn	431
	FeNi	243
	FeRu	650
	FePd	268
	MnCu	260
	InCd	353
	InPb	254
	InTl	299

1.2.1. Martensite start temperature

SMAs have the potential to be used in high and cryogenic temperature environments by controlling the martensite start temperature (M_s). Since M_s is sensitive to alloy composition, extensive research has been carried out to modulate M_s through alloy design. Through these efforts, factors such as shear modulus [4-6], valence electron (shown in Fig. 1.3) [7,8] and latent heat [9] have been investigated to have a significant correlation with compositional dependence of M_s. However, the correlations have not been widely utilized in development of new alloys. Currently, the conventional SMA developments based on trial and error without the theoretical background is faced with the challenge of designing new alloy composition. Commercial SMAs such as NiTi and Cu-based alloys have an ordered intermediate phase as an austenite. In this case, due to the crystal structure, the concentration of antisite defects (ASDs) and constitutional vacancies generated according to the site preference of the contained elements are closely correlated with the properties of the alloy [10-12]. Not surprisingly, it has been presumed that the concentration of point defects including ASD and vacancy is expected to have a great influence on the MT of SMAs. In this regard, Tehrani et al. presented ab initio calculations of M_s in equiatomic NiTi with different ASD or vacancy concentration [13]. However, since it is difficult to measure the exact defect concentration and the related theories are not understood, the detailed correlation has not been sufficiently investigated yet.
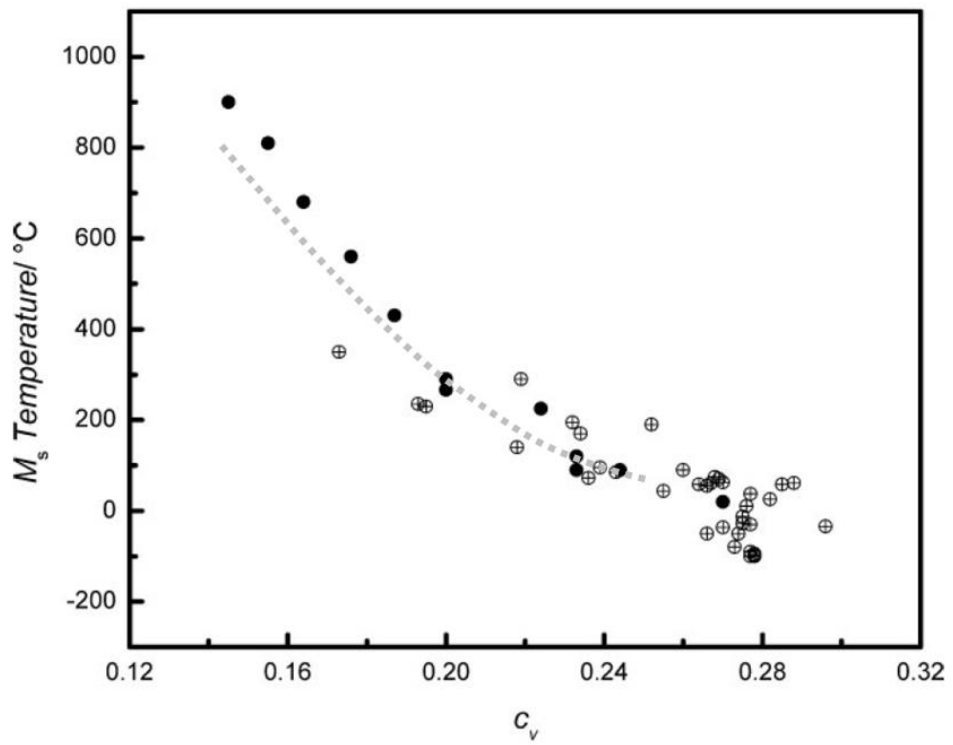
Fig. 1.3. Illustration of valence electron concentration (C_v) dependence of martensite start temperature (M_s).

1.2.2. Lattice structure

1.2.2.1. Transformation matrix

When phase transformation from B2 to B19 proceeds, lattice strain occurs through (110)[1-10] – (110)[-110] shuffling which are described in Fig 1.4. A tensile strain increases along the $[001]_{B19}$ direction, and compressive strain increases along the $[010]_{B19}$ and $[100]_{B19}$ directions. B2 and B19 have a crystallographic correlation as shown in Fig. 1.4. The $[001]_{B19}$, $[010]_{B19}$, and $[100]_{B19}$ axes correspond to the $[-110]_{B2}$, $[110]_{B2}$, and $[001]_{B2}$ axes, respectively. The transformation stretches α, β and γ have a relationship with the lattice parameters of the B2 and B19 phases as:

$\alpha = a_{B19}/a_{B2}$, $\beta = b_{B19}/(a_2\sqrt{2})$ and $\gamma = c_{B19}/(a_2\sqrt{2})$ where the lattice parameter of the B2 unit cell is a_{B2} and the lattice parameters of the B19 unit cell are a_{B19}, b_{B19} and c_{B19}. The transformation stretch includes crystallographic information about the lattice distortion occurring during the martensitic phase transformation. In particular, the volume change ($\Delta V / V = \alpha\beta\gamma$) can be calculated directly, and the transformation matrix $\mathbf{U}_i$ can be induced if all lattice parameters of both the austenite and the martensite phases can be obtained. Transformation matrixes of B2 to B19 transformation for the six martensite variants are :

$$U_1 = \begin{bmatrix} \beta & 0 & 0 \\ 0 & \dfrac{\alpha+\gamma}{2} & \dfrac{\alpha-\gamma}{2} \\ 0 & \dfrac{\alpha-\gamma}{2} & \dfrac{\alpha+\gamma}{2} \end{bmatrix}, U_2 = \begin{bmatrix} \dfrac{\alpha+\gamma}{2} & 0 & \dfrac{\alpha-\gamma}{2} \\ 0 & \beta & 0 \\ \dfrac{\alpha-\gamma}{2} & 0 & \dfrac{\alpha+\gamma}{2} \end{bmatrix}, U_3 = \begin{bmatrix} \dfrac{\alpha+\gamma}{2} & \dfrac{\alpha-\gamma}{2} & 0 \\ \dfrac{\alpha-\gamma}{2} & \dfrac{\alpha+\gamma}{2} & 0 \\ 0 & 0 & \beta \end{bmatrix},$$

$$U_4 = \begin{bmatrix} \beta & 0 & 0 \\ 0 & \dfrac{\alpha+\gamma}{2} & \dfrac{\gamma-\alpha}{2} \\ 0 & \dfrac{\gamma-\alpha}{2} & \dfrac{\alpha+\gamma}{2} \end{bmatrix}, U_5 = \begin{bmatrix} \dfrac{\alpha+\gamma}{2} & 0 & \dfrac{\gamma-\alpha}{2} \\ 0 & \beta & 0 \\ \dfrac{\gamma-\alpha}{2} & 0 & \dfrac{\alpha+\gamma}{2} \end{bmatrix}, U_6 = \begin{bmatrix} \dfrac{\alpha+\gamma}{2} & \dfrac{\gamma-\alpha}{2} & 0 & 0 \\ \dfrac{\gamma-\alpha}{2} & \dfrac{\alpha+\gamma}{2} & & 0 \\ 0 & 0 & & \beta \end{bmatrix}$$

which have the same ascendingly ordered eigenvalues of $\lambda_1 \leq \lambda_2 \leq \lambda_3$ [3]. We found all the pair of type 1 and type 2 twins whose middle eigenvalue of $\mathbf{C}(i,j)$ is 1 :

Type1 : $(U_1, U_2)_{[110]}$, $(U_4, U_5)_{[110]}$, $(U_2, U_6)_{[011]}$, $(U_3, U_5)_{[011]}$,

Type2 : $(U_2, U_4)_{[1\text{-}10]}$, $(U_1, U_5)_{[1\text{-}10]}$, $(U_2, U_3)_{[0\text{-}11]}$, $(U_5, U_6)_{[0\text{-}11]}$.
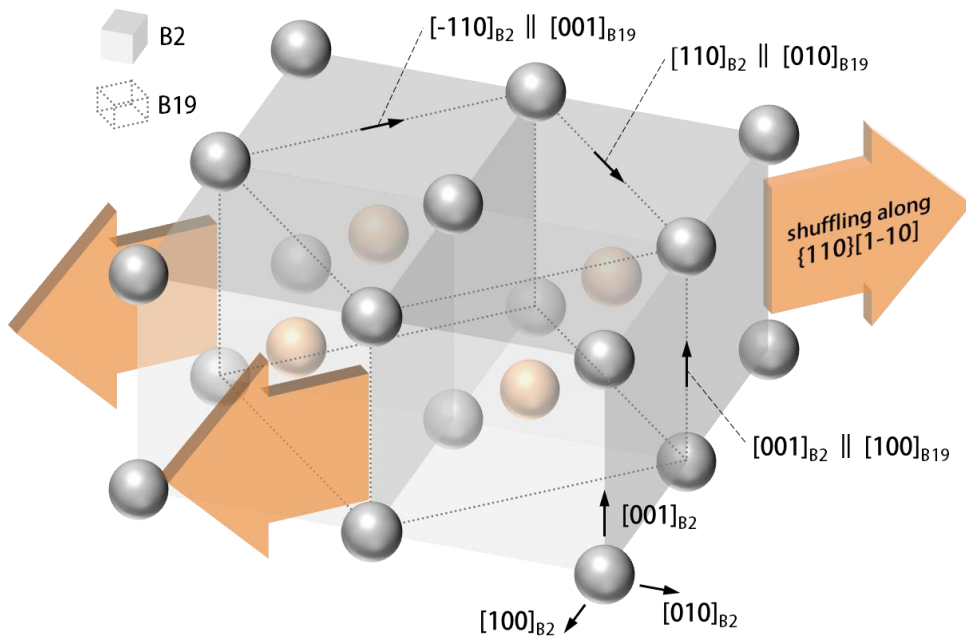
Fig. 1.4. Schematic description of the lattice shuffling during martensitic phase transformation from B2 to B19 structure.

1.2.2.2. Middle eigenvalue and cofactor condition

The NiTi-based SMA systems alloys with noble elements, such as Pd, Pt, and Au is known to have the feature of narrow hysteresis and excellent functional stability. The unique properties of low hysteresis in a very wide composition range in this alloy system seemed to be related to compatibility between austenite and martensite or between a pair of martensite variants. Therefore, the cofactor conditions were considered from the lattice parameters calculated by refinement of the XRD patterns. From the crystallographic theory of martensite, the geometrically plausible interface of austenite-martensite, or interface of different martensite variants have been investigated. The cofactor conditions[19], i.e.,

$\lambda_2 = 1$ Where 2 is the middle eigenvalue of transfotmation matrix, U,

$$\mathbf{a} \bullet \mathbf{U}\text{cof}(\mathbf{U}^2 - \mathbf{I})\mathbf{n} = 0,$$

$$\text{tr}\mathbf{U}^2 - \det\mathbf{U}^2 - \frac{|\mathbf{a}|^2|\mathbf{n}|^2}{4} - 2 \geq 0,$$

are the quantitative compatibility criteria using only lattice parameters of austenite and martensite phase. A simplified equivalent forms of the conditions are :

$$\lambda_2 = 1,$$

$$\text{XI:} = |\mathbf{U}^{-1}\hat{e}| = 1 \ \text{(type 1 twin)},$$

$$\text{XII:} = |\mathbf{U}\hat{e}| = 1 \ \text{(type 2 twin)},$$

where ê is a unit vector aligned with the twofold axes associated to the twins. ê is given by

$\hat{e} = \pm(\delta_1 \mathbf{U}_i \mathbf{v}_1 + \delta_3 \mathbf{U}_i \mathbf{v}_3)$, where $\delta_1 = (2(\mathbf{v}_1 \mathbf{U}_i^2 \mathbf{v}_1 + s\sqrt{\mu_3}\mathbf{v}_3 \mathbf{U}_i^2 \mathbf{v}_1))^{-1/2}$ and $\delta_3 = s\sqrt{\mu_3}\delta_1$, $s = \pm 1$. μ_3 is the largest eigenvalues of $\mathbf{C}(i,j) = \mathbf{U}_i^{-1}\mathbf{U}_j^2\mathbf{U}_i^{-1}$ [20].

By Yintao Song et al., the simplified equivalent forms of cofactor condition XI and XII can be calculated as follows. We need to measure the lattice parameters of austenite and martensite phase, and transformation matrix by the analysis of diffraction patterns. For a compatible MT, the accompanying structural change can be given by a 3 by 3 tensor, F which describes the structure change of unit cell of austenite to that of martensite, defined by lattice vectors in Fig 1.4. The stretch component of F can be extracted through polar decomposition, $\mathbf{F} = \mathbf{QU}$, where $\mathbf{Q}$ is a rotation tensor. U is called the transformation matrix related to a certain martensite variant. It is required to compute the transformation matrix U for the every distinct variant. For MT from B2 to B19, there are total 6 different variants and equivalent U. Certain two martensite variants, which are satisfying the twining relation ($\mathbf{QU}_j\text{-}\mathbf{U}_i=\mathbf{a}\otimes\mathbf{n}$, $\mathbf{Q}$ representing a rigid body rotation of variant j) is called twin pair. For the 6 different variants of B2 to B19 MT, there are 4 type I twin pairs and 4 type II twin pairs each, where types I and II refer to a certain crystallographic relations that having specific twin plane between each variant. The twinning axis $\hat{e}$ is calculated for each twin pair, and the XI and XII obtained by the equation, $X_I := |\mathbf{U}^{-1}\hat{e}|$, $X_{II} := |\mathbf{U}\hat{e}|$.

1.2.3. Transformation interval

Lüders-type deformation behavior is one of the most problematic aspects of practical application in utilizing SMAs. During stress-induced martensitic transformation, a flat stress plateau causes a serious instability of the system where the displacement cannot be effectively controlled by the load. In order to solve this problem, various functionally graded SMAs have been actively developed recently. Fabrication of microstructurally graded SMA through gradient annealing process and compositionally graded SMA through control of manufacturing process using powder metallurgy have been reported. The graded structures result in the variation of thermomechanical properties at different local region by creating a complex stress field that causes transformation strain at different levels of applied load. In the case of such a graded structure, since the composition or microstructure changes have directionality, the thermomechanical property also has a characteristic of being oriented.

1.2.4. Solid solution hardening

Most of SMAs are considered to have ordered crystal structure (intermetallic compounds). Ordered alloys are usually divided into three different groups according to their preference of defect types, triple defect (TRD), antisite defect (ASD), and hybrid type. For TRD type alloys, vacancy is considered to be a preferential defect rather than antisite defect. Therefore, relatively high concentration of vacancy is stable at cryogenic temperature. The theoretical minimum vacancy concentration for TRD alloys is 2x (x: compositional deviation from stoichiometry in atomic percent) as described by the Bradley-Taylor (BT) line in Fig 1.5. Similarly, the theoretical minimum antisite concentration for ASD alloys is x, as shown in Fig 1.5. A antisite defect in B sub-lattice site (A_B) can be generated in A-rich alloys. The effect of the point defects, ASD and TRD on the MT of SMAs has been interested for many decades. Especially, it has been reported that ASD has severe influence for NiTi SMAs. This was evidenced by the strong ASD dependence of M_s which can be varied either by alloy composition deviated from stoichiometry. In the representative SMA systems of CuZn, TiNi, etc. show several hundreds of M_s variation by only 1~2 at% change in composition. This can be considered as a common feature to many ordered alloys of B2 structure.
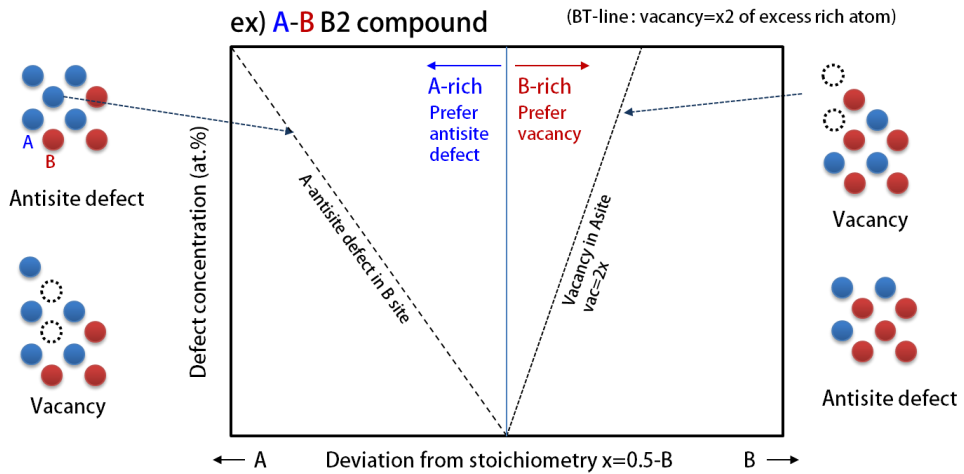
Fig. 1.5. Compositional dependence of point defect (vacancy/ASD) concentrations for B2 compound alloy. A-rich alloys prefer to generate A antisite defect in B sub-lattice site, and B-rich alloys prefer to generate triple defect, B solute defect and two vacancy defect in A sub-lattice site.

1.3. Application of TiCu-based superelastic alloys

1.3.1. Elastocaloric effect in superelastic alloys

Elastocaloric cooling has been known as the most promising alternative technology to the vapor compression cooling system. It is based on the latent heat related with the MT process, which has been known in SMAs when they are subjected to cyclic loading and unloading procedures. Fig. 1.6 visualizes the elastocaloric cooling system. The SMA is initially fully austenite under the stress-free condition at the room temperature. When the stress on the SMA exceeds the critical stress of characteristic level, the austenite phase starts to transform into the martensite. During the MT, entropy reduces and latent heat is released to the ambient temperature. The reverse MT change from martensite to austenite takes place once the loading pressure decreases below the critical level of MT. The critical stress of unloading may not be identical to that of loading due to friction. The entropy and enthalpy increase and the SMAs absorb heat from the ambient, which could be utilized for the cooling effect. The principle determines the cyclic nature of elastocaloric cooling system, that is the most important difference from vapor compression system. Another difference from the vapor compression is the requirement of a heat transfer fluid (HTF), since solid-state SMAs cannot flow like a liquid or gaseous refrigerant.
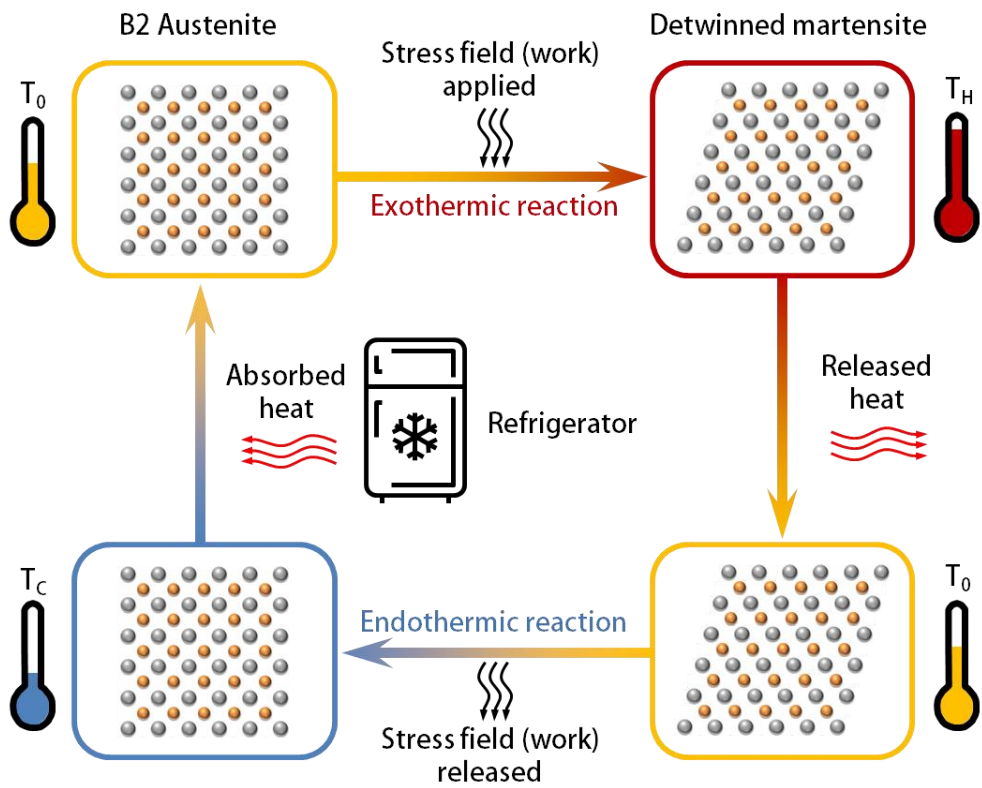
Fig. 1.6. Schematic illustration of the typical features of an elastocaloric cooling by shape memory alloys.

Fig. 1.6. shows the typical illustration of an elastocaloric cooling. The most important part of the system is the elastocaloric materials. Materials with different viable cycles should be considered for efficient heat change material. Another feature is the loading/driving systems that require work input. Unlike compressible gaseous/liquious refrigerants used in vapor compression system, undergoing large specific volume change, the solid-state phase transformation in elastocaloric materials is usually corresponding to very small strain. As a result, the MT of SMAs requires very high pressure. Heat transfer between the elastocaloric material and the heat transfer material is very important as well.

The temperature change in SMAs originate primarily from the difference in chemical entropy of parent and product phase, but elastic energy and irreversible energies like friction or the introduction of dislocation should be considered for the thermodynamics of the MT. It is therefore important to design alloys with large entropy changes. Other important problems that have not yet been solved are the functional and mechanical fatigue. Fatigue in elastocaloric alloys is pivotal for any cooling system as it is directly related to the potential cooling performance of the material. Since the elastocaloric effect in SMAs is caused by the chemical entropy difference that is related to MT, elastocaloric fatigue has a close correlation with the characteristics of MT and their functional and mechanical fatigue properties. An increase in remnant strain during cyclic deformation, due to the introduction and multiplication of many kinds of defects results in an increase of the volume fraction of remained martensite.
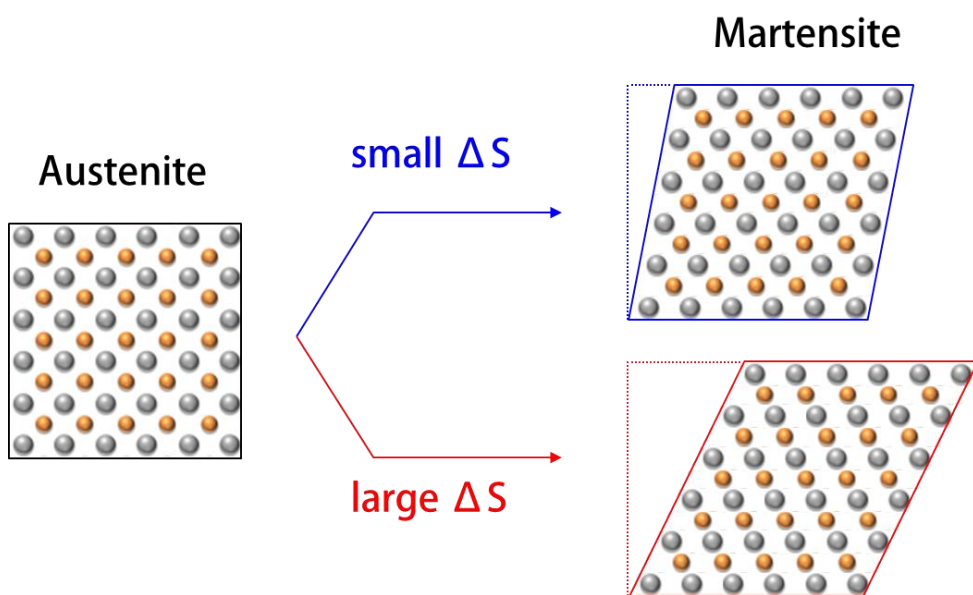
Fig. 1.7. Difference of lattice structure between austenite and martensite phase according to the amount of entropy change during martensitic transformation.

1.3.2. Bulk metallic glass matrix composites

Bulk metallic glasses (BMGs) are characterized by superior properties such as ultra-high strength, low Young's modulus, and large elastic limit. Unfortunately, monolithic BMG undergoes inhomogeneous plastic deformation during loading at room temperature, and shear bands are formed where the stress is confined. This instability severely restricts engineering applications of BMGs. To overcome the limitation concerning catastrophic failure of BMGs, the concept of developing heterogeneous microstructure with in-situ formed secondary phases has been used.

Recently, a design method for composite material capable of realizing work hardening behavior during tensile deformation by precipitating a second phase capable of stress-induced martensite transformation into an amorphous matrix has been proposed and intensively studied. One of the most common manufacturing methods of such bulk metallic glass matrix composites is in situ composite structure formation by casting processes such as drop casting, tilt casting, or suction casting. In this case, there is an advantage that the interface bonding force between the second phase and the base phase is excellent, but there is a limit in that there is no systematic method for controlling the composition and mechanical characteristics of the second phase. In order to solve this problem, the bulk metallic glass matrix composites were deposited in the Ti-based multicomponent alloy system by the polymorphic transformation of the second phase in the amorphous matrix, and composites were prepared by copper mold suction casting in the alloy composition. The composite materials are advantageous in that the precipitation rate of the second phase reinforced in the matrix is very sensitive to the cooling rate, so that the phase fraction can be effectively controlled by adjusting the casting

process conditions. In order to investigate the correlation between the fraction of the secondary phase and the mechanical properties of the amorphous matrix composite, mechanical properties such as strength, plasticity and work hardening behavior of the composite materials should be modulated by the properties of secondary phase.
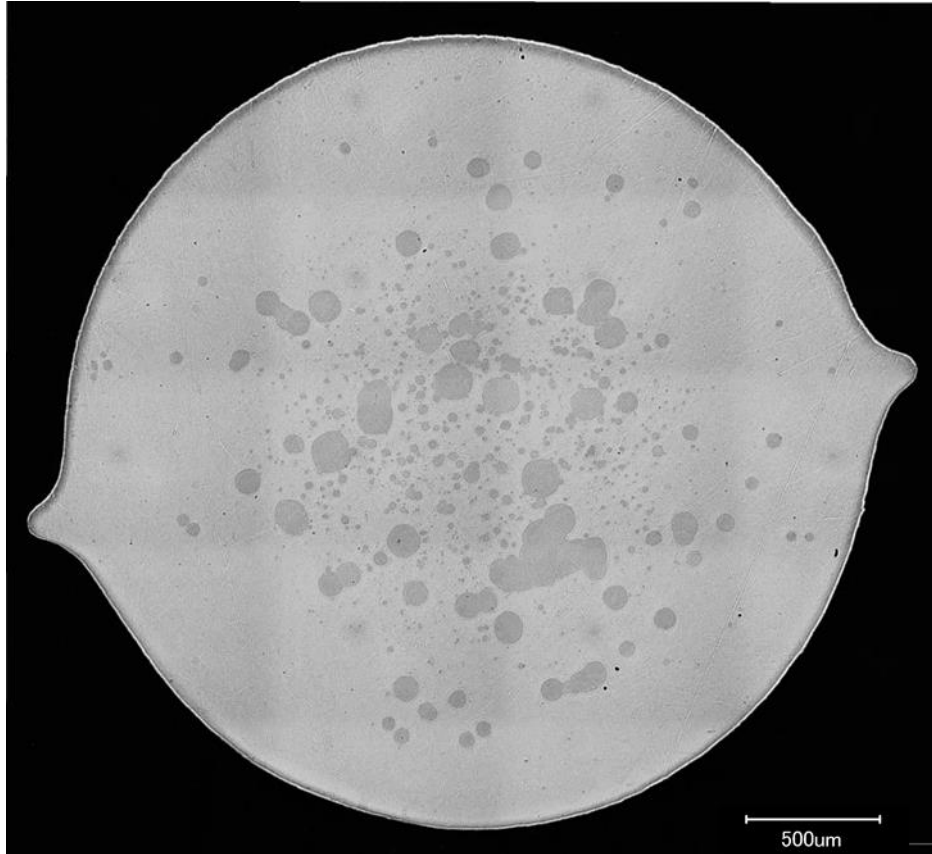
Fig. 1.8. FE-SEM image of cross section of in-situ fabricated bulk metallic glass matrix composite. The gray phase exhibit polymorphically crystallized secondary phase, and the white phase is glassy matrix phase.

Chapter 2.

Experimental and calculation procedures

2.1. Sample preparation

2.1.1. Arc melting and suction casting

The alloy ingots of the desired compositions in Ti-Cu-Ni-Si-Sn system were prepared by arc-plasma re-melting elements with high purity (over 99.99 %). Prior to the melting the mixture of elements, a pure Ti button was melted, which act as a getter for remaining oxygen in high-purity Ar atmosphere. They were re-melted at least seven times in a Ti-gettered Ar atmosphere in order to ensure compositional homogeneity. Cylinders 3 mm in diameter and 50 mm in height for the all of the compositions were prepared by a suction-casting apparatus attached to the arc-melter (Samhan Vacuum Development). The cylinders were mechanically polished to about 200um in thickness from the surface. Weight loss by melting process was controlled to be less than 1% of the initial weight.
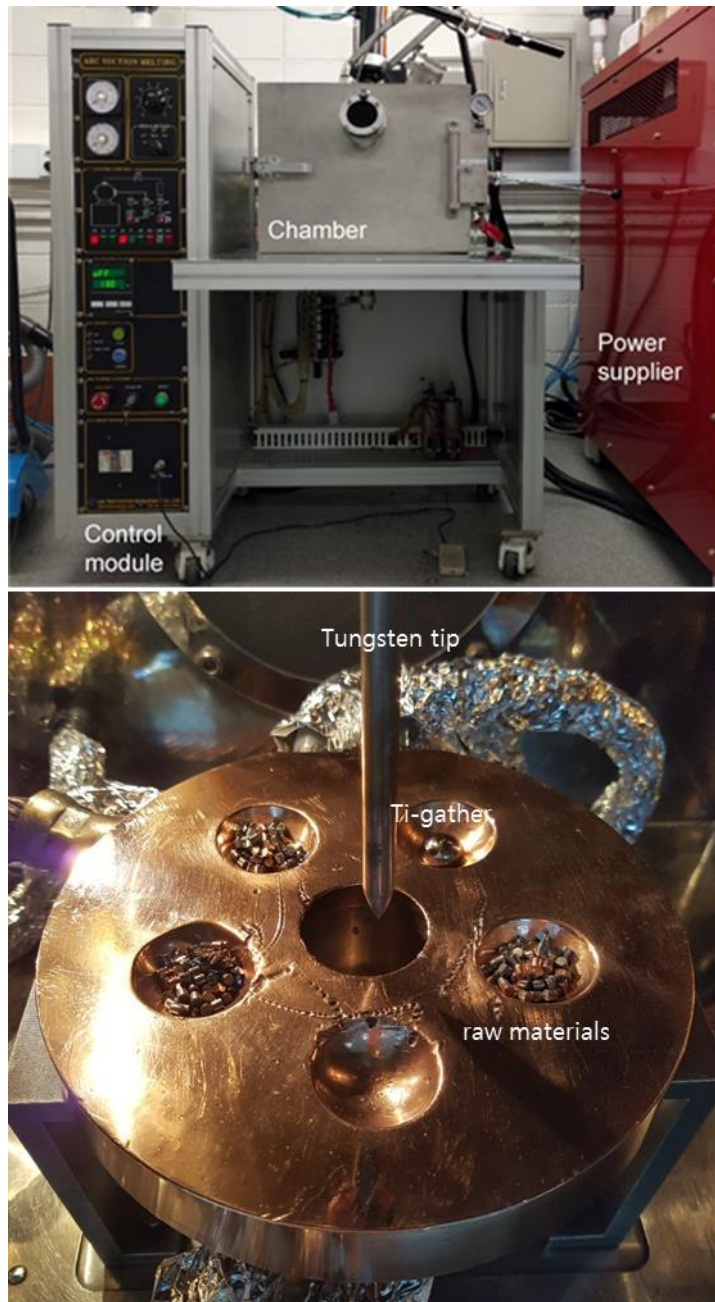
Fig. 2.1. The overview of arc melting machine and the detailed construction inside the arc melting chamber.

2.2. Structural characterization

2.2.1. Scanning electron microscopy (SEM)

Secondary electron micrograph was obtained by field emission scanning electron microscope (FE-SEM, Hitachi, SU70, Japan) equipped with energy dispersive X-ray spectroscopy (EDS). To obtain the microstructures, the samples were fixed on the aluminum holder by using electrically conductive carbon tape. Fine-polished cross sections of as-cast alloy samples were directly observed by secondary electron and EDS detector.

2.2.2. Electron back scattered diffraction (EBSD)

The constituent phases and the average grain size were examined by FE-SEM (Hitachi, SU70) combined with electron backscattered diffraction (EBSD, operated at 20 kV with a step size of 0.5 micrometer). The EBSD samples were polished using a colloidal silica suspension and then ion-milled to remove the damaged layer.

2.2.3. Transmission electron microscopy (TEM)

The structure of as-cast cylinder samples were characterized using high-resolution transmission electron microscopy (HRTEM) and the selected area electron diffraction (SAED) technique. Thin-foil samples of $(Ti_{51}Cu_{41}Ni_7Si_1)Sn_1$ and $(Ti_{51}Cu_{41}Ni_7Si_1)Sn_2$ for TEM observation were prepared by FIB sample preparation using an FEI Nova 600 NanoLab DualBeam SEM/FIB system after mechanical thinning process. A standard ion column was installed, which allowed Ga milling at 5–30 kV. A 200 kV field-emission TEM (Tecnai F20) was used for bright-field imaging and electron diffraction.

2.2.4. X-ray diffraction (XRD)

The cylinder specimens were characterized by X-ray diffraction (XRD, Bruker D2 phaser and New D-8 advance) using monochromatic Cu Kα radiation to identify phases and crystal structures in 2 different temperatures of 293K, 333K, and 363K.

2.2.5. Neutron diffraction

2.2.5.1. Residual strain instrument (RSI)

The stress-induced martensitic phase transformation behavior from austenite to martensite was characterized by in-situ neutron scattering measurement under compressive loading (RSI, Hanaro, KAERI). The incident neutron source has gauge volume of 2mm×2mm×2mm and deep penetration depth (over 1cm), and wavelength of 1.46Å .

2.2.5.2. High resolution powder diffraction (HRPD)

The cylinder specimens were characterized by high resolution powder diffraction(HRPD, Hanaro, KAERI). The HRPD system is equipped with a Ge(331) monochromator and a 32-channel multi-detector system. About 10g of cylinder specimens of each composition were packed in a vanadium can. The data were collected with a wavelength of 1.8367Å over the 2θ range 10-155° at a step size 0.05°.
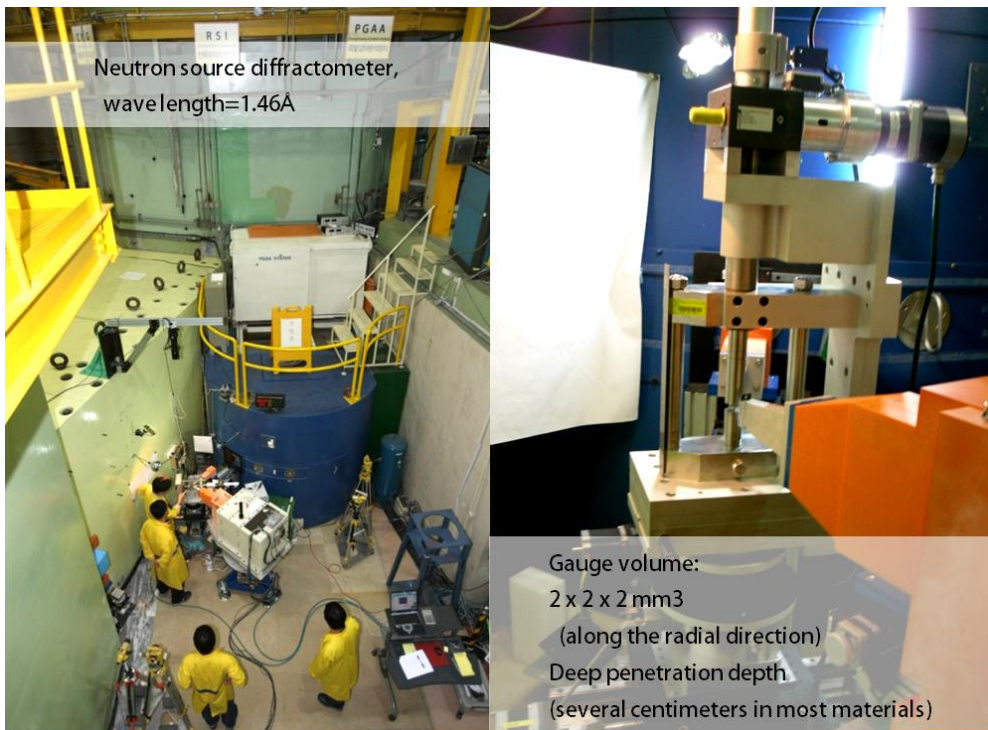
Fig. 2.2. The residual stress instrument in HANARO, KAERI, Korea; In-situ neutron diffraction pattern can be measured by the neutron source with gauge volume of 2x2x2 mm^3, penetration depth of several centimeters.

2.2.6. Synchrotron X-ray diffraction

The in-situ synchrotron-based high-energy X-ray diffraction (HE-XRD) technique was adopted in this study to investigate the microstructure of the as-cast specimens and stress-induced martensitic phase transformation behavior of the specimens. The HE-XRD experiments were performed at 11-ID-C beamline at the Advanced Photon Source (Argonne, IL, USA). The wavelength of the X-ray beam was given as 0.117980 Å corresponding to beam energy of 105.1KeV. Compressive specimens of 3 mm diameter and 6 mm height mounted on loading frame. The CeO_2 powder was employed for calibrating the distance between the specimen and 2-D detector. 2D Circular ring diffraction patterns from the specimens were recorded in 30-second intervals under compressive loading.

2.2.7. Rietveld refinement (MAUD)

X-ray diffraction patterns of TiCuNiSiSn SMAs were analyzed using Materials Analysis Using Diffraction (MAUD) software. Especially, the lattice parameters of the SMAs are measured by fitting calculated diffraction patterns. Rietveld refinement, which is a technique for determining the crystalline materials, was used for the fitting [14]. The Rietveld refinement method uses a least squares approach to fit calculated line profiles until it match the real diffraction patterns as shown in Fig. 2.5. It is possible to estimate maximum transformation strain, thermal hysteresis, and volume change during MT from the measured lattice paremeters of B2 austenite and B19 martensite phase of the samples.
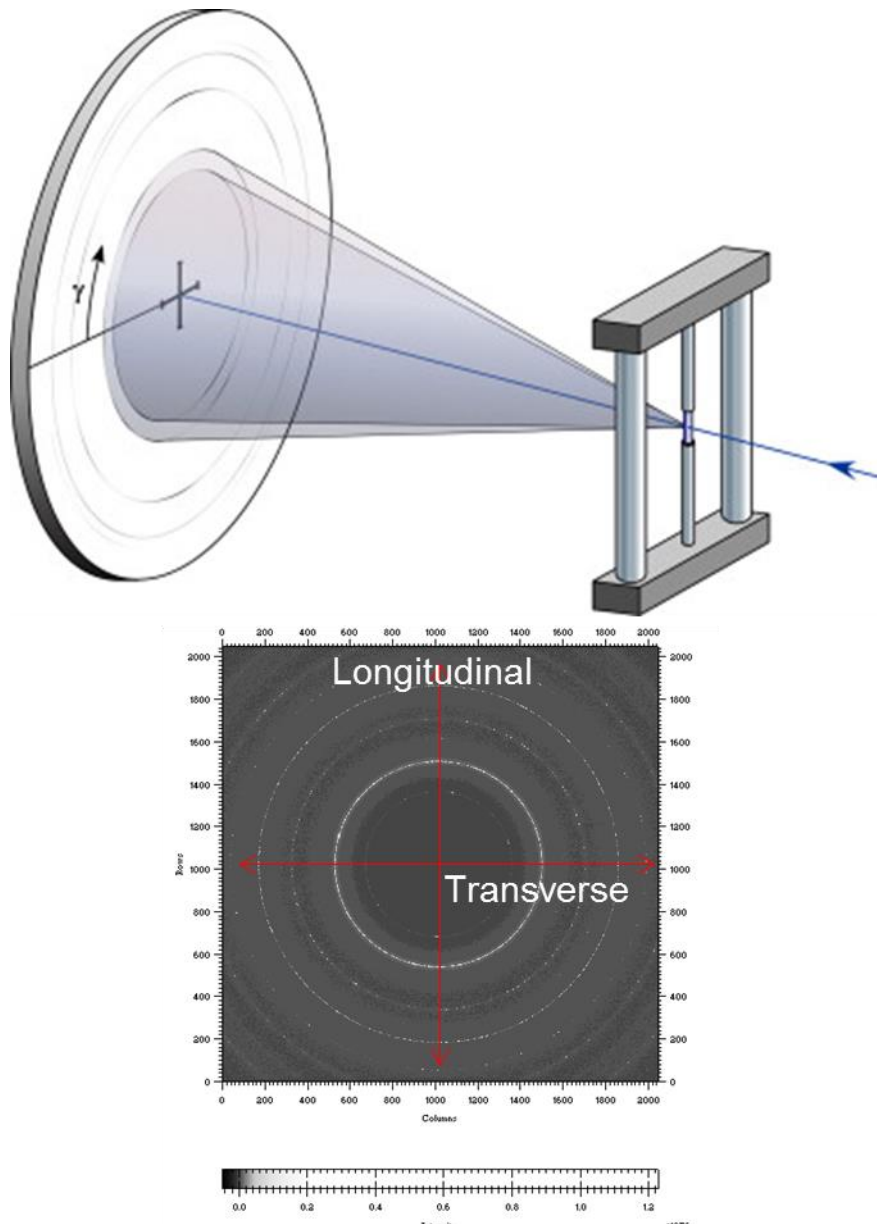
Fig. 2.3. Description of the setup for in-situ synchrotron diffraction pattern measurement under compressive loading. Diffraction patterns were recorded by a two-dimensional (2-D) image plate detector (Mar345).
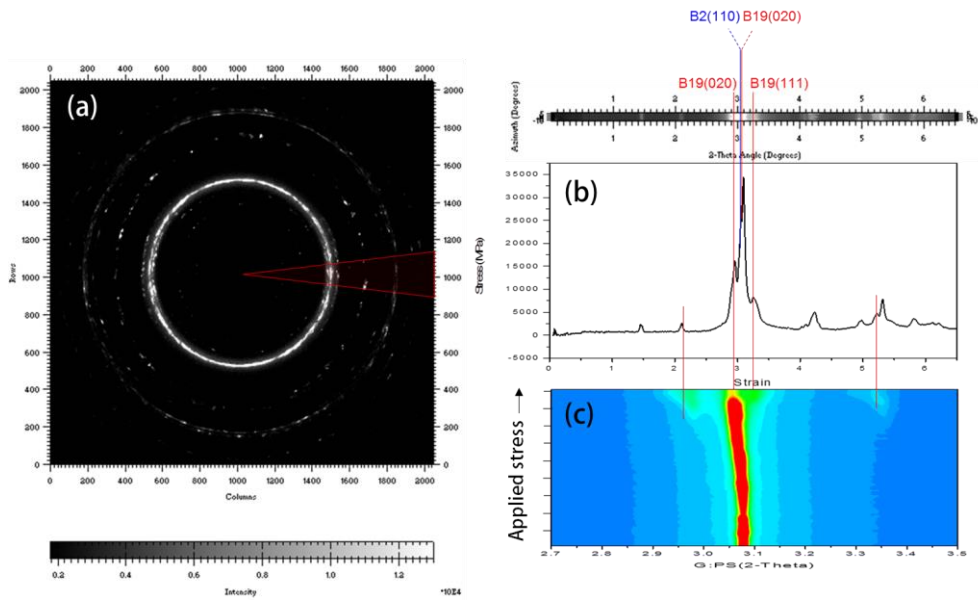
Fig. 2.4. 2-D diffraction pattern of deformed bulk metallic glass matrix composite (a); red triangle represent selected zone along transverse direction of loading axis. The integrated 1-D diffraction pattern of the red triangle in (b); plots of 1-D diffraction patterns along the applied stress (c).
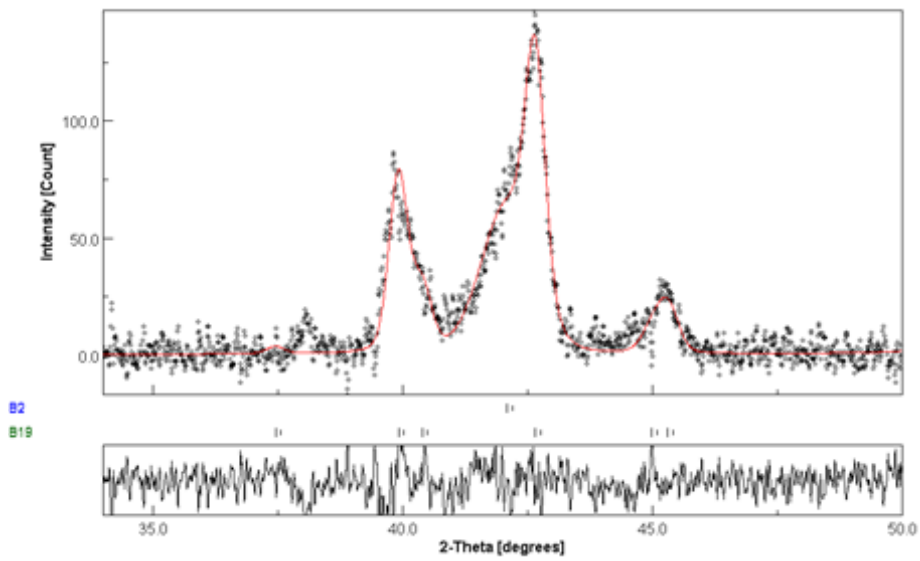
Fig. 2.5. The dotted line shows X-ray diffraction pattern of TiCu-based SMA. The calculated solid line was refined with the experimental pattern.

2.3. Thermal analysis

2.3.1. Differential scanning calorimetry (DSC)

Thermal response of materials with increasing temperature was characterized by differential scanning calorimetry (DSC, Perkin Elmer, DSC 8500 and and TA Instrument DSC Q1000 with liquid nitrogen cooling system, USA). to examine enthalpy of transformation and characteristic transition temperatures (Martensite start temperature (M_s), Martensite finish temperature (M_f), Austenite start temperature (A_s), Austenite finish temperature (A_f)) of reversible martensitic transformation with heating/cooling rates of 10 K min^{-1}. nd specific heat. Specific heat was determined by DSC in the temperature range of 273 K – 600 K under argon atmosphere at a flow rate of 20 mL/min. To obtain accurate results, electric intracooler system was utilized to equilibrate the sample holder below room temperature. Samples were prepared by cutting and grinding alloys with thickness under 1 mm to minimize conduction effect. The weight of samples was precisely measured by using ultra micro electrical balance (Perkinelmer) with a resolution of 10^{-4}g.

2.3.2. Tunnel diode oscillator (TDO)

Tunnel-diode oscillator (TDO) measurement was carried out from near RT down to below 5 K using average heating and cooling rate of 2 K/min. Our TDO setup is based on LC tank circuit where the capacitor couples to the sample, and any change in physical properties of the sample affect the inductance, and thus resonant frequency (ω) of the sample. The resonant method has the advantage of high precision and sensitivity to detect changes in the physical properties of materials as a function of temperature, because ω can be measured with very high degree of accuracy. Cylindrical samples were placed as an inductor in self-resonance coil of LC tank circuit with the distance of $d_0 + d$ where d_0 is the minimal accessible distance for adequate sensitivity. For metallic samples, a radio frequency field can penetrate only by a finite thickness defined by skin depth (δ). The change of ω which depends on δ was measured. In order to obtain high stability in cryogenic temperature, an open-flat coil was adopted with the liquid He-cooled cryogenic free magnet system. By detecting the $\Delta\omega$ caused by the MT, the variation in characteristic temperatures of MT (M_s, M_f, A_s, A_f) was measured down to below 5 K. Fig. 2.6 shows plots of $\Delta\omega/\omega$(baseline subtracted) by MT of Sn2, Sn3, Sn4, Sn4.7 and Sn5 as a dimensionless quantity. Table 1 in the manuscript summarizes the measured M_s, M_f, A_s and A_f by DSC and TDO.
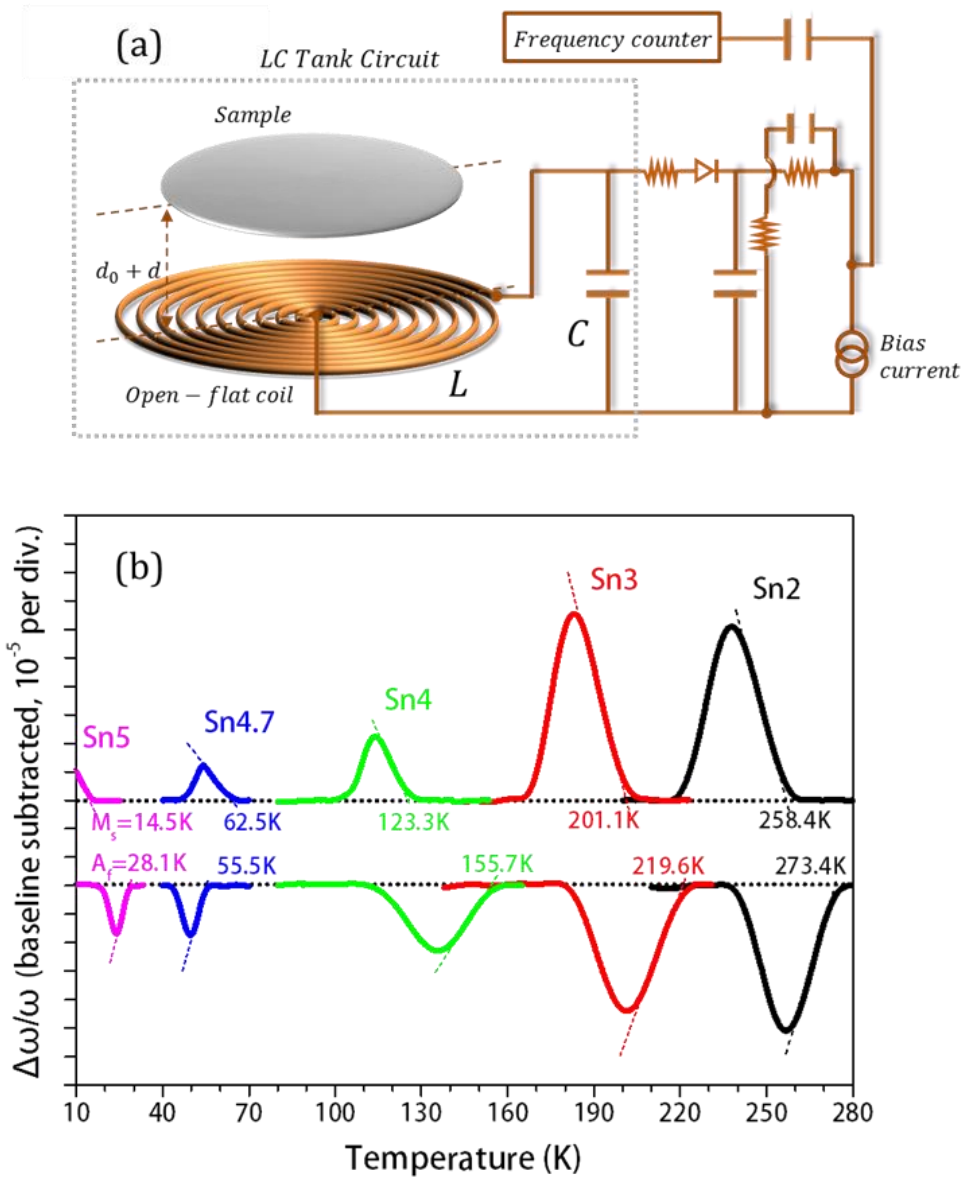
Fig. 2.6. (a) Schematic illustration of the self-manufactured TDO setup; Open-flat type coil was adopted for high resolution of skin depth, especially for measurement in cryogenic temperature. (b) Resonant frequency shift by MT of $(Ti_{51}Cu_{41}Ni_7Si_1)_{100-x}Sn_x$ (x=2, 3, 4, 4.7, 5). The M_s and A_f of each composition are marked.

2.3.3. Dynamic mechanical analyzer (DMA)

Thermomechanical response was examined by dynamic mechanical analysis (DMA). Four DMA experiments were conducted, on plate specimens prepared by suction casting into a 2.5mm×6mm×40mm Cu mold followed by mechanical polishing to the dimensions of 1.5mm×4mm×25mm, on a PerkinElmer DMA 8000 device with liquid nitrogen dewar kit, functioning in three point bending mode, at a frequency of 1 Hz and an amplitude of 50μm. Heating was performed at a rate of 40 K min^{-1} from 150 to 400 K.

2.3.4. Dilatometry

The thermomechanical property of as-quenched specimens was studied with a Netzsch DIL204c dilatometer (heating rate of 5 K per min). The dilatometery performed from room temperature to -150 ℃ paying caution for the MT region of the SMA specimens. The cooling were carried out on a liquid nitrogen cooling system to control the furnace temperature. The measured dilatometry curves were compared to DSC measurement result for determining the characteristic temperature of MT.
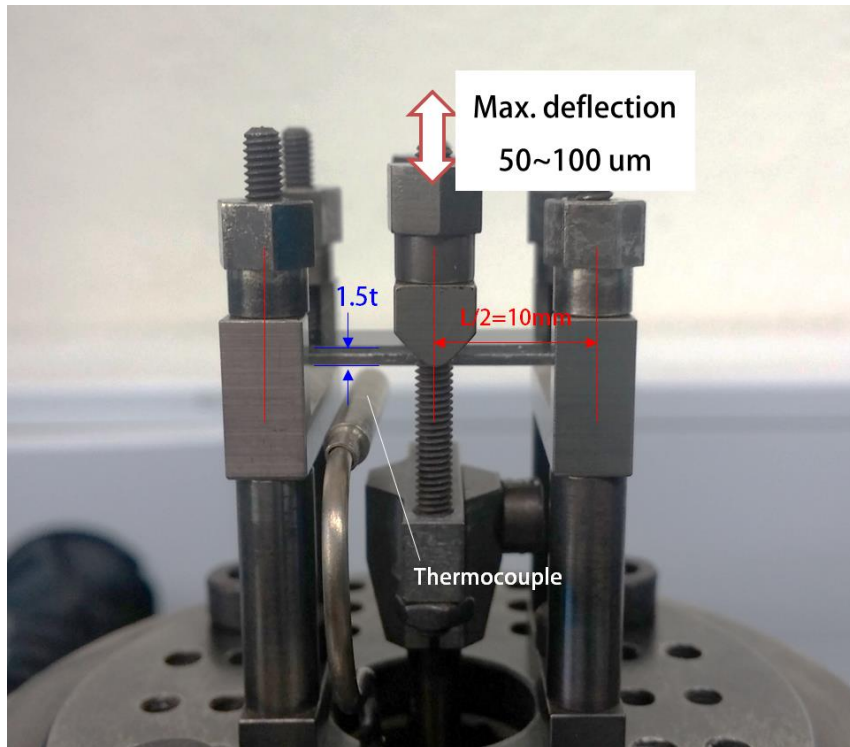
Fig. 2.7. Dynamic mechanical analyzer setup for 3-point bending mode; Sample dimension is (1 ± 0.5)mm*$(25\pm5$mm). The maximum deflection of the bending test is 50-100μm.

Fig. 2.8. Overview and loading stage of dilatometer for measuring volume change during martensitic transformation

2.4. Mechanical analysis

2.4.1. Uniaxial compression test

The mechanical behavior during compression was investigated using an Instron 5967 testing machine at a constant strain rate of $1 \times 10^{-4}\,s^{-1}$ for cylinder specimens. At least five specimens of each composition with 1:2 aspect ratio were tested to ensure reproducibility. The sample was fixed between the anvils with two tungsten carbide plates to prevent permanent deformation of the anvils

2.4.2. In-situ high temperature compression test

Compressive testing at elevated temperature was performed at constant strain rates of $1 \times 10^{-4}\,s^{-1}$ for cylinder specimens. A uniquely self-manufactured high temperature compressive stage including a laser extensometer was used. At least two specimens for each temperature were tested to ensure reproducibility. The samples were fixed between the anvils with thermocouples to insure the testing temperature.

2.4.3. Vickers hardness test

Vickers hardness measurements were conducted using an EMCO-TEST DuraScan 70 under a loading of 0.1 kgf. The hardness tests were repeated 10 times to obtain an average values, and standard deviations were used as the error ranges.

2.4.4. 3-point bending and fracture toughness test

The mechanical testing of 3-point bending and fracture toughness test were performed on as-cast rods of TiCuNiSi and TiCuNiSiSn SMAs. The rods machined into square poles (2.5mm × 50mm). The samples have fully B2 of 19 crystalline phase as indicated by X-ray diffraction, transmission electron microscopy, and high resolution powder diffraction. The critical deflection stress was determined by composition and M_s of the sample through bending test, and the difference between B2 phase and B19 phase was analyzed. Fracture toughness was determined by monotonically deforming the fatigue pre-cracked specimens to failure at specific strain rates (ASTM E399). K_{IC} values were compared according to the alloy composition, since depending on the ductility of the sample, brittle fracture occurs without crack propagation.

2.4.5. Ultrasonicwave measurement

Ultrasonic wave propagating measurement was conducted by ultrasonic pulse-receiver, ultrasonic wave transducer (computer controlled pulse/receiver 5800), and a digital oscilloscope (TDS220). The shear modulus was calculated after getting the elastic wave propagating velocities and the material density. The density of the alloys was measured by Archimedes' principle with an electrical balance (XS204, Mettler Toledo, Switzerland).

2.5. Ab-initio calculation

2.5.1. Special quasi-random structure (SQS)

Four special quasi-random structures (SQS) [15] have been considered in the Ti-rich or Cu-rich compositions in which Sn is preferred to Ti-site or Cu-site. The descriptions of the SQS structures are shown in Fig. 2.9. The four initial SQSs have been constructed by adjusting the lattice constant and replacing Ni with Cu in the structures of TiNi-X SQS modeled by N. Singh et al [30]. Each SQS consists of a total of 32 atoms, Ti-rich structures are composed of 16 Ti, 15 Cu and 1 Sn, and Cu-rich structures are composed of 15 Ti, 16 Cu and 1 Sn.

2.5.2. VASP code

The calculations were performed to analyze the site preference of Sn element added on TiCu B2 phase with the Vienna Ab Initio Simulation Package (VASP) [31], using the frozen core all-electron projector augmented wave method (PAW) [32, 33] and the generalized gradient approximation of Perdew, Burke, and Ernzerhof [34]. The Brillouin zone integrations were performed using Monkhorst-Pack k-point meshes. Optimal atomic configurations were obtained by relaxations in which volume, shape and ionic positions were allowed to vary. A total energy convergence of 1 meV per atom was obtained. A kinetic cutoff energy of 400 eV was used. The k-point mesh was selected based on what converged the total energy to under 1 meV/atom.
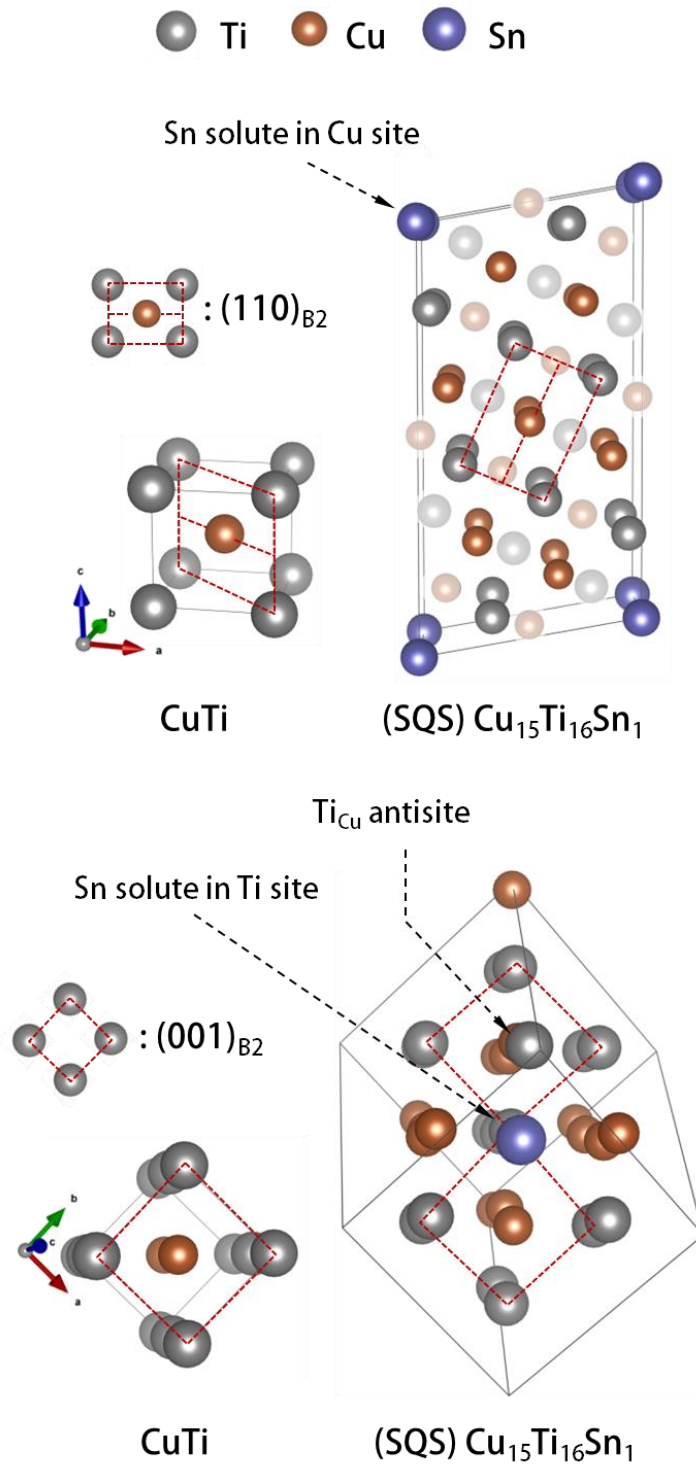
Fig. 2.9. Schematic illustrations of the two different special quasi-random structures (SQS) of Ti-rich B2 phase in this study.

2.6. Calculation of Phase Diagrams (CALPHAD)

2.6.1. CuTi-NiTi pseudo-binary phase diagram

The pseudo-binary equilibrium phase diagram of $Cu_{50}Ti_{50}$-$Ni_{50}Ti_{50}$ in Cu-Ti-Ni ternary alloy system was calculated with the help of thermodynamic software Thermo-calc™. The calculated phase diagram was compared to the reported pseudo-binary phase diagram of CuTi-NiTi, and the experimental data of X-ray diffraction pattern of TiCuNSi alloy system, especially for the composition range of two-phase, primary B2 and liquid, stable region.

2.7. Measurement of caloric effect

2.7.1. Infra-red imaging

In order to evaluate the elastocaloric effect in as-cast rod specimens and its fatigue property, the temperature changes in the rods during uniaxial cyclic loading were monitored by means of thermography with infrared (IR) camera. The temperature changes were measured during a large number of superelastic cycles, and have a correlation to their corresponding stress-strain curves.

2.7.2. Brayton cycle

The cycles plotted in Fig. 2.10 are a Brayton cycle(consists of two isentropic processes and two iso-stress processes, adiabatic or quasi-adiabatic, blue line) and isothermal cycle(red line). The isothermal cycle is deformed and recovered continuously at a very slow and constant strain rate. However, in the case of the Brayton cycle, strain and recovery progress at a very high strain rate to minimize heat loss due to thermal conduction during loading and unloading. In the case of the Brayton cycle, since the temperature of the sample changes due to heat absorption and release occurring at the time of MT, it has a larger critical stress for MT than in the isothermal cycle. Therefore, the mechanical hysteresis in the cyclic deformation is larger than the isothermal cycle in the Brayton cycle, as shown in Fig. 2.10.
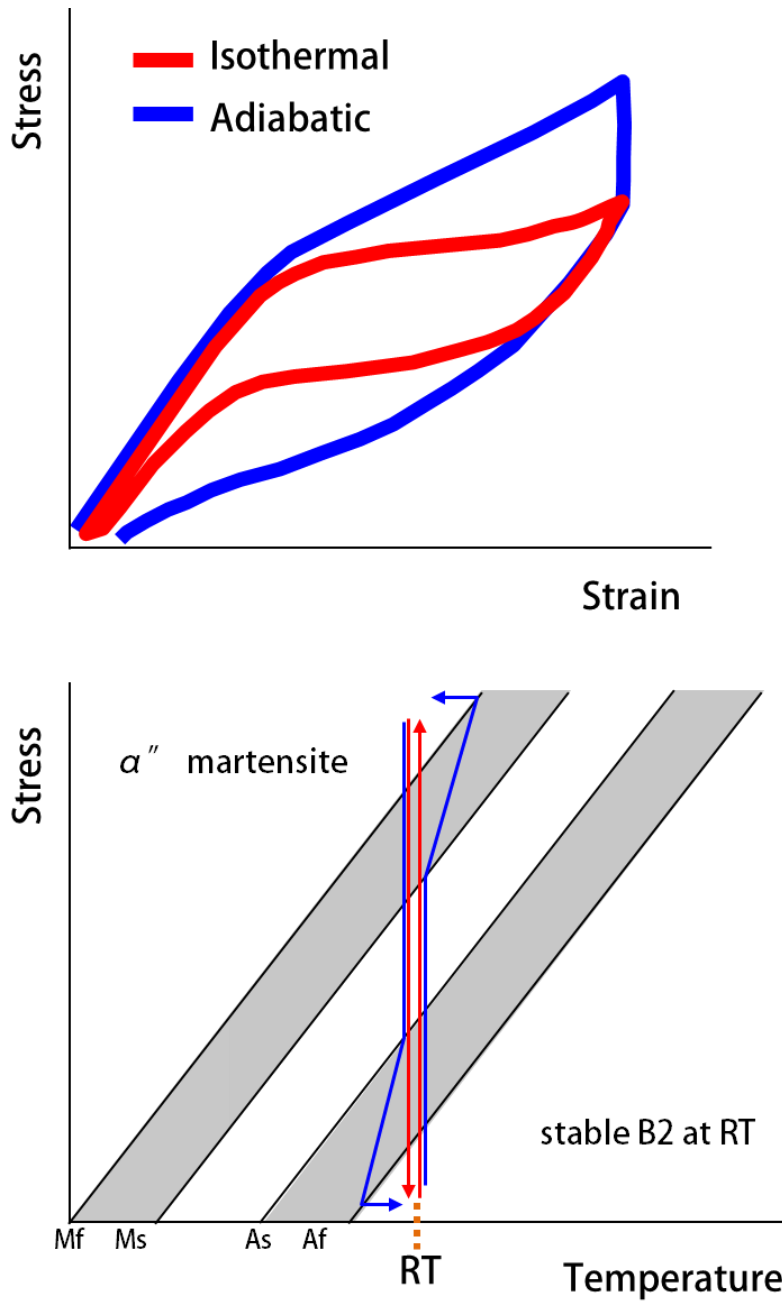
Fig. 2.10. Schematic illustration of stress-strain curves and stress-temperature trajectories on phase diagram for isothermal cyclic deformation and adiabatic(Brayton cycle) cyclic deformation.

Chapter 3.

Development of TiCu-based shape memory alloys

3.1. Si solubility in TiCuNi B2 phase

In the conventional NiTiCu ternary SMA system, it has been reported that the precipitation of intermetallic compounds easily take place because the phase stability of B2 (B19) is not sufficient in the Cu-rich composition. In order to increase the Cu content, a small amount of Si was added as to suppress other precipitates except the B2 (B19) phase. According to reports [16], the addition of Si stabilizes the high temperature stable BCC phase, and inhibits other precipitates that affect mechanical properties[17]. However, when excess amount is added, the silicide phase, Ti_5Si_3 precipitates, so it should be added within the solubility limit of the Si element. In general, Ti-based alloys are known to form a silicide phase very easily in a very large negative mixed-thermal relationship with Si elements, but the Si solubility is reported to be about 4 at.% In the NiTi B2 phase. Fig. 3.1. shows that The most stable TiCuNi B2 phase precipitates in the Cu-rich composition as Si is added at a level of about 1 ~ 2 at. %.
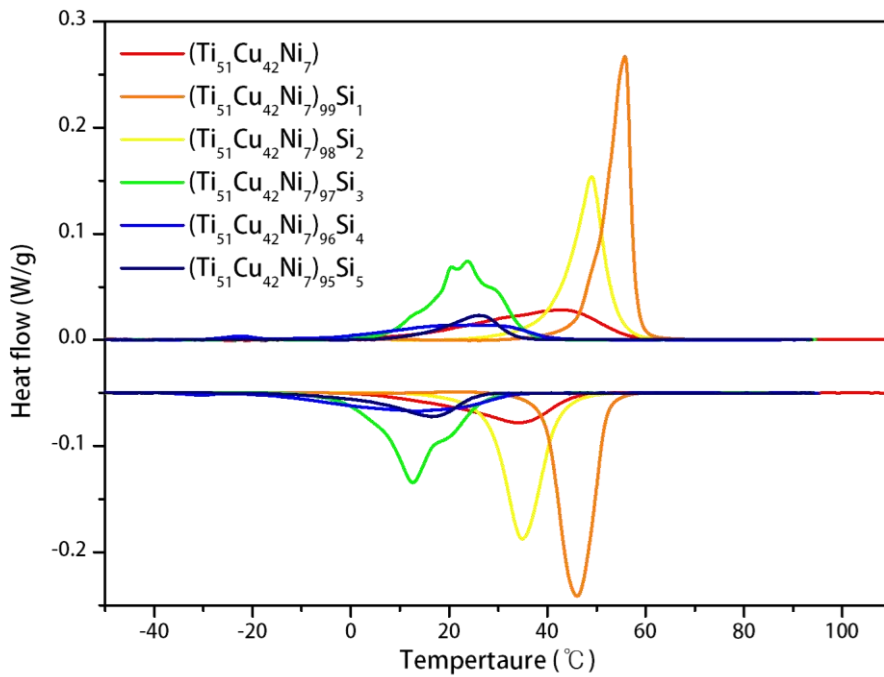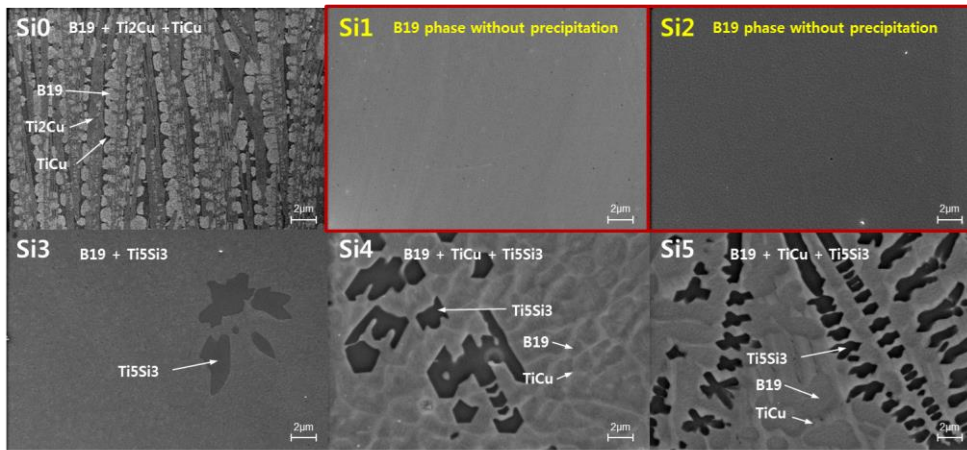
Fig. 3.1. (a) FE-SEM images and (b) plots of DSC traces of $(Ti_{51}Cu_{42}Ni_7)Si_X$ (x =0, 1, 2, 3, 4, and 5 at. %) cylindrical specimen having a diameter of 3 mm.

3.2. Development of TiCu-based shape memory alloys

The martensitic phase transformation behavior and crystal structure of the TiCuNiSi alloy system were investigated by XRD and DSC analysis. Fig. 3.2 (a) shows XRD patterns of cylinder specimens of $(Ti_{50}Cu_xNi_{50-x})_{99}Si_1$ (x = 15, 20, 25, 30, 35, 40, 43, 45 at. %) prepared by suction casting and mechanical polishing. The patterns revealed that B19 martensite phase precipitates when the Cu content is 43 at. % or less, and if the Cu content is over 45 at. %, the B11 phase precipitates.

In this alloy system, the B11-B2(B19) eutectic composition is believed to exist between the Cu43 and 45 compositions, and the primarily precipitated phase in each alloy composition is considered to be reflected in the XRD patterns. Fig. 3.2 (b) represents the DSC measurement results of the cylinder specimens. The specimens of the composition of Cu43 of less with the precipitation of B19 martensite phase exhibited a distinct reversible martensitic transformation behavior, and the transformation temperature tended to increase slightly as the Cu content increased. The specimen of Cu45 composition with the precipitation of B11 phase did not show any heat flow by martensitic transformation. The characteristic temperature and enthalpy changes of each alloy compositions were shown in Table 3.1. As a result, it was confirmed that SMAs with Cu contents of up to 43% can be produced in TiCuNiSi alloy system by adding 1at. % Si. Calculated pseudo-binary CuTi-NiTi phase diagram Fig. 3.3. The phase diagram shows that precipitation of the B2 phase is possible even in the Cu-rich composition.
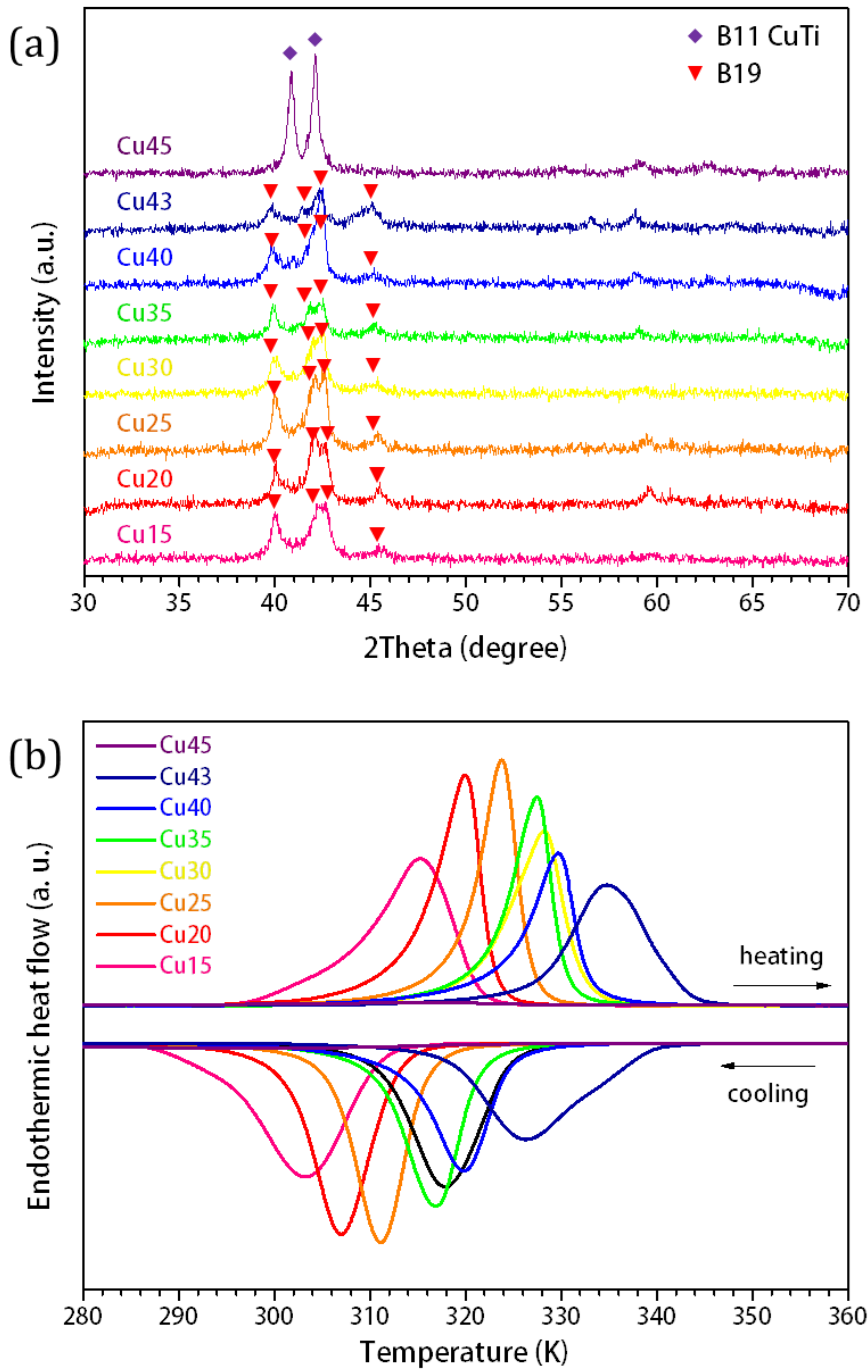
Fig. 3.2. (a) X-ray diffraction patterns and (b) plots of DSC traces of $(Ti_{50}Cu_xNi_{50-x})_{99}Si_1$ (x = 15, 20, 25, 30, 35, 40, 43, 45 at. %) cylindrical specimen having a diameter of 3 mm.

Table 3.1. Characteristic temperatures (M_s, M_f, A_s, A_f, M_p, and A_p) and enthalpy change of MT (ΔH)

Alloy composition (at.%)	M_s (K)	M_f	A_s	A_f	M_p	A_p	$\Delta H_{A \to M}$	$\Delta H_{M \to A}$
$(Ti_{50}Cu_{15}Ni_{35})Si_1$	311.5	293.1	305.2	321.6	303.1	315.3	-14.507	12.567
$(Ti_{50}Cu_{20}Ni_{30})Si_1$	313.3	300.4	312.8	323.0	307.0	319.9	-13.062	12.215
$(Ti_{50}Cu_{25}Ni_{25})Si_1$	316.3	305.1	318.7	326.9	311.0	323.8	-12.589	11.471
$(Ti_{50}Cu_{30}Ni_{20})Si_1$	321.9	309.8	321.6	330.7	316.7	327.4	-12.232	11.125
$(Ti_{50}Cu_{35}Ni_{15})Si_1$	324.8	310.5	320.6	332.2	318.0	328.2	-11.83	10.999
$(Ti_{50}Cu_{40}Ni_{10})Si_1$	325.2	312.9	323.4	332.9	319.7	329.6	-10.3351	9.239
$(Ti_{50}Cu_{43}Ni_7)Si_1$	339.7	317.5	327.1	344.1	326.3	334.8	-10.421	10.561
$(Ti_{50}Cu_{45}Ni_5)Si_1$	-	-	-	-	-	-	-	-
$(Ti_{56}Cu_{37}Ni_7)Si_1$	317.3	255.4	259.7	329.0	299.5	305.3	-2.448	2.040
$(Ti_{55}Cu_{38}Ni_7)Si_1$	349.3	251.3	245.7	359.5	305.4	309.9	-0.468	2.120
$(Ti_{54}Cu_{39}Ni_7)Si_1$	349.7	243.1	246.1	357.5	312.7	317.9	-1.274	6.291
$(Ti_{53}Cu_{40}Ni_7)Si_1$	347.5	260.3	250.4	355.4	310.9	317.9	-3.065	7.906
$(Ti_{52}Cu_{41}Ni_7)Si_1$	345.6	249.5	261.7	357.5	305.7	307.6	-4.087	8.820
$(Ti_{51}Cu_{42}Ni_7)Si_1$	329.0	312.4	323.5	335.8	319.4	331.5	-8.664	8.622
$(Ti_{50}Cu_{43}Ni_7)Si_1$	332.8	310.7	327.7	341.9	323.1	336.5	-8.580	9.860
$(Ti_{49}Cu_{44}Ni_7)Si_1$	330.8	261.5	253.2	339.3	315.7	324.5	-4.144	4.181
$(Ti_{48}Cu_{45}Ni_7)Si_1$	326.7	-	253.5	342.0	303.1	312.4	-2.259	2.125
$(Ti_{47}Cu_{46}Ni_7)Si_1$	316.2	-	253.3	342.2	277.2	286.7	-2.983	2.319
$(Ti_{46}Cu_{47}Ni_7)Si_1$	315.7	-	251.0	355.2	278.2	289.5	-2.142	3.035

Fig. 3.3. Calculated TiNi - TiCu Pseudo-binary phase diagram using Thermocalc software for estimating the composition range of TiCuNi B2 phase.

3.3. Analysis of lattice structure

The conventional NiTiCu SMA system is known to have the feature of narrow hysteresis and excellent functional stability. The high Cu containing TiCuNiSi alloy system also exhibited very low hysteresis. Figure 3.4 (a) shows the hysteresis (M_p-A_p) of TiCuNiSi alloys, and it can be seen that the hysteresis is lower than 10K especially in the composition of Cu over 30%. . When phase transformation from B2 to B19 proceeds, lattice strain occurs through (110)[1-10] – (110)[-110] shuffling. A tensile strain increases along the $[001]_{B19}$ direction, and compressive strain increases along the $[010]_{B19}$ and $[100]_{B19}$ directions. B2 and B19 have a crystallographic correlation as shown in Fig. 3.4 (b). The $[001]_{B19}$, $[010]_{B19}$, and $[100]_{B19}$ axes correspond to the $[-110]_{B2}$, $[110]_{B2}$, and $[001]_{B2}$ axes, respectively.

Table 3 shows the values of lattice parameters and transformation stretches of B19 and B2 obtained by Rietvelt refinement of the XRD patterns measured at a temperature of 293K(B19) and 363K(B2) respectively. The λ_2, XI and XII of AuCuZn, TiNi, TiNiCu, TiNiPd, TiNiHf, TiNiZr and TiCuNiSi alloy systems are listed in Table 3.2. In particular, AuCuZn, TiNiCu, TiNiPd and TiCuNiSi alloys were considered to satisfy the cofactor conditions, as shown in Fig.3.5. In the TiCuNiSi system, there is no significant difference in the values of λ_2, XI and XII depending on the composition, which is considered to support the thermal analysis result that low hysteresis is maintained even when the Cu content changes greatly.
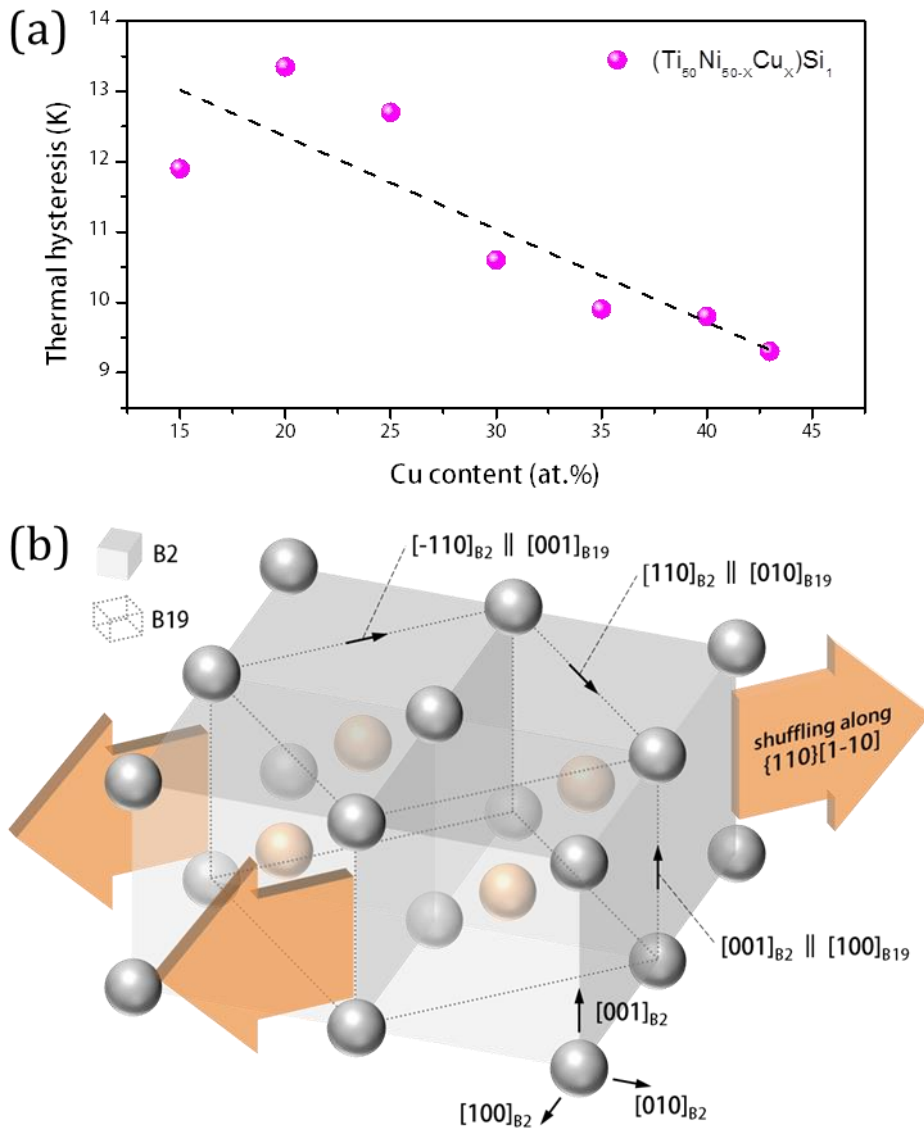
Fig. 3.4. (a) Thermal hysteresis of reverse MT (B19-B2) of TiCuNiSi SMAs, as a function of Cu content. (b) Schematic illustration of crystallographic correlation of B2 austenite and B19 martensite phase.
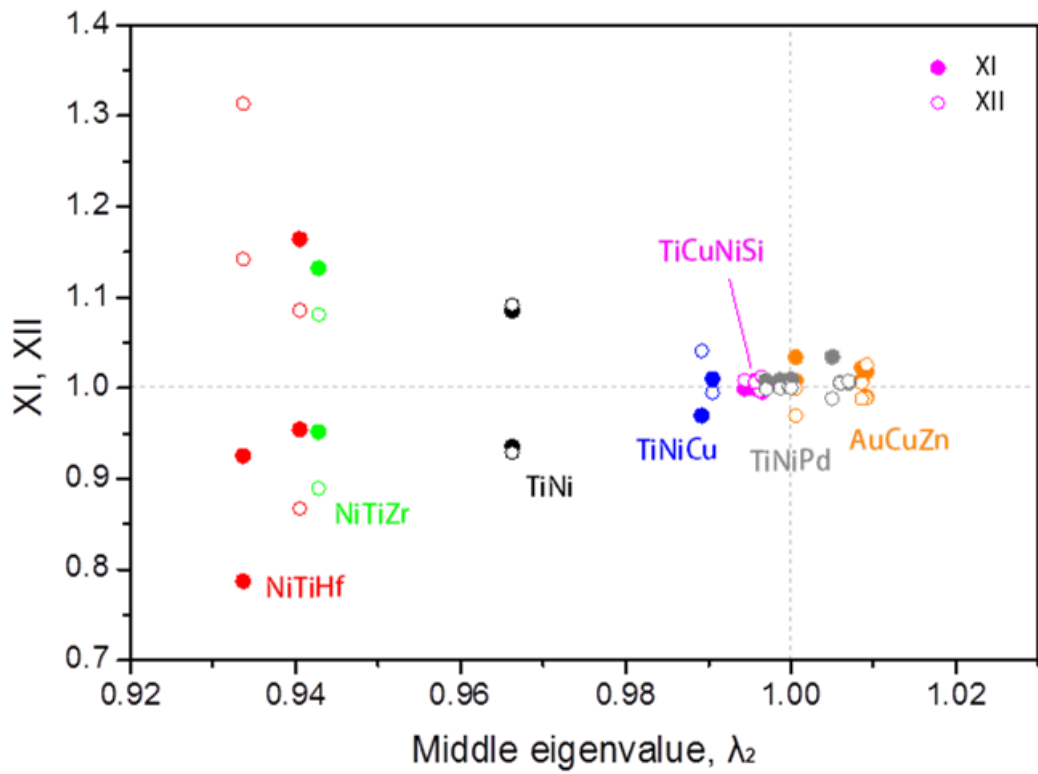
Fig. 3.5. Middle eigenvalue and cofactor conditions XI, XII of NiTi-based and AuCuZn alloy system.

Table 3.2. Middle eigenvalue and cofactor conditions XI, XII of NiTi-based and AuCuZn alloy system.

Composition	λ_2	XI		XII	
$(Ti_{50}Cu_{40}Ni_{10})Si_1$	0.9957	1.0019	-	1.0062	-
$(Ti_{50}Cu_{43}Ni_7)Si_1$	0.9965	0.9957	-	1.0124	-
$Au_{25}Cu_{30}Zn_{45}$	1.0092	0.9899	1.0179	1.0256	0.9893
$Au_{27}Cu_{28}Zn_{45}$	1.0086	1.0090	1.0222	1.0056	0.9884
$Au_{30}Cu_{25}Zn_{45}$	1.0006	1.0081	1.0339	0.9996	0.9695
$Ti_{51}Ni_{36}Cu_{13}$	0.9892	0.9695	-	1.0407	-
$Ti_{54}Ni_{34}Cu_{12}$	0.9905	1.0098	-	0.9951	-
$Ti_{50}Ni_{43}Pd_7$	0.9970	1.0084	-	0.9989	-
$Ti_{50}Ni_{41}Pd_9$	0.9988	1.0088	-	0.9997	-
$Ti_{50}Ni_{40}Pd_{10}$	0.9998	1.0073	-	1.0016	-
$Ti_{50}Ni_{39}Pd_{11}$	1.0001	1.0096	-	1.0002	-
$Ti_{50}Ni_{32}Pd_{18}$	1.0050	1.0342	-	0.9884	-
$Ti_{50}Ni_{30}Pd_{20}$	1.0060	1.0053	-	1.0054	-
$Ti_{50}Ni_{25}Pd_{25}$	1.0070	1.0059	-	1.0074	-
$Ni_{50.3}Ti_{29.7}Zr_{20}$	0.9428	1.1322	0.9519	0.8894	1.0812
$Ni_{48.5}Ti_{36.5}Hf_{15}$	0.9405	1.1641	0.9540	0.8673	1.0856
$Ni_{50.3}Ti_{29.7}Hf_{20}$	0.9337	0.7869	0.9254	1.3135	1.1421
$Ti_{50.25}Ni_{49.75}$	0.9663	1.0853	0.9354	0.9286	1.0918

3.4. Investigation of transformation interval

In the case of the NiTi B2 phase, the transformation temperature of the Ni-rich composition decreases sharply as compared with the stoichiometric composition, while the transformation temperature of the Ti-rich composition does not change much. In comparison, we analyzed the changes in microstructure and transformation temperature in the Ti-rich and Cu-rich compositions of the $(Ti_{50+x}Cu_{43-x}Ni_7)Si_1$ (x = -4, -3, -2, -1, 0, 1, 2, 3, 4, 5, and 6 at. %) alloy system. Fig 3.6 shows a FESEM image of the six selected alloy compositions (x = -4, -1, 0, 1, 2, and 5 at.%). Fig. 3.6. (a, b) show the microstructure of the alloy of Cu (Ni)-rich composition. It was found that nano-precipitates are homogeneously dispersed and, considering the contrast and alloy composition, the precipitates are expected to be Cu-rich compound of Cu_3Ti_2. Fig. 3.6. (c, d) shows that a single phase was formed in the composition of $(Ti_{50}Cu_{43}Ni_7)Si_1$ and $(Ti_{51}Cu_{42}Ni_7)Si_1$ without any precipitate identifiable by FESEM. Fig. 3.6. (e) was an image of the $(Ti_{52}Cu_{41}Ni_7)Si_1$ specimen, and it can be confirmed that the nano-precipitate judged as Ti_2Cu is finely dispersed. Fig. 3.6. (f) shows that three different phases of B19, TiCu and Ti_2Cu were precipitated in the specimen of Ti $(Ti_{52}Cu_{41}Ni_7)Si_1$ composition, and the composition of each phase was confirmed by EDS analysis. It is interesting to note that a specimen composed of a single B19 martensite phase was prepared with a composition with an extremely high Cu content of 43 at.%. It can be seen that the minor addition of Si to the TiCuNi alloy system effectively suppressed precipitation of TiCu B11, Ti_2Cu, and other compounds.

The DSC measurement results of each alloy composition are shown in fig. 3.7. (a) and considered to be compatible with the microstructure analysis results. The

transformation intervals $(\Delta \mathrm{T} = A_f - A_s)$ of the $(\mathrm{Ti}_{50}\mathrm{Cu}_{43}\mathrm{Ni}_7)\mathrm{Si}_1$ and $(\mathrm{Ti}_{51}\mathrm{Cu}_{42}\mathrm{Ni}_7)\mathrm{Si}_1$ compositions are considered to be very narrow, which are 14.2 and 12.3K, respectively. However, the other compositions showed a wide $\Delta \mathrm{T}$ value in the range of 69-114K, and the transformation enthalpy $(\Delta \mathrm{H})$ corresponding to the area of the heat flow curve showed a large difference by composition. Fig 3.7. (b) shows the tendency of $\Delta \mathrm{T}$ and $\Delta \mathrm{H}$ values according to Ti content. It is noteworthy that the $\Delta \mathrm{H}$ values were relatively higher for specimens with Ti-rich composition than those with Ti-lean composition. The characteristic temperature and enthalpy changes of each alloy compositions were shown in Table 3.1.
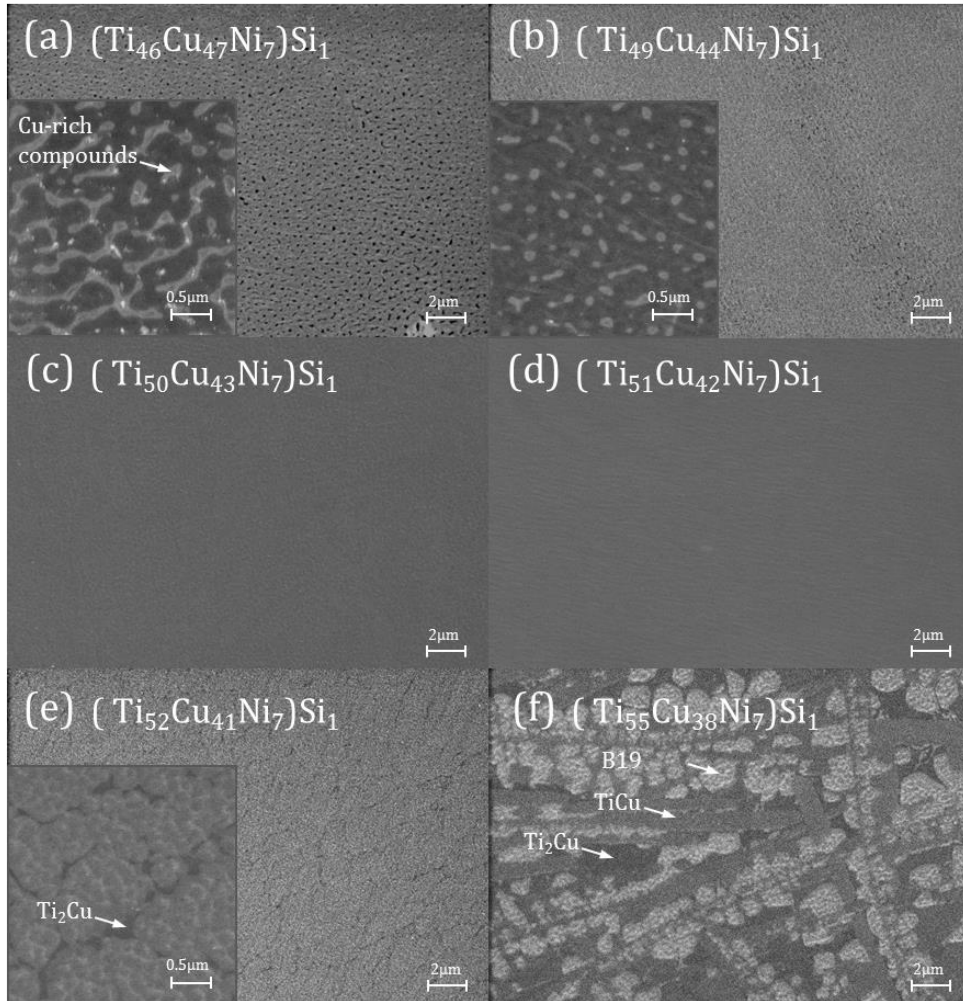
Fig. 3.6. FE-SEM images of $(Ti_{50+X}Cu_{43-X}Ni_7)Si_1$ (X=-4, -1, -, 1, 2, and 5 at. %) alloys. The insets are more magnified images for nano-precipitated specimens.
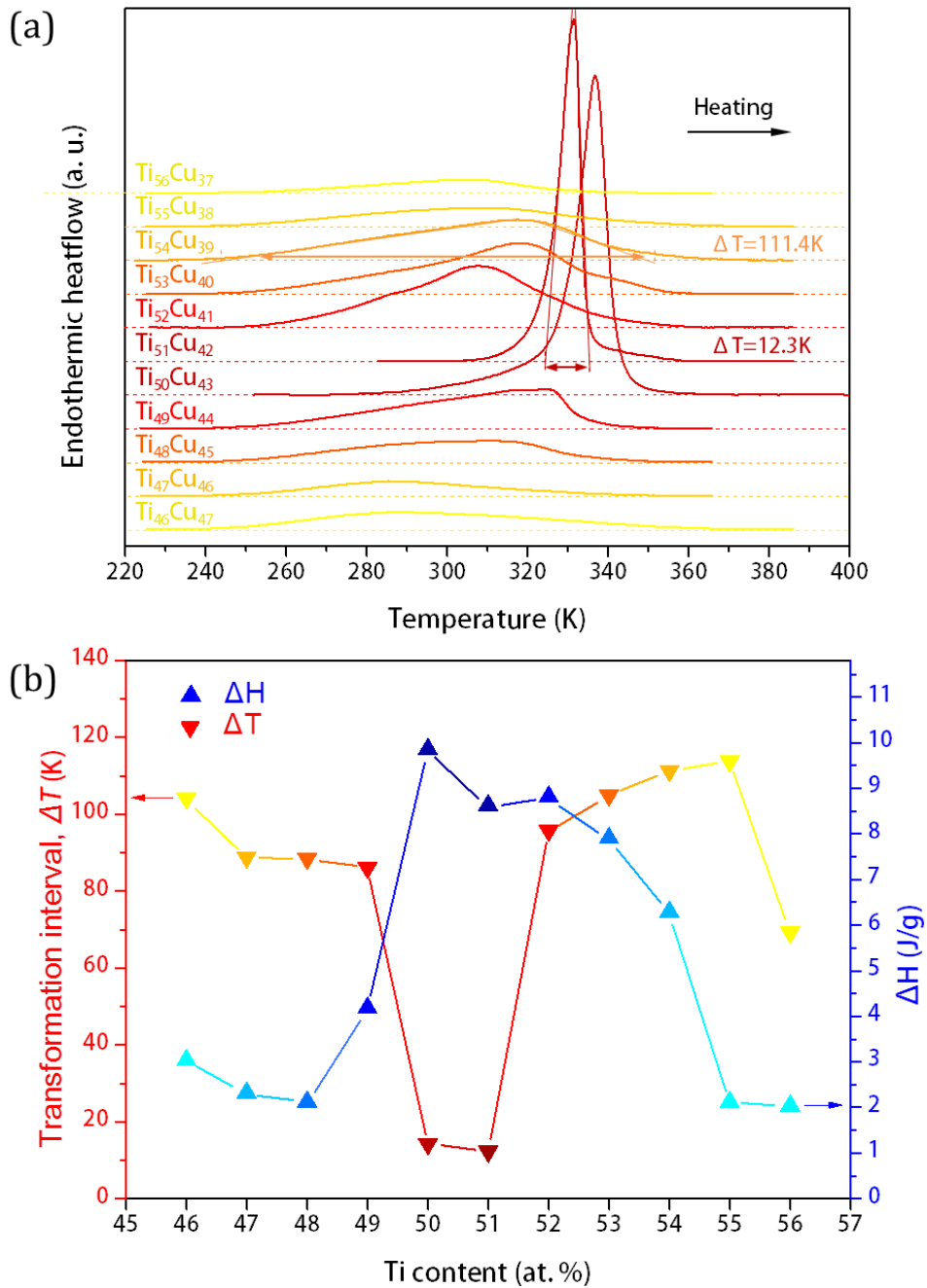
Fig. 3.7. (a) Plots of DSC traces of $(Ti_{50+X}Cu_{43-X}Ni_7)Si_1$ ($-4 \leq X \leq 6$ at. %) cylindrical specimen having a diameter of 3 mm during heating, and (b) calculated transformation interval (ΔT, left) and enthalpy change (ΔH, right) as a function of Ti content.

3.5. Nano-coring structure induced by precipitation

In this study, we have induced nano-scale compositional heterogeneity through precipitation depending on the ratio of Ti and Cu in the $(Ti_{50+x}Cu_{43-x}Ni_7)Si_1$ alloy system. Through the nano-scale coring structure centered on the precipitate, it was possible to design SMAs with isotropic thermomechanical characteristics with a very wide transformation interval over 110K. Fig. 3.8. (a) shows the FESEM image of functionally graded $(Ti_{52}Cu_{41}Ni_7)Si_1$ SMA, and Fig. 3.8. (b-d) represent the schematic illustration of nano-scale coring structure centered on the Ti-rich precipitate. The precipitate absorbs the Ti content of the nearby B2 matrix, and as the distance from the matrix to the precipitate decreases, the Ti content decreases and the local transformation temperature decreases. The precipitates are several tens of nanometers in size and distributed at distances of several hundred nanometers. Fig. 3.8. (e) shows heat flow curves obtained from DSC measurement of the $(Ti_{51}Cu_{42}Ni_7)Si_1$ and $(Ti_{52}Cu_{41}Ni_7)Si_1$ specimens. It is considered that there is almost no local composition and stress field difference in $(Ti_{51}Cu_{42}Ni_7)Si_1$ specimen, because the transformation interval was very low even though it is in the as-cast state. In the case of the $(Ti_{52}Cu_{41}Ni_7)Si_1$ specimen including the nano-scale coring structure, the hysteresis $(M_p\text{-}A_p)$ is almost the same as that of $(Ti_{51}Cu_{42}Ni_7)Si_1$ specimen, but the heat flow peak is widely broadened to low temperature. It is important to note that, In the case of M_s and A_f, there is little difference between the two compositions. The reason can be inferred that the M_s and A_f appear in the B2 matrix region located relatively far from the Ti_2Cu precipitate (white region in Fig. 3.8. (b, d)). However, the lower transformation temperature, M_f and A_s appear in the much lower temperature for $(Ti_{52}Cu_{41}Ni_7)Si_1$

specimen. M_f and A_s is considered to be affected by the precipitate (shaded region in Fig. 3.8. (b, d)). The difference in transformation temperatures is evidence that the mechanism of peak broadening in heat flow curve is related to the nano-coring structure centered on Ti_2Cu precipitate. The Ti content is further lowered in a local region where the Ti_2Cu precipitate is large and densely distributed. In Fig. 3.8. (a), the precipitate size varies from a few tens of nanometers to a maximum of about 100nm, and the distance between precipitations is several tens nanometers to a maximum of about 1μm. It is considered to have a very large ΔT due to the effect of such a heterogeneous size and distribution of nano-precipitate.
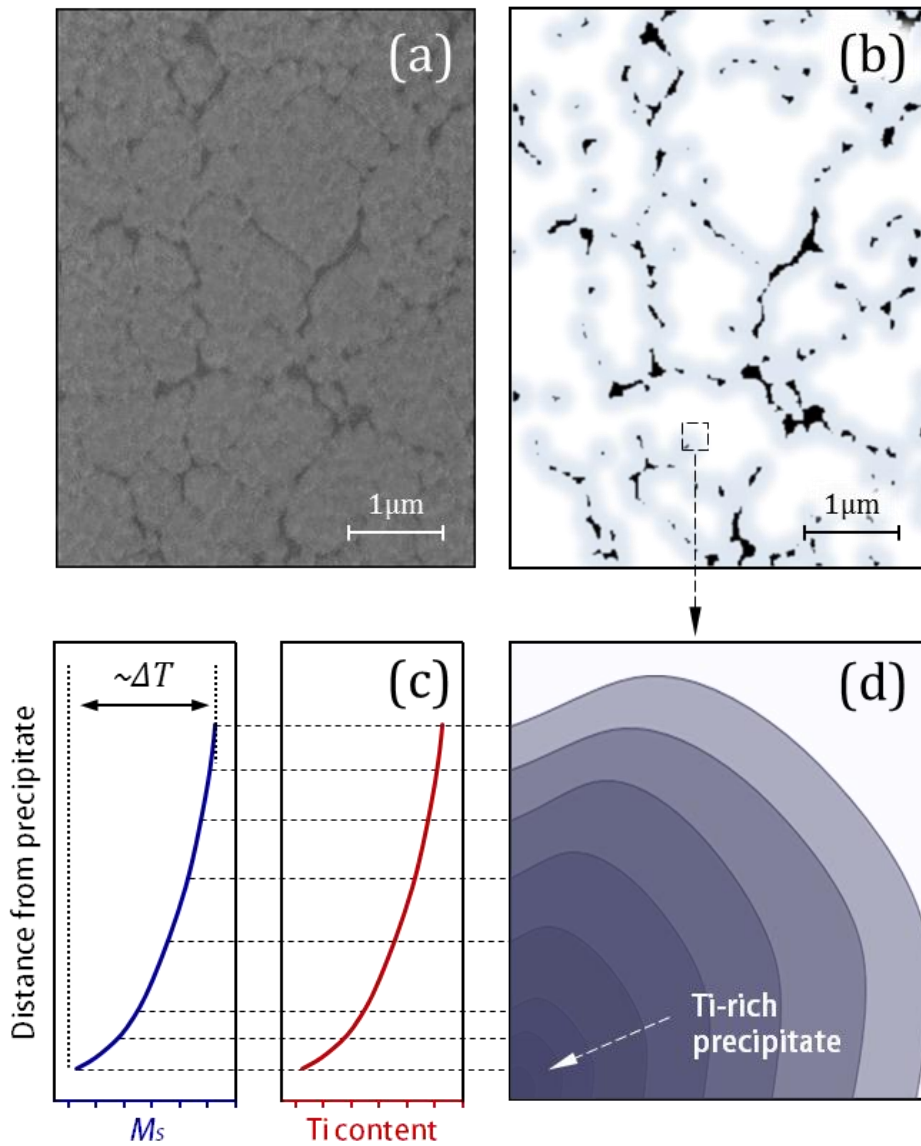
Fig. 3.8. (a) FE-SEM image of $(Ti_{52}Cu_{41}Ni_7)_{99}Si_1$, and (b) a schematic illustration of Ti_2Cu compound particles and local regions affected by the particles. (c, d) M_s and Ti content curves and schematic illustration showing the local compositional change of the B2 phase according to the distance from the Ti_2Cu compound.

3.6. Extension of Cu solubility limit by Si addition

The solid solubility of Cu on NiTi B2 was reported to be about 30at. % at a temperature of 1143K. When Cu is substituted with Ni, the MT transformation path changes as B2-B19 '→ B2-B19-B19' → B2-B19, because the B19 phase is stabilized as the Cu content increases. It has been reported that as the Cu content increases, the internal friction and transformation strain for the MT decrease, and the enthalpy change tends to increase[25]. Therefore, in the case of alloys containing a large amount of Cu, the energy dissipation due to the phase transformation is small, so there is a great potential to be utilized in certain applications such as elasto-caloric material. It is interesting to note that, by adding 1% of Si in $(Ti_{50}Cu_xNi_{50-x})_{99}Si_1$ alloy system, single B2 phase was precipitated up to 43 at.% Cu content. Figure 3.9. (a) is the schematic phase diagram of the Si-Ni-Ti-Cu quaternary system and shows how the B2 stable region $(TiNiCu)_{99}Si_1$ plane is expanded compared to the previously reported NiTiCu B2 phase region. In particular, the gray shaded region represents the area where the solid solubility of Cu is greater than 30at. %. In Fig. 3.9. (b), the *Ms* temperature of the TiNiCu alloy and the (TiNiCu)Si alloy are compared. By Si addition, the Ms was slightly lowered by 10-20 K, but the change of M_s showed a consistent tendency to increase as the increase of Cu content in accordance with the results of the NiTiCu system. It has been reported that the stability of B2 phase in NiTi binary system is higher in the Ni-rich composition than Ti-rich compostion, but in the high Cu containing TiCuNiSi alloy system, the B2 phase in the Ti-rich composition is more stable than in the Cu-rich B2 phase. In addition, the alloys in the Ti-rich composition retains a high enthalpy change and has a very wide transformation interval, which is represented as a functionally graded zone in Fig. 3.9. (a).
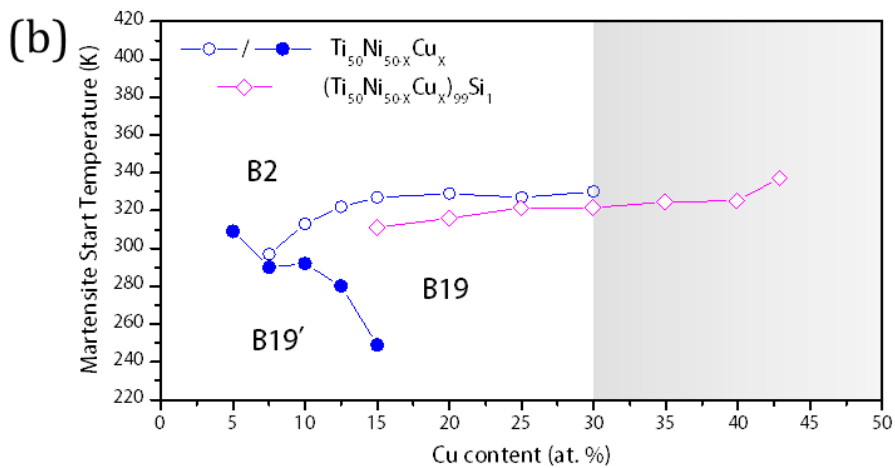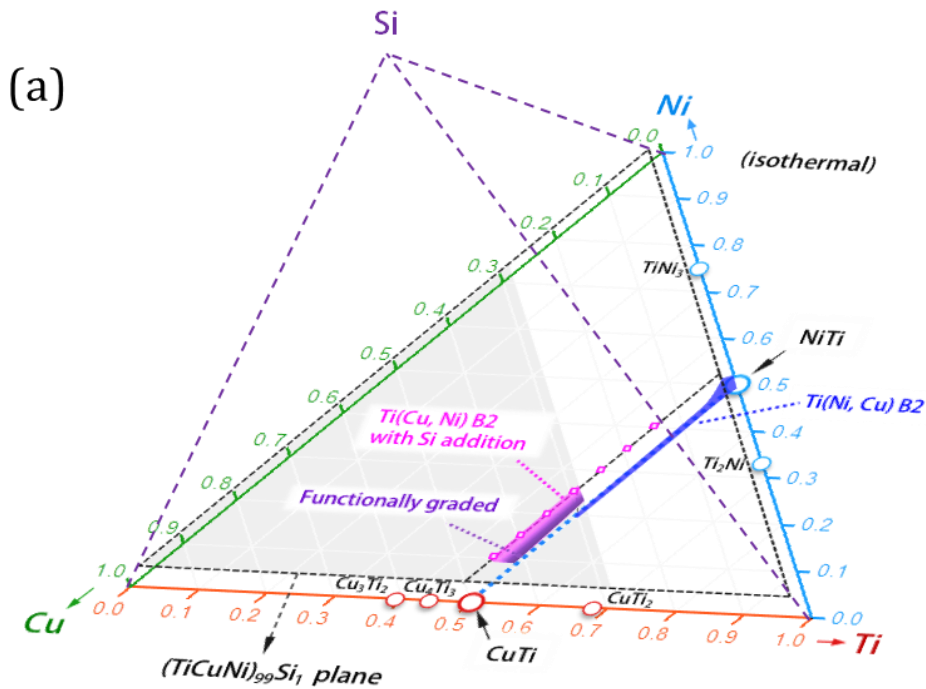
Fig. 3.9. (a) Schematic isothermal phase diagram of TiCuNiSi quaternary alloy system. The blue area on the TiCuNi ternary phase diagram represent the reported TiCuNi B2, and the magenta area on the $(TiCuNi)_{99}Si_1$ plane shows the TiCuNiSi B2 having Cu content over 30%. (b) Martensite start temperature (M_s) of TiCuNi and TiCuNiSi SMAs, as a function of Cu content.

Chapter 4.

Tailoring martensitic transformation

4.1. Development of TiCuNiSiSn quinary shape memory alloys

We investigated the effect of Sn addition as a solute element on the martensite phase transformation and mechanical properties of TiCuNiSi alloys. The HRPD measurement results of the cylinder specimens of $(Ti_{51}Cu_{41}Ni_7Si_1)_{100-X}Sn_X$ (X=0, 1, 2, 3, 4, 5, and 6 at. %) compositions are shown in Fig. 4.1 It can be seen that the B19 martensite phase and B2 austeniste phase were precipitated simultaneously at the Sn concentration of 0 and 1 at. %, and the B2 phase precipitated at the Sn concentration of 2, 3, 4, and 5 at. %. Only the specimen of Sn6 showed an unknown precipitate phase other than B2 and B19. It is considered the martensitic transformation temperature decreases as the Sn content increases.

The compression test results of the 3mm cylinder specimens of $(Ti_{51}Cu_{41}Ni_7Si_1)Sn_x$(X=1, 2, 3, 4, and 5) compositions selected as representatives are shown in Fig. 4.3 (a). In the compressive stress-strain curves of Sn2 ,3, 4 and 5, typical double-yielding behavior was found. The first apparent yielding appears to be a stress-induced MT from B2 phase to B19 phase. The first piece of evidence for stress-induced MT is that the stress level of the first apparent yielding of the Sn2 composition lay within the critical stress range of 420 to 570 MPa of the stress-induced martensitic phase transformation observed in in-situ neutron

diffraction measurement that is shown in fig. 4.3 (b). The neutron diffraction patterns measured under compressive stress on a 3 mm diameter and 6 mm height cylinder specimen. As the compressive deformation progresses, the B2 lattice deformed through the elastic deformation, and the position of the B2 phase peak gradually moved to the left and the width became wider. When compressive stress reached the critical stress level for MT, the B2 phase peak disappeared, and the B19 phase peak occurred. The results indicate that the critical stress at which martensitic phase transformation occurred from the B2 phase to the B19 phase was between 420 MPa and 570 MPa. Additionally, as deformation proceeds, the B19 phase peak also shifted to the left, and the width gradually widened, indicating that B19 phase elastic deformation had occurred. The second piece of evidence for stress-induced MT is that the first apparent yielding was followed by a constant deformation stage, which is considered the elastic deformation zone of the B19 martensite phase. After the elastic deformation zone of the B19, the second apparent yielding due to the yield of the martensite phase was observed. The maximum stress values in all alloy compositions were very similar from 2335 to 2450 MPa, and the strain-hardening rates after yielding were also similar. In contrast, the stress-strain curves of the Sn1 composition give rise to strain plateu at low stresses below 100 MPa at the early stage of deformation, which is considered to be due to the detwinning of the B19. The specimens of alloy composition with lower Sn content, which started plastic deformation through the second apparent yielding at lower stress, showed plastic deformation and work hardening behavior in a wider range of strain, exhibited high fracture strain and absorbed energy values. As a result, specimens with lower Sn content, which

initiated plastic deformation through the second apparent yielding at lower stresses, exhibited plastic deformation and work hardening behavior in a wider range of strain and higher absorbed energy.

Fig. 4.2(a) shows the DSC traces obtained from the $(Ti_{51}Cu_{41}Ni_7Si_1)_{100-x}Sn_x$ (X=0-3 at.%) SMAs. All the DSC traces exhibited reversible MT between B2 austenite and B19 martensite. Table 4.1. shows the martensitic phase transformation start temperatures(M_s) measured by the DSC and TDO equipment, the Vickers hardness (H), first apparent yield stress by martensitic phase transformation(σ_{Ms}), second apparent yield stress by yielding of martensite phase($\sigma_{y,M}$), energy absorbed by compressive deformation until fracture occurred(E_{ab}) and fracture strain(ε_F) of 3 mm diameter cylinder specimens of $(Ti_{51}Cu_{41}Ni_7Si_1)Sn_x$ ($0 \leq x \leq 5.5$ at. %). As the concentration of Sn increased, the phase transformation temperature, fracture strain, and absorption energy decreased, but the hardness, phase transformation stress and yield stress of martensite tended to increase. It is considered that the mechanical properties and the MT temperature change systematically according to the content of Sn.
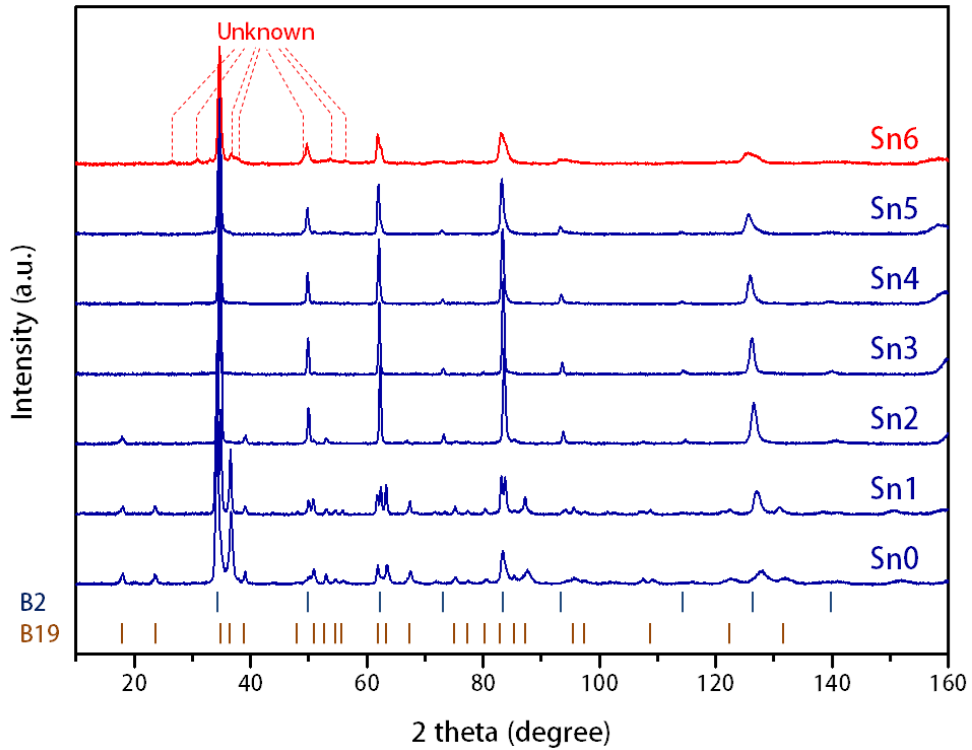
Fig. 4.1. High resolution powder diffraction (HRPD) pattern measurement results of $(Ti_{51}Cu_{41}Ni_7Si_1)_{100-X}Sn_X$ (X=0, 1, 2, 3, 4, 5, and 6 at. %). Only the B2 and B19 phases were detected in the composition between Sn0 and 5, but the unknown phase was precipitated in the Sn6 composition, and therefore the B2 stability limit was judged to be between Sn5 and 6.
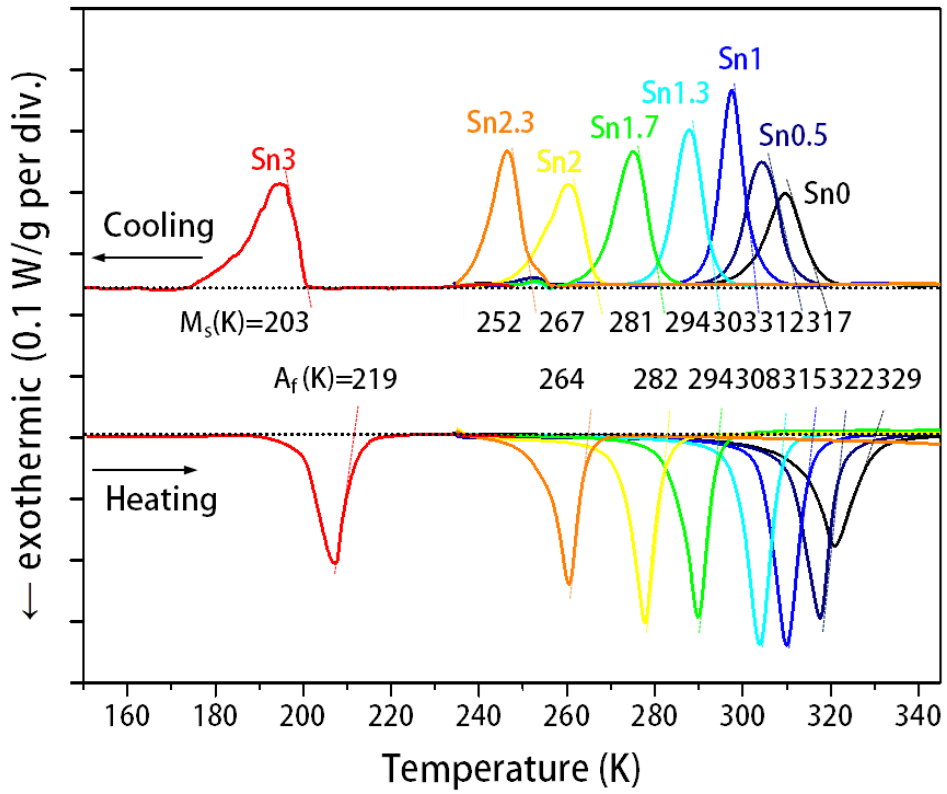
Fig. 4.2. Plots of DSC traces of $(Ti_{51}Cu_{41}Ni_7Si_1)_{100-X}Sn_X$ (X=0-3 at. %) alloys. Martensite start temperature (M_s) and austenite finish temperature (A_f) is obtained by the tangent line of endothermic and exothermic peak. Enthalpy change during martensitic transformation is obtained by the integration of the peaks.
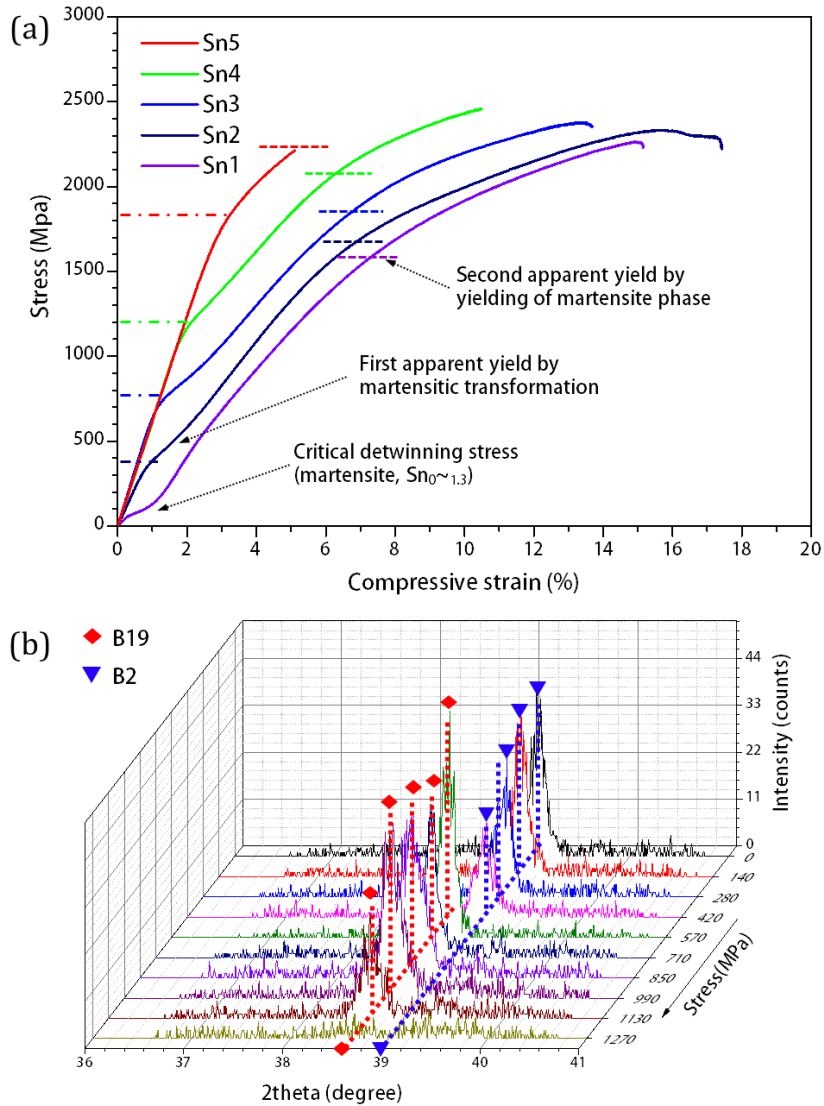
Fig. 4.3. (a) Compressive stress-strain curves of 3mm cylinder specimens with composition of $(Ti_{51}Cu_{41}Ni_7Si_1)_{100-x}Sn_x$ (x=1, 2, 3, 4, and 5 at.%). With increasing Sn contents, stress-strain curves systematically changes depending on the martensite transformation related characteristics such as transformation stress (σ_{Ms}, first yielding) and yield stress B19 martensite phase (σ_y, second yielding). (b) In-situ neutron diffraction spectra of as-cast $(Ti_{51}Cu_{41}Ni_7Si_1)_{98}Sn_2$ cylindrical specimen having a diameter of 3 mm under uniaxial compressive loading.

7 3

Table. 4.1. Characteristic temperatures (M_s, M_f, A_s, A_f, M_p, and A_p) and enthalpy change of MT (ΔH)

Alloy composition (at.%)	M_s (K)	M_f	A_s	A_f	M_p	A_p	$\Delta H_{A \to M}$	$\Delta H_{M \to A}$
$(Ti_{50}Cu_{15}Ni_{35})Si_1$	311.5	293.1	305.2	321.6	303.1	315.3	-14.507	12.567
$(Ti_{50}Cu_{20}Ni_{30})Si_1$	313.3	300.4	312.8	323.0	307.0	319.9	-13.062	12.215
$(Ti_{50}Cu_{25}Ni_{25})Si_1$	316.3	305.1	318.7	326.9	311.0	323.8	-12.589	11.471
$(Ti_{50}Cu_{30}Ni_{20})Si_1$	321.9	309.8	321.6	330.7	316.7	327.4	-12.232	11.125
$(Ti_{50}Cu_{35}Ni_{15})Si_1$	324.8	310.5	320.6	332.2	318.0	328.2	-11.83	10.999
$(Ti_{50}Cu_{40}Ni_{10})Si_1$	325.2	312.9	323.4	332.9	319.7	329.6	-10.3351	9.239
$(Ti_{50}Cu_{43}Ni_7)Si_1$	339.7	317.5	327.1	344.1	326.3	334.8	-10.421	10.561
$(Ti_{50}Cu_{45}Ni_5)Si_1$	-	-	-	-	-	-	-	-
$(Ti_{56}Cu_{37}Ni_7)Si_1$	317.3	255.4	259.7	329.0	299.5	305.3	-2.448	2.040
$(Ti_{55}Cu_{38}Ni_7)Si_1$	349.3	251.3	245.7	359.5	305.4	309.9	-0.468	2.120
$(Ti_{54}Cu_{39}Ni_7)Si_1$	349.7	243.1	246.1	357.5	312.7	317.9	-1.274	6.291
$(Ti_{53}Cu_{40}Ni_7)Si_1$	347.5	260.3	250.4	355.4	310.9	317.9	-3.065	7.906
$(Ti_{52}Cu_{41}Ni_7)Si_1$	345.6	249.5	261.7	357.5	305.7	307.6	-4.087	8.820
$(Ti_{51}Cu_{42}Ni_7)Si_1$	329.0	312.4	323.5	335.8	319.4	331.5	-8.664	8.622
$(Ti_{50}Cu_{43}Ni_7)Si_1$	332.8	310.7	327.7	341.9	323.1	336.5	-8.580	9.860
$(Ti_{49}Cu_{44}Ni_7)Si_1$	330.8	261.5	253.2	339.3	315.7	324.5	-4.144	4.181
$(Ti_{48}Cu_{45}Ni_7)Si_1$	326.7	-	253.5	342.0	303.1	312.4	-2.259	2.125
$(Ti_{47}Cu_{46}Ni_7)Si_1$	316.2	-	253.3	342.2	277.2	286.7	-2.983	2.319
$(Ti_{46}Cu_{47}Ni_7)Si_1$	315.7	-	251.0	355.2	278.2	289.5	-2.142	3.035

Fig. 4.4. Plots of martensitic transformation start temperature (M_s) dependence of absorbed energy(blue triangle), phase transformation stress(black circle), yield stress of martensite(green triangle), and compressive elongation(red square).

4.2. Compositional dependence of martensite start temperature

4.2.1. Compositional dependence of internal friction

Effect of solute element can be reflected in the internal friction and modulus of the alloys [18-23], and DMA measurement during continuous heating was performed to investigate the effect of addition of solute element Sn. The obtained storage modulus and $\tan\delta$ value are shown in Fig. 4.5. (b). The storage modulus represents stiffness [24], and the $\tan\delta$ is the direct measurement of internal friction caused by shuffling during MT and the twin boundary motion of the martensite phase. Fig. 4.5. (a) shows the heat-flow curve measured by DSC during heating. The temperature range of the exothermic peak due to the B19 to B2 MT during continuous heating can be identified. Fig. 4.5. (a) and Fig.4.5 (b), the storage modulus and $\tan\delta$ values for the B19 phase and B2 phases can be determined. As the Sn content increased, the storage modulus of the B2 phase increased markedly. In the B19 martensite phase, the increase in the storage modulus was not significant, but the internal friction ($\tan\delta$) increased significantly, indicating that the internal friction during the twin boundary motion increased. In addition, the peak values of the $\tan\delta$ curve also increased with increasing Sn content, which means that internal friction caused by shuffling of the basal plane during MT increased. This result implies that the strengthening mechanism by Sn addition worked in both the B2 phase and the B19 phase.
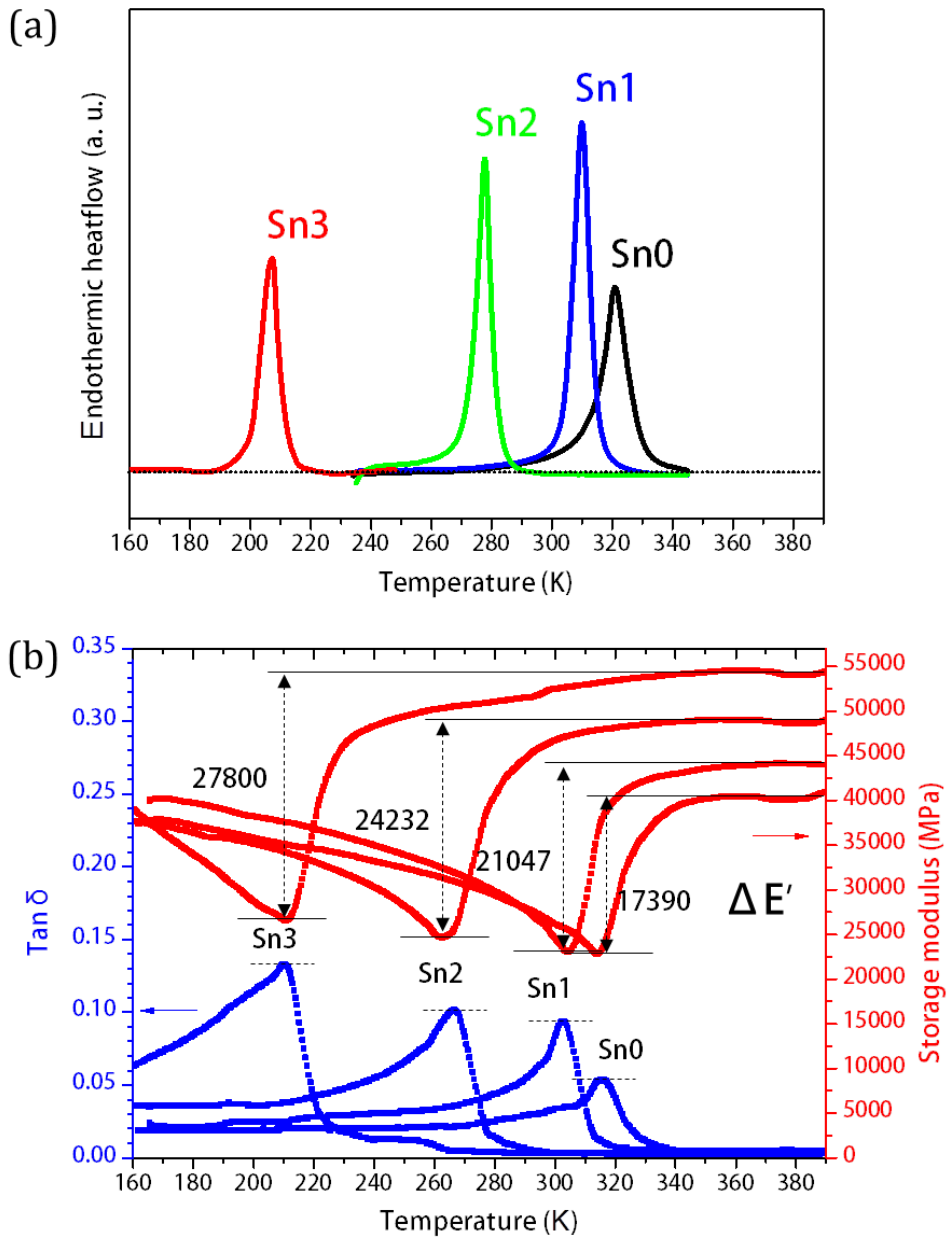
Fig. 4.5. (a) DSC traces and (b) curves of Tanδ (left) and storage modulus (right) of 3mm cylinder specimens with composition of $(Ti_{51}Cu_{41}Ni_7Si_1)_{100-x}Sn_x$ (x=0, 1, 2, and 3 at.%).

4.2.2. Driving force for martensite nucleation

Fig. 4.2(a) shows the DSC traces obtained from the $(Ti_{51}Cu_{41}Ni_7Si_1)_{100-x}Sn_x$ (x=0-3 at.%) SMAs. All the DSC traces exhibited reversible MT between B2 austenite and B19 martensite. With increasing Sn contents, the M_s decreases from 317 K in Sn0 to 203 K in Sn3. The M_s and A_f are marked by dashed tangent lines in the DSC traces. Based on the equation: $T_0 = (M_s + A_f)/2$ [25, 26], the value of T_0-M_s of SMAs in this study is considered to be quite small, below ~8 K, signaling the SMAs exhibit thermoelastic MT [4]. The driving force for martensite nucleation($-\Delta G_{Ms}$) was calculated by adopting Turnbull's equation: $\Delta G = \frac{\Delta H \Delta T}{T_0} = \Delta H(\frac{T_0-M_s}{T_0})$ [27]. ΔH (B2→B19), $T_0 = (M_s + A_f)/2$ are obtained from DSC data in Fig. 4.2, and $-\Delta G_{Ms}$ is calculated. It should be noted that as the ΔH and T_0-M_s values increased, $-\Delta G_{Ms}$ tended to increase. To investigate the origin of the Sn effect on this phenomenon, we considered the following equation of the critical driving force for martensite nucleation in the athermal regime induced by Ghosh and Olson [28]:

$$-\Delta G = \Delta A\gamma + \Delta V E_{ela} + W_F \qquad (1)$$

, where ΔG is chemical free energy, $\Delta A\gamma$ is interfacial energy, $\Delta V E_{ela}$ is elastic strain energy, and W_F is internal frictional work. We have tried to apply equation (1) for the B2 - B19 thermoelastic MT of TiCuNiSiSn alloys, where ΔG is equal to ΔG_{Ms} in that thermal activation can be neglected. In addition, since the values of the second eigenvalue (λ_2) of the transformation matrices of B2 to B19 MT are very close to 1, ranging from 0.995 to 0.999, it can be assumed that the alloys have compatible arrangement of martensite, and the variation of interfacial energy

$(\Delta A\gamma)$ and elastic strain energy (ΔVE_{ela}) generated by the MT are negligible [29-31] Therefore, the equation (1) can be approximated by the following equation :

$$-\Delta G_{Ms} = K_1 + W_F \qquad (2)$$

, where K_1 is a constant. Since B2-B19 MT is athermal, the thermal term of W_F was not taken into account even in the cryogenic temperature. Because the relative atomic ratio of the base alloy $(Ti_{51}Cu_{41}Ni_7Si_1)$ is maintained, and MT path (B2-B19) is not affected by the addition of Sn, resulting in a consistent increase in internal strength, the $(Ti_{51}Cu_{41}Ni_7Si_1)_{100-X}Sn_X$ alloy system can be assumed to be a TiCuNiSi-Sn pseudo-binary system. Accordingly, the increase of athermal internal frictional work (ΔW_F) of TiCuNiSi-Sn pseudo binary alloy can be described by the functional form of $K_{Sn}X_{Sn}^t$ associated with solid solution hardening (SSH) theories [5, 19, 32]. As a result, driving force for martensite nucleation in the SMAs is given by :

$$-\Delta G_{Ms} = G_0 + K_{Sn}X_{Sn}^t \qquad (3)$$

, where G_0 is a constant, K_{Sn} is strength coefficient, X_{Sn} is concentration of Sn, and t is solute exponent. The equation (3) implies the MT behavior significantly depends on SSH. It should be noted, therefore, that the TiCuNiSiSn alloy system is considered to be a suitable model system for investigating the effect of point defect hardening on MT. In particular, the exponent t is an important factor related to compositional dependence of solid solution hardening. For the athermal driving force of Fe-X and Ti-X binary alloys, the value of $t = 1/2$(or 2/3) and $t=1.5$ have been accepted respectively [30, 33-35]. We obtained the value of $t=1.94$ for TiCuNiSiSn alloy system by fitting the equation (3) to the measured $-\Delta G_{Ms}$ data from DSC results. As shown in Fig. 4.7, the best fit was obtained with the

following formula: $-\Delta G_{Ms} = 0.12 + 0.017X^{1.94}$ (J/g). Fig. 4.8 shows a plot of M_s measured by DSC (blue closed circle) versus Sn content. The M_s data were fitted by the equation $M_S = M_S^0 + CX_{Sn}^t$ using t=1/2 (Fleisher [36], dot line), t=2/3 (Rabusch [18], dash-dot line), 1.5 (Neelakantan [30], dash line), and 1.94 (this work, solid line). When the exponent t value is 1.5 proposed by Neelakantan in the Ti-X system or 1.94 obtained from this study, a comparable agreement with experimental data was obtained in the temperature range above 150K where DSC measurement is available with LN2 cooled type chiller. However, a large difference is revealed between the two fitted curves in the region of non-measurable temperature below 150K. Moreover, it is essential to ascertain the fundamental question as to whether MT can actually occur at a cryogenic temperature close to 0K, since no SMA system has ever been reported where M_s can actually be modulated up to the ultra-cryogenic region.
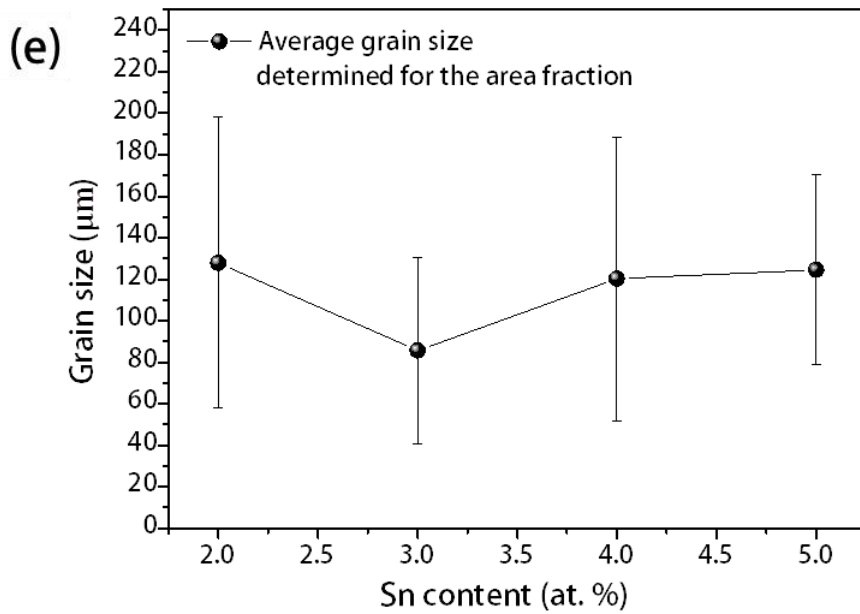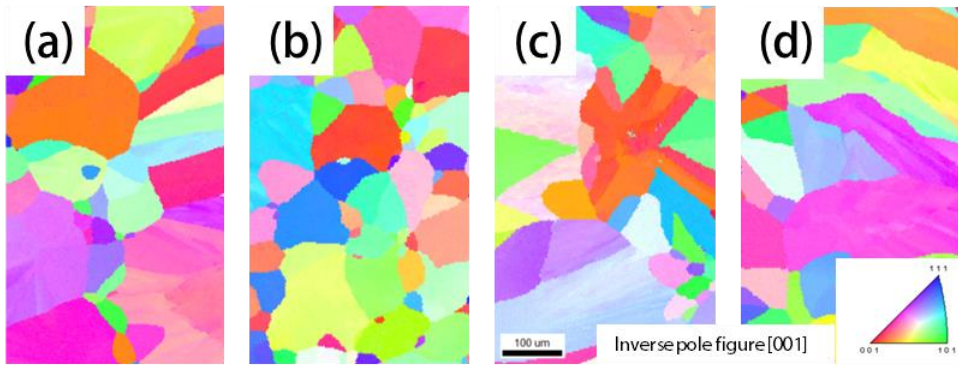
Fig. 4.6. EBSD orientation map of $(Ti_{51}Cu_{41}Ni_7Si_1)_{100-X}Sn_X$ (X = 2, 3, 4, 5 at. %) alloys (a-d) and the average grain size taken from each scan (e). Average grain size is determined for the area fraction.
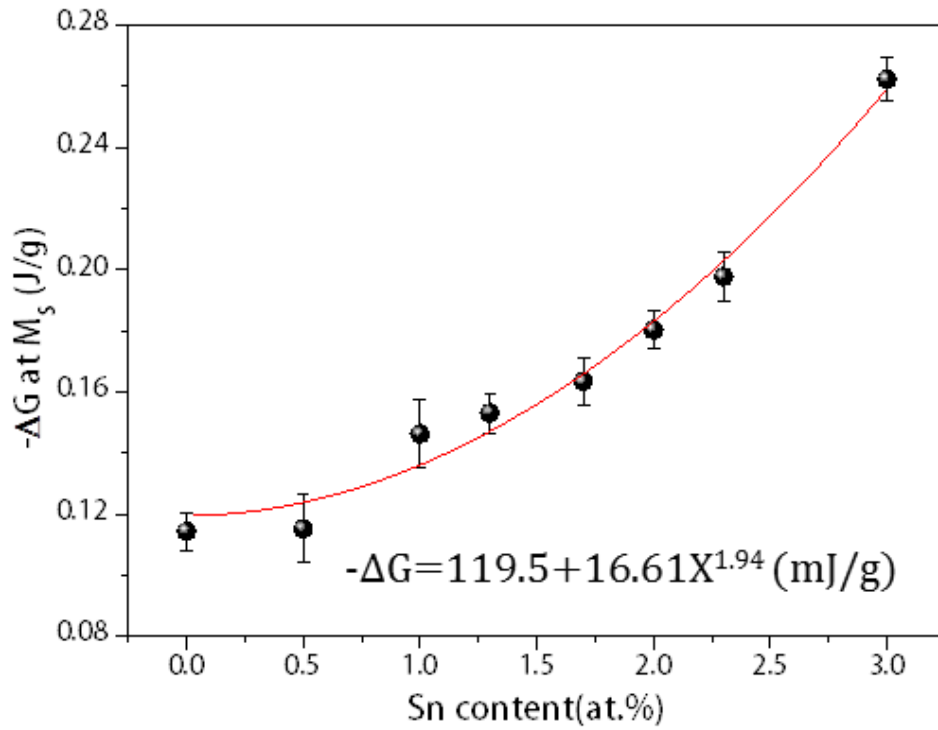
Fig. 4.7. Measured driving force for martensite nucleation of B2 to B19 transformation in TiCuNiSiSn alloy system according to content of Sn element.

4.2.3. Cryogenic measurement of martensitic transformation and exponent of athermal flow stress

We measured characteristic temperatures of MT in cryogenic temperature by home-built TDO. The detailed description of our TDO setup is provided in ref [37]. As a result of TDO measurement, MT behavior with M_s at the lowest temperature of 14.5 K was actually confirmed, and it was considered that M_s could be easily controlled only by the addition of Sn within 5% from RT to a cryogenic temperature close to 0K. As can be seen in Fig. 4.8, the TDO results and the fitted curves with four different solute exponent t values of M_s show that the best agreement is obtained at t = 1.94, especially in the cryogenic region. The fitted equation was obtained as follows [34, 38] :

$$M_s = 316.68 - 13.24 \times X_{Sn}^{1.94} \text{ (K)} \qquad (4)$$

It is interesting to note that the solute exponent $t{=}1.94$, which represents the hardening tendency, is also the most important factor explaining the compositional dependence of M_s. We have assumed that the t value reflects the point defect hardening behavior and that this behavior depends on the site preferences of the containing element.
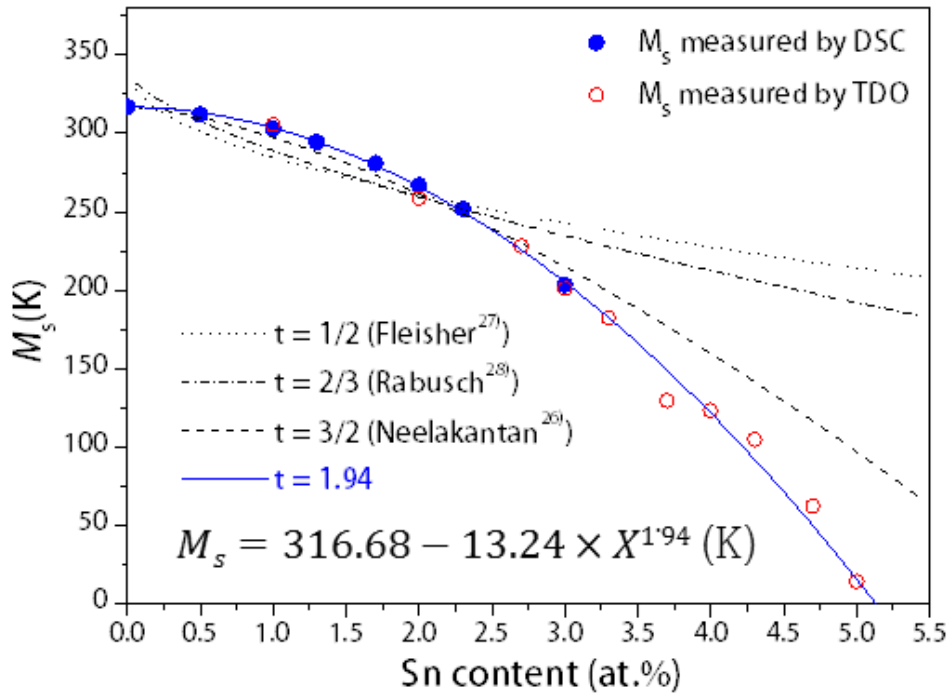
Fig. 4.8. Plots of M_s measured by DSC (blue closed circle) and TDO (red open circle) versus Sn contents. DSC results were fitted by the equation $M_s = M_s^0 + CX_{Sn}^t$ with $t=1/2$(Fleisher), 2/3(Rabusch), 1.5(Neelakantan) or 1.94(this work).

4.3. Correlation between martensite start temperature and mechanical properties

4.3.1. Solid solution hardening by antisite defect

Ab-initio methods were used to analyze the site preference of Sn element added on TiCu B2 phase [39-44]. Four special quasirandom structures (SQS) [15] have been considered in the Ti-rich or Cu-rich compositions in which Sn is preferred to Ti-site or Cu-site. The descriptions of the SQS structures are shown in Fig. 2.9. The calculated ground state energies of these four structures were -184.6594(Ti-rich, without ASD), -184.7395(Ti-rich, with ASD), -180.6613(Cu-rich, without ASD) and -181.0341(Cu-rich, with ASD) eV respectively. The SQS with lower ground state energy indicates the site preference of Sn for each composition. It is considered that Sn element shows a preference for a site that forms ASD in TiCu B2 phase. This result essentially implies that Sn addition c1an cause a severe hardening effect on the B2 lattice due to the formation of additional point defects.

Fig. 4.9 (a) shows schematics for describing three types of point defects, solute defects, antisite defect (ASD), and triple defect (TRD) that can be generated when the B atom is replaced by a solute element. First, if a solute atom has a preference for B atom site, only the solute atom itself can be a point defect. However, if the solute atom has a preference for A atom site, it can form ASD or TRD. ASD is generated as point defect of the solute atom and A atom in B site, and in case of TRD, solute atom defect and constitutional vacancies are generated. The ASD and constitutional vacancies have been reported to cause much more severe solid

solution hardening effects than a substitutional solute atom in B2 phase [45]. In general, it is difficult to describe the hardening effect of each type of defect individually. It is because most ordered alloys are in a hybrid defect state in which ASD and vacancies coexist [46], and the measurement of the concentration is possible only if the sample is manufactured in a specific form of single crystal or micro powder. On the other hand, by the solute exponent t obtained from DSC results, we could easily find the hardening tendency that reflects the hybrid defect state even though we cannot directly know the concentration of each kind of point defect [47-49]. For equibinary alloys and ternary alloys of $(Ni-X)_{50}(Ti-Y)_{50}$ ($X = Pd$, Pt or Cu, Y=Hf) systems in which the austenite has B2 structure, the effect of ASD and constitutional vacancies generated by solute atoms need not be considered [15]. Fig. 4.9 (b) shows M_s of the SMA systems with as a function of the valence electron concentration c_V (number e_V of valence electrons divided by the total number e_{total} of electrons) [2, 4, 50, 51]. It is considered that the broad tendency can be rationalized by the relationship between M_s and c_V proposed by Zarinejad and Liu [52]. They found that M_s almost linearly decreases with increasing c_V, because the increase of the c_V increases the value of the shear modulus, which is a measure of the resistance to the shape change and MT. This tendency suggests that M_s heavily depends on the valence electron effect. It is interesting to note that the c_V depedence of M_s in TiCuNiSiSn alloys deviates from the reported trend as shown in Fig. 4.9 (b). We presumed that M_s depends on the point defect hardening by Sn addition rather than the valence electron effect. To examine our assumptions, it was necessary to investigate the tendency of ASD and vacancy generation by Sn addition.
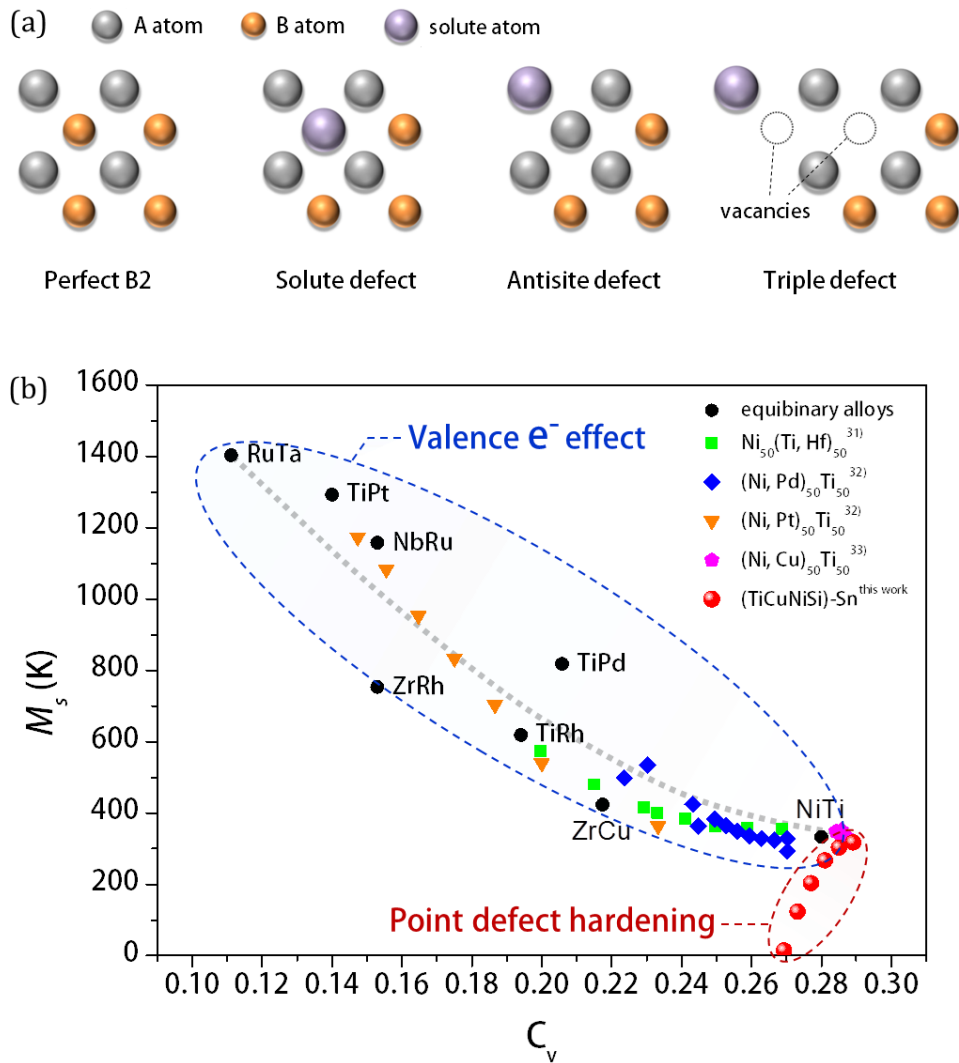
Fig. 4.9. (a) Schematics for describing three types of point defects, solute defects, antisite defect (ASD), triple defect (TRD). (b) M_s of the SMA systems with as a function of the valence electron concentration c_V (number e_V of valence electrons divided by the total number e_{total} of electrons).

4.3.2. Compositional dependence of mechanical properties

The evidence that Sn addition generates an additional point defect could also be found in the measurement results of the mechanical properties of the alloys. Table 4.2 summarizes the physical properties of $(Ti_{51}Cu_{41}Ni_7Si_1)_{100-x}Sn_x$ (x=0-5.5 at.%) alloys. In particular, an abnormal hardening behavior was reflected in shear modulus measurement results. The shear modulus of Sn element is reported as 18 GPa, which is much lower than that of Ti (44), Cu (48), Ni (76) and Si (80). According to SSH theory, the fractional change in shear modulus $\varepsilon_G = \frac{1}{G}\frac{dG}{dc} = -0.59\,(GPa/at.\%)$ [32, 37, 53, 54], indicate a slight negative change as the Sn content increases [55]. However, the actual shear modulus of bulk specimens measured by ultrasonic measurements show a very high positive fractional change in shear modulus of $\varepsilon_G = 7.84\,(GPa/at.\%)$. In addition, it can be seen that the yield stress (σ_y) obtained from the compression test increases rapidly from 1501 MPa to 2329 MPa by adding a small amount of substitutional element Sn. It is difficult to understand the abnormal phenomenon as a conventional SSH behavior, and there should be additional hardening components such as ASD and constitutional vacancy. Fig. 4.3 shows stress-strain curves obtained from the compression test results. It can be clearly seen that the critical stress for stress-induced MT (σ_{MT}) systematically increases by Sn addition. The compositional dependences of σ_{Ms} and σ_y is given by the following equations based on SSH :

$\sigma_{Ms} = 65.5 + 76.0 \times X_{Sn}^{1.94}(MPa)$, $\sigma_y = 1450 + 45.0X_{Sn}^{1.94}$ (MPa). It is important to note that the hybrid defect state cause by Sn addition is represented by the solute

exponent t=1.94 in equation (4), which means that there is a close correlation between the mechanical properties and the MT with respect to point defect hardening. We show the correlation of M_s with σ_{MT} and yield stress in Fig. 4.10. We found the relations can be expressed as the equations : $\sigma_y = 2467.1 - 3.18 \times M_S$ and $\sigma_{MT} = 2053.4 - 6.45 \times M_S$. We proposed a concrete method of controlling the characteristics related to MT through alloy design using the correlations. We also provide equations to predict MT-related mechanical properties such as hardness. In thermoelastic TiCuNiSiSn SMAs, the hardening exponent t mainly represents compositional dependence of internal friction stress. Fig. 4.11 shows plots of the measured Vickers hardness and M_s versus Sn contents. With increasing Sn contents, the hardness value also increases nonlinearly. The increase in internal frictional stress is correlated with Sn content: (eg. $\Delta\tau_{Sn} \propto X_{Sn}^{t'}$). Thus, the increase of hardness can be reasonably expressed by the following equation:

$$H = H_0 + BX_{Sn}^{t'}$$

, where H_0 and B are constant.

3-point bending and fracture toughness measurement results are shown in Fig. 4.12. The critical stress for MT has a low stress level in the 3-point bending result for relatively low-Sn compositions. It also shows low-Sn compositions have low modulus and good ductility, which is compared with the compression test result. In the case of fracture toughness results, a sample exceeding Sn2 with B2 single phase showed brittle fracture without crack propagation. Sn0 and Sn1 samples showed high K_{IC} values due to deflection and crack propagation at low stress due to martensite reorientation.
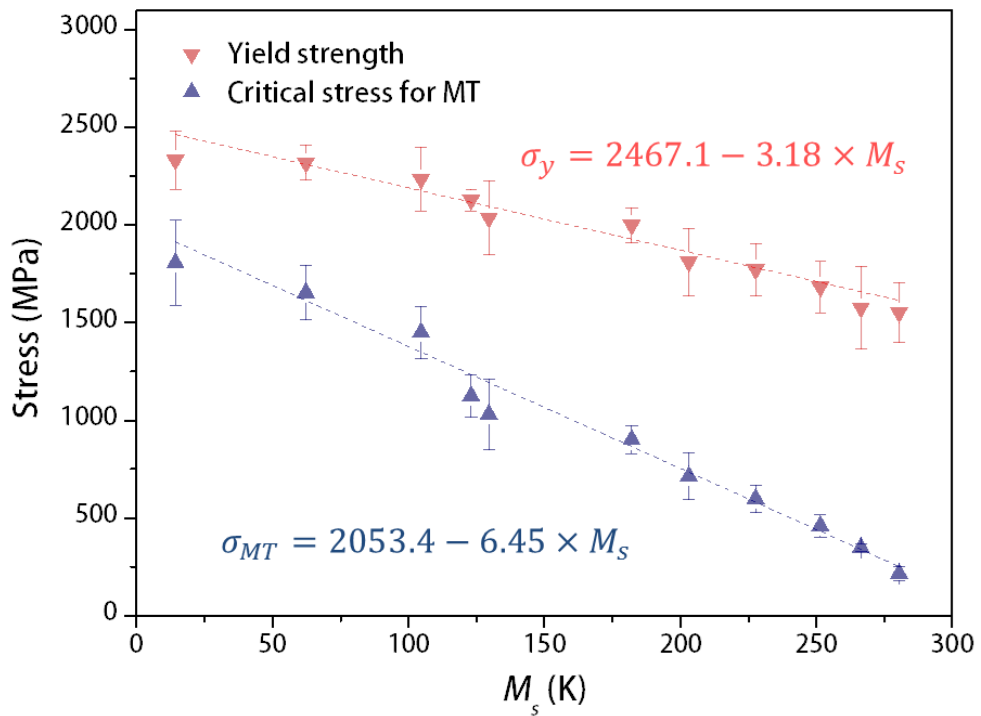
Fig. 4.10. Plots of yield strength and critical stress for stress-induced MT obtained from compression test results. The inserted doted lines represent the correlation between MT and strength.
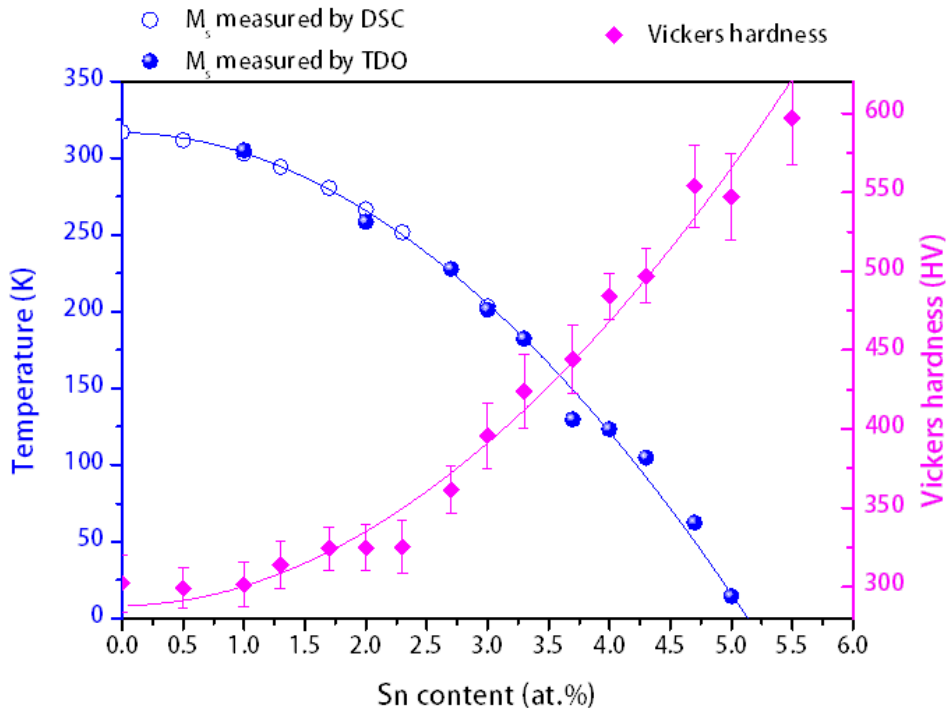
Fig. 4.11. Compositional dependence of martensite start temperature and Vickers hardness of $(Ti_{51}Cu_{41}Ni_7Si_1)_{100-X}Sn_X$ ($X \leqq 5.5$ at. %). Addition of solute element Sn induce solid solution hardening and increase of Vickers hardness according to the trend with hardening exponent t=1.94. Decrease of M_s related to the increase of shear modulus by the hardening behavior.
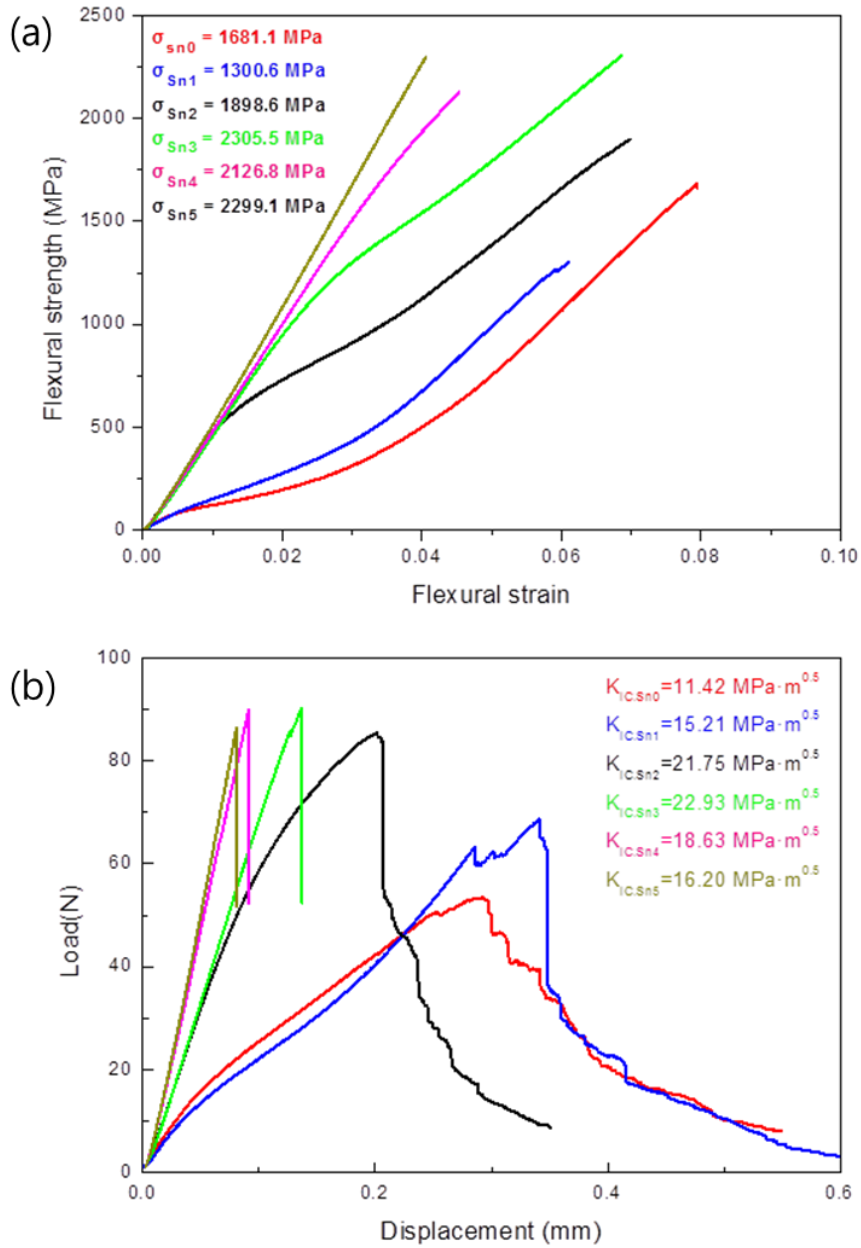
Fig. 4.12. 3-point bending(a) and fracture toughness test(b) results of $(Ti_{51}Cu_{41}Ni_7Si_1)_{100-X}Sn_X$ (X = 0, 1, 2, 3, 4, 5 at. %) are shown. Deflection in Sn0, Sn1 is come from rearrangement of the B19 martensite since the samples are in a fully martensite. Sn3, 4, and 5 showed brittle fracture. Sn0, 1, and 2 have a little ductility.

Table 4.2. Measured characteristic temperatures of MT (M_s, M_f, A_s, A_f) and Vickers hardness of $(Ti_{51}Cu_{41}Ni_7Si_1)_{100-x}Sn_x$ (x=0 - 5.5 at.%) alloys

Sn content (at.%)	DSC / TDO (K)				Critical stress for MT (MPa)	Yield stress (MPa)	Shear modulus (GPa)
	M_s	M_f	A_s	A_f			
0	316.7	301.3	313.4	328.9	-	1501±135	-
0.5	311.7	296.4	309.7	322	-	1524±114	-
1	302.9	291.8	303.4	315.2	-	1530±97	-
	305.3	297.5	301.1	309.9			
1.3	294.3	281	297.2	307.6	-	1529±178	-
1.7	280.7	266.7	283.4	293.9	212.5±34	1549±152	-
2	266.7	250.7	271.7	281.9	345.1±21	1573±210	28.1±0.2
	258.4	219.6	238.7	273.4			
2.3	251.8	238.8	254.5	264.4	455.5±56	1679±131	-
2.7	227.9	221.3	226.4	236.9	595±71	1768±132	-
3	203.4	182.6	199.5	219.3	711.4±121	1808±172	29.4±0.2
	201.1	170.1	181.7	219.6			
3.3	182.3	168.1	180.6	187.6	899.1±71	1995±89	-
3.7	129.8	119.2	129.5	146.1	1028±181	2033±191	-
4	123.3	105.4	117.2	155.7	1122±110	2125±56	31±0.3
4.3	104.9	93.51	104.8	117.1	1447±134	2231±162	-
4.7	62.5	47.9	44.2	55.4	1651±141	2314±89	-
5	14.5	-	18.6	28.1	1803±217	2329±149	33.8±0.3
5.5	-	-	-	-	2060±131		

9 3

4.4. Analysis of deformation mechanism of superelastic alloys

4.4.1. In-situ neutron diffraction measurement

As shown in fig. 4.3, significant work hardening after yielding occurred. The second phase is a soft cubic structure and the martensite has soft orthorhombic structure. The phase transformation of the second phase during the deformation of the composite was investigated by Residual Strain Instrument(RSI, HANARO, KAERI, Korea). In-situ neutron diffraction under uniaxial compressive loading is used to show the phase change of the second phase inside the composite during deformation. Internal volume is measured in the area of $2 \times 2 \times 2\text{mm}^3$ for 3mm rod samples. The lattice strain of the martensite phase was calculated based on the initial values obtained by extrapolating the strain points linearly. As the stress level increased, the peak intensity became low, and the noise tends to be severe. After the smooth treatment, the peak position was determined by gaussian fitting, as shown in fig 4.13(a). The MT behavior induced by stress field could be clearly seen. Depending on the applied pressure, the entire specimen undergoes a MT change to martensite. The change in lattice strain of the B2 phase and martensite occurs almost linearly with the pressure. Fig. 4. 13. (b) shows the phase map of deformed $Ti_{49}Cu_{41}Ni_7Si_1Sn_2$ rod specimen measured by electron back scattered diffraction (EBSD). The B19 martensite laths were remained after the cyclic deformation.
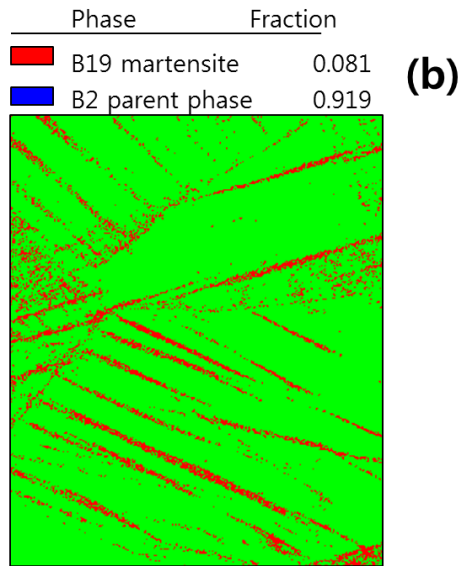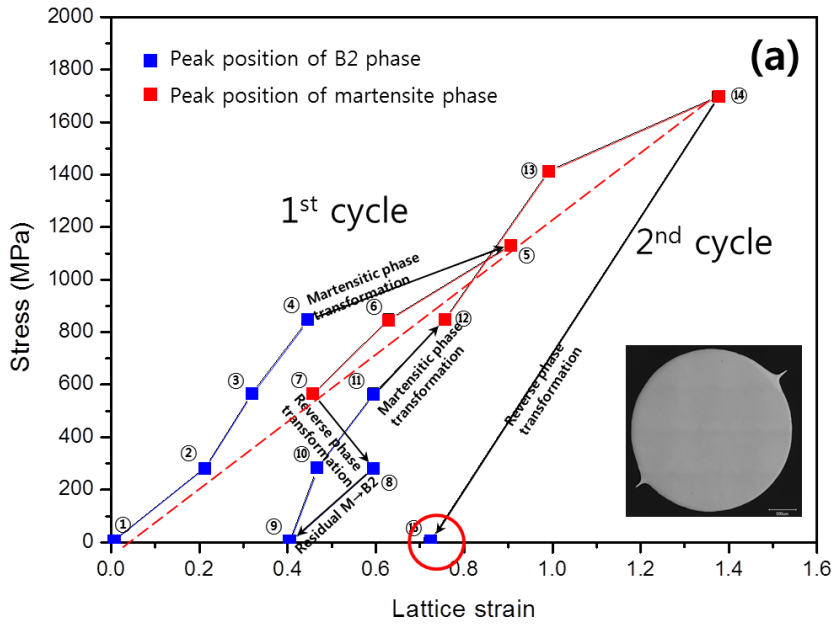
Fig. 4.13. Change of lattice strain of B2 parent phase and B19 martensite phase of Ti$_{49}$Cu$_{41}$Ni$_7$Si$_1$Sn$_2$ as-cast rod specimen during cyclic compressive loading(a). The lattice strain points were obtained by the analysis of neutron diffraction pattern measured under cyclic loading. EBSD phase map of the deformed specimen after 2cycle of compressive loading.

4.4.2. In-situ synchrotron diffraction measurement

Fig. 4.14 shows in-situ high energy x-ray diffraction spectra of as-cast $(Ti_{51}Cu_{41}Ni_7Si_1)_{98}Sn_2$ cylindrical specimen having a diameter of 3 mm under uniaxial compressive loading, which shows clearly single B2 (Pm3m) to B19 martensite (Pcmm) phase transformation from ~350 MPa to ~470 MPa. Because the bulk specimens consist of coarse grains with an average diameter of 291 ± 12 µm and have no precipitates revealed by transmission electron microscopy (not shown) and high-energy X-ray diffraction, it was assumed that the effect of microstructure on M_s is negligible.

4.4.3. In-situ high temperature compression test

Fig. 4.15 shows stress-strain curves of $(Ti_{51}Cu_{41}Ni_7Si_1)Sn_3$ as-cast rod specimens under in-situ compression test at room temperature and elevated temperature. As the operating temperature increases, the difference between the operating temperature and the M_s gradually increases, and hence a larger stress change is required for the MT. The tendency of increasing critical stress for MT shows this phenomenon well, and when plotted against temperature, linear correlation can be confirmed by clasius clapeyron relation. The slope is multiplied by the transformation temperature and the enthalpy change value, respectively, to calculate the volume change that occurs during MT. The volume change obtained from this was -0.59%, indicating a somewhat small negative value. Fig. In 4.16, it was confirmed by dilatometry that the volume was reduced by -0.14% at the transition point where the austenite to martensite phase transition occurred in the high temperature stable phase.
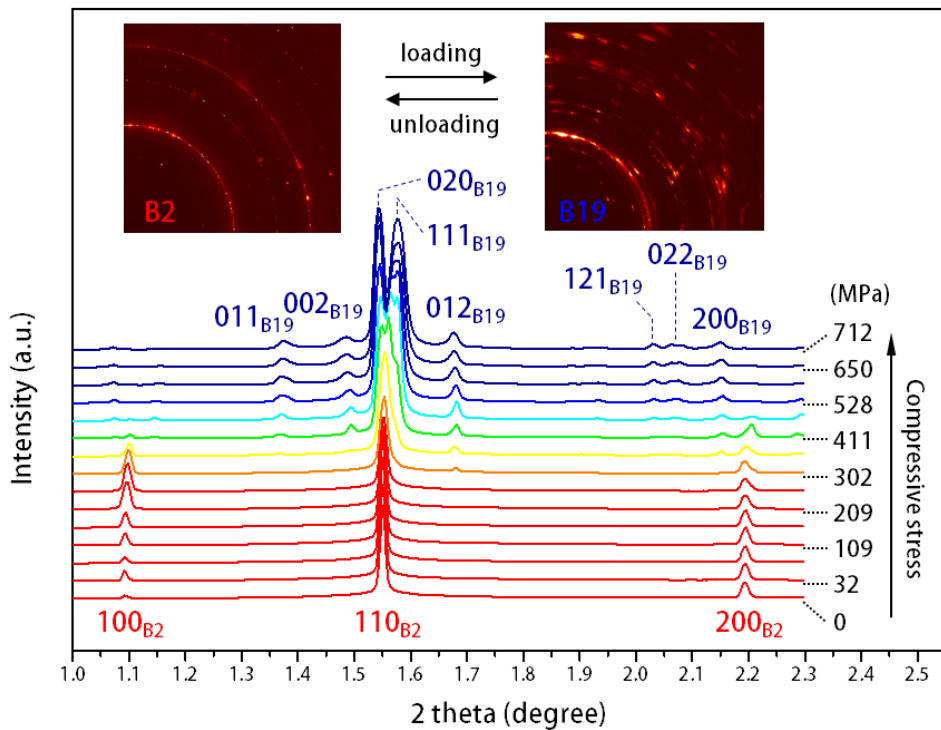
Fig. 4.14. In-situ high energy x-ray diffraction spectra of as-cast $(Ti_{51}Cu_{41}Ni_7Si_1)_{98}Sn_2$ cylindrical specimen having a diameter of 3 mm under uniaxial compressive loading.
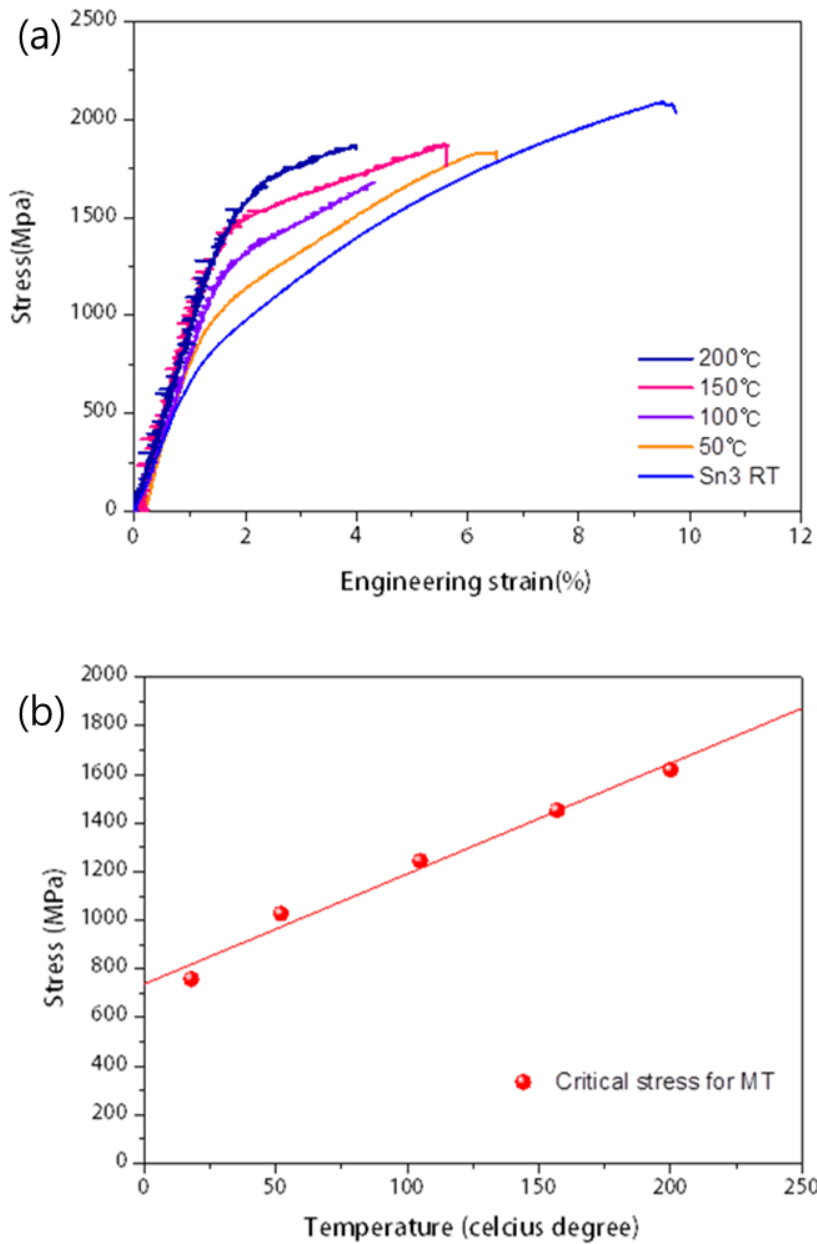
Fig. 4.15. Stress-strain curves of $(Ti_{51}Cu_{41}Ni_7Si_1)Sn_3$ as-cast rod specimens under in-situ compression test at room temperature and elevated temperature(a). Plot of critical stress for stress-induced martensitic phase transformation at different temperature(b).
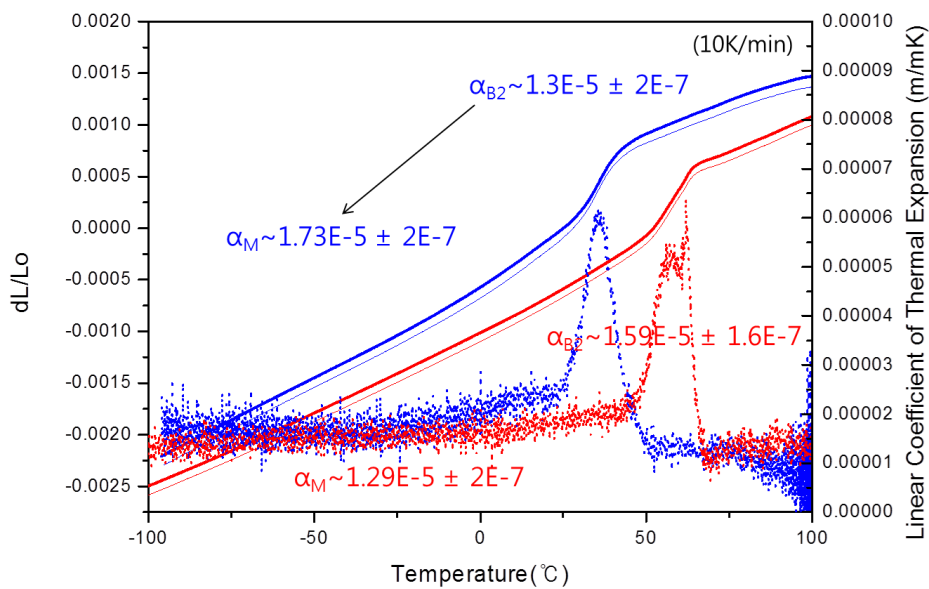
Fig. 4.16. Dilatometric curves of $(Ti_{51}Cu_{41}Ni_7Si_1)Sn_3$ as-cast rod specimen.Blue curves are obtained during cooling process, and the red curves are obtained during heating. Solid lines represent length change relative to the initial length of specimen. Dotted lines show linear coefficient of thermal expansion obtained by derivation of the dL/L_0 lines.

Chapter 5.

Application of TiCu-based super-elastic alloys

5.1. Elastocaloric effect

5.1.1. Elastocaloric effect in shape memory alloys

Elastocaloric applications require superelastic shape memory materials which show high fatigue resistance, adjustable transformation temperatures, short heat transfer times, and large elastocaloric effect sizes. Ti-rich TiNiCu films are known for their high functional and structural stability, accompanied by a small hysteresis caused by the good crystallographic compatibility of austenite and martensite phase [6, 9, 56-60]. Still, for the application of TiNiCu as an elastocaloric cooling agent, transformation temperature and further high stability of functional fatigue is necessary. Another requirement is a small superelastic hysteresis since it is directly proportional to the dissipated work [61]. These quantities determine the efficiency of the material expressed by the coefficient of performance (COP) which relates the transferred heat of a cooling cycle Q to the performed work W, COP = Q/W. Aim of this work is to investigate not only the intrinsic material COP, but also the ideal COP, Carnot COP. Major sources of losses in an actual device like parasitic heat flow are not taken into account. Several research groups are working on prototypes based on bulk materials to evaluate not only the intrinsic material COP, but also the whole cooling process efficiencies.
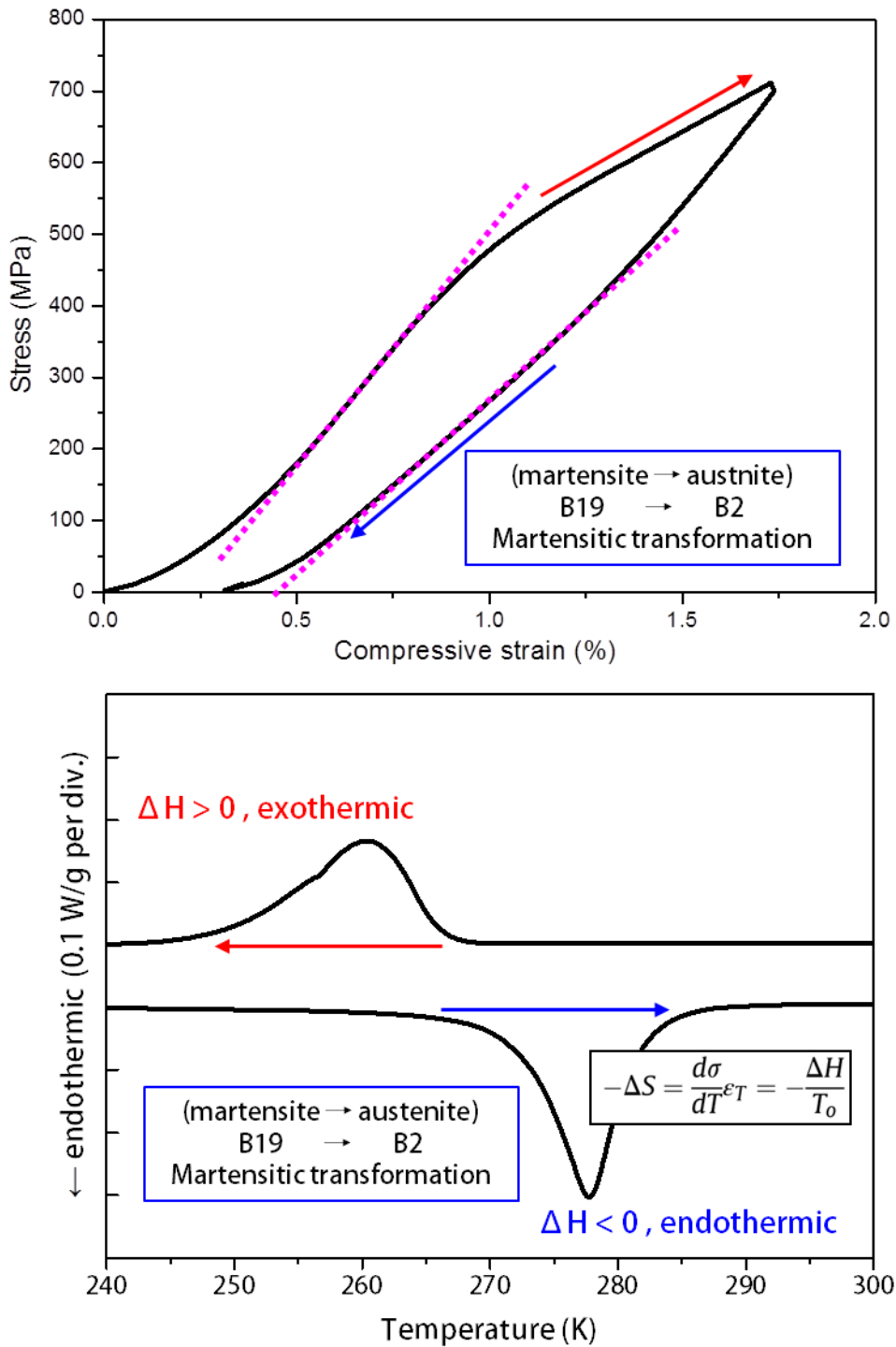
Fig. 5.1. Illustration of quasi-adiabatic stress-strain curve and heat flow curve of super-elastic alloys for elasto-caloric material.

5.1.2. Effect of Cu content on elasto-caloric effect

The elasto-caloric effect refers to the change in enthalpy as the applied external stress field changes. In most cases, the enthalpy changes originate from the martensitic phase transformation in shape memory alloys. Cooling system to make use of elasto-caloric effect has been recognized as a promising alternative to the vapor compression cooling system, owing to the high COP. In the present study, we developed novel Ti-based multicomponent alloys and tailored the temperature change and mechanical hysteresis for improving COP. It is expected the methodology for modulating mechanical hysteresis can be used as a useful guideline for optimizing COP through tailoring the composition of the shape memory alloy in various alloy systems in the future. The martensitic transformation from austenite to martensite phase causing a temperature increase occurs when the applied stress is beyond the critical transformation stress. Upon unloading, the reverse martensitic phase transformation occurs, resulting in temperature decrease. For realizing high efficiency (COP) in elasto-caloric effect, low mechanical hysteresis and large amount of latent heat of martensitic phase transformation should be obtained. Although the highest enthalpy change and temperature change of 17K were reported in NiTi SMAs, COP of the alloy system is not good as other SMA systems. The possibility of being used as elasto-caloric material has been reported in other various shape memory alloy systems of Co-Ni-Al(~3 K), Cu-Al-Zn(~6 K), Cu-Al-Ni(~14 K) and Ni-Fe-Ga-Co(~10 K). Among them, Cu-Al-Zn alloy system has been demonstrated to have excellent COP as a result of its significantly low hysteresis, but the temperature change is not promising for real cooling system. In the present study, we developed novel Ti-based super-elastic

alloys for elasto-caloric material. Through tailoring of the nominal alloy composition, the temperature change during martensitic transformation and the input energy during cyclic loading were controlled and the high efficient caloric material was designed.

For designing high efficient elasto-caloric material, it is important to modulate its mechanical hysteresis during cyclic loading and latent heat during martensitic phase transformation. We developed novel TiCu-rich multi-component B2 alloys that have low transformation hysteresis and internal friction by minor addition of Si. Fig. 5.2 shows the stress strain curves of cyclic compression test results of TiCuNiSi alloy system. Mechanical hysteresis during cyclic loading is related to the degree of difference between crystal structure of austenite phase, the high temperature stable phase, and martensite phase, the low temperature stable phase. Increasing the mechanical and thermal hysteresis of the martensitic transformation increases the dissipated mechanical energy and reduces the COP during cooling cycle. The developed alloys have extremely high Cu content which are favorable for low hysteresis. The high Cu content could be realized by addition of small amount of Si that stabilizes the B2 phase and prohibits the precipitation of other intermetallic compounds.
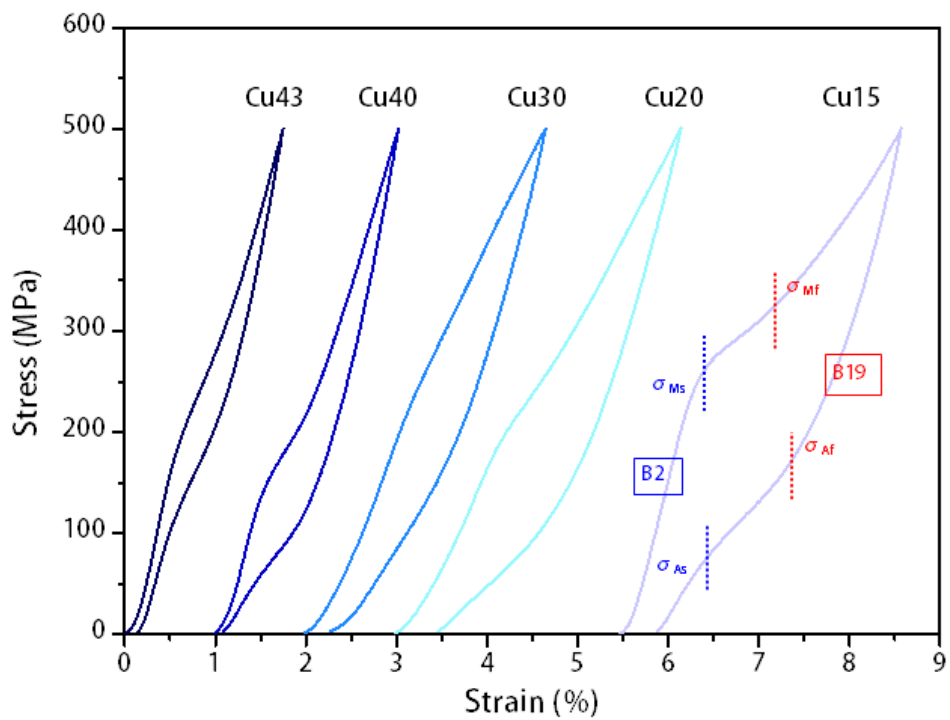
Fig. 5.2. Plots of stress-strain curves of cyclic compression test results of $(Ti_{50}Cu_XNi_{50-X})Si_1Sn_1$ alloy system. Samples of Cu-rich composition show low mechanical hysteresis.
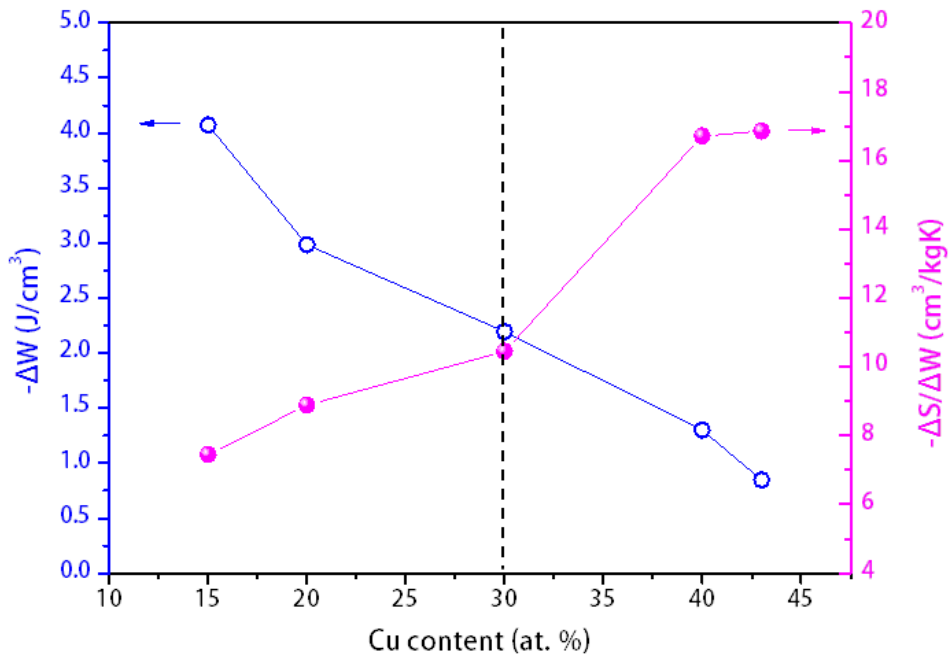
Fig. 5.3. Plots of the area of stress strain curve of cyclic compression test results, and the ratio of entropy change during martensitic transformation to the area of stress strain curve of cyclic compression test results

5.1.3. Measurement of elasto-caloric effect in TiCuNiSiSn superelastic alloys

The efficiency (coefficient of performance, COP) of elasto-caloric effect of material is determined by the ratio of the amount of latent heat generated during the phase transformation and the amount of mechanical energy consumed in the phase transformation. The latent heat can be directly measured by infrared camera, and the consumed mechanical energy can be obtained from compressive stress-strain curve [62]. Fig. 5.4 shows the infrared image obtained during in-situ compression test. The temperature increase of the developed super-elastic alloy sample induced by the stress-induced martensitic phase transformation during compressive loading is shown in the center of Fig. 5.4. For the application of elastacaloric cooling materials, we investigated the temperature change over the surface of the sample that is considered as a cooling power [63]. The maximum and minimum temperatures were measured over an area of surface. The strain rate effect on temperature change is investigated in the range between 0.001/s and 0.2/s. Fig. 5.5 shows maximum temperature during loading and minimum temperature during unloading at different strain rate. In the case of loading, the temperature does not change first and the sample is elastically deformed until the critical stress for the martensitic transformation is reached in the austenite state. The temperature increases in proportion to the strain rate and reaches its maximum at the end of the martensitic transformation. The maximum temperature change is dependent on the strain rate, because of the heat transfer by conduction into the air and anvils.For the highest strain rate of 0.2/s, we observe a maximum temperature change of 7.8 K. The temperature equilibrates with the ambient temperature while maintaining the

sample at an iso-stress condition for 30 seconds. The thermal equilibrium was well approximated as a function of exponential decay. When unloading, the reverse martensitic transformation starts immediately. The decrease in temperature is also proportional to the strain rate. In addition, the lowest temperature reached until the end of deformation is dependent not only on heat transfer but also on strain rate. The maximum decrease in temperature during unloading observed at a strain rate of 0.2/s is -7.8 K.
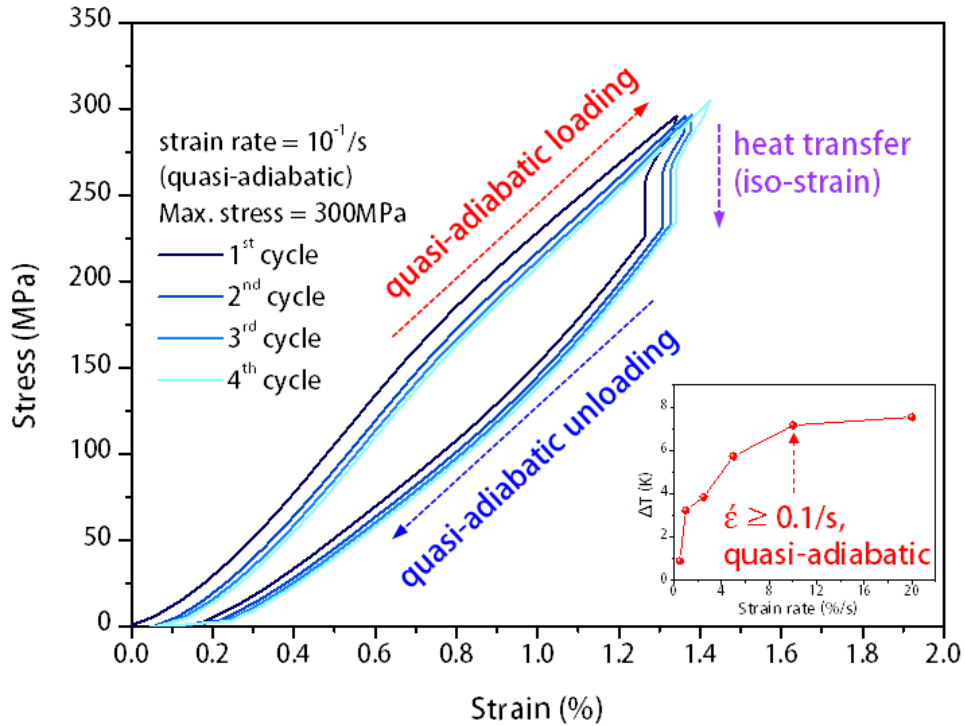
Fig. 5.4. Stress strain curves of cyclic compression test results of $(Ti_{50}Cu_{40}Ni_{10})Si_1Sn_1$ specimen by quasi-adiabatic loading and unloading. The inset shows maximum temperature change of the sample during unloading according to the strain rate. At the strain rate over 0.1%/s, the amount of maximum change of temperature is saturated, in which the sample is considered to be under quasi-adiabatic condition.
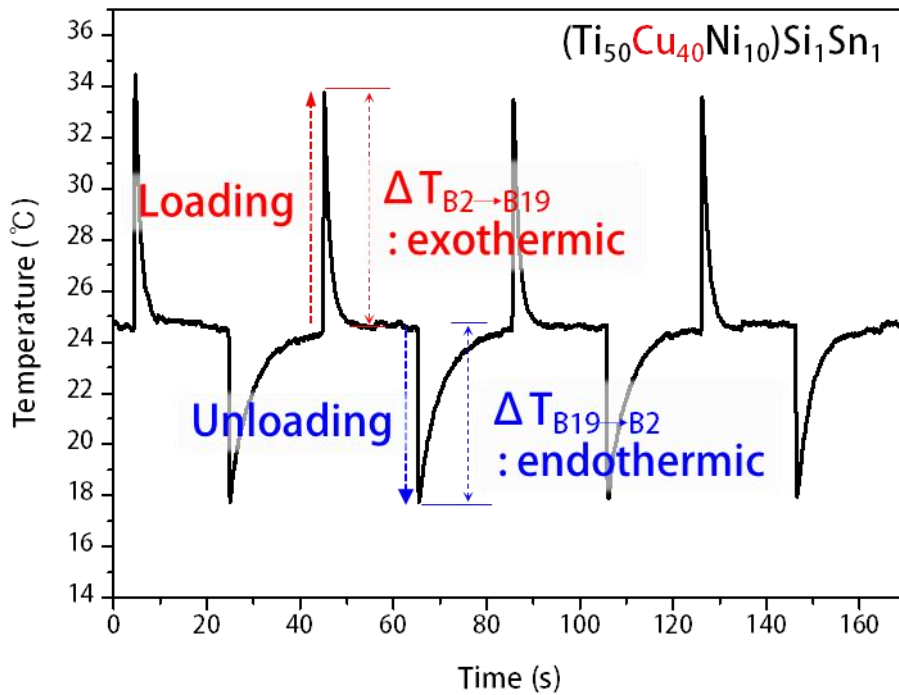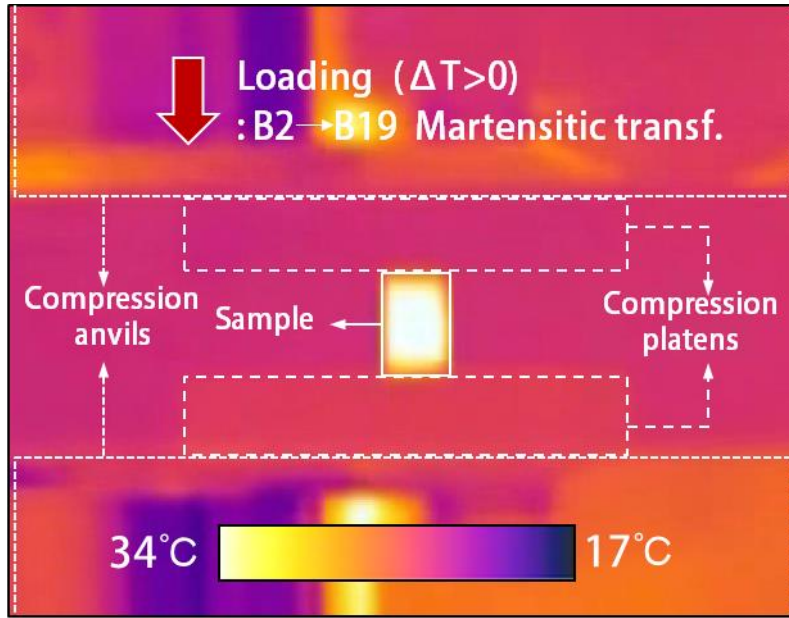
Fig. 5.5. The Infrared image during quasi-adiabatic loading, the exothermic reaction of forward martensitic transformation, and the temperature vs. time curve during cyclic loading.

5.1.4. Mechanical & Functional fatigue in TiCu-based super-elastic alloys

Since the elastocaloric effect in SMAs is induced by the chemical enthalpy difference that is released or absorbed during transformation, elastocaloric fatigue is expected to correlate closely with the martensite transformation characteristics and their fatigue properties [64-67]. For instance, an increase in residual strain during superelastic cycling due to the introduction and multiplication of defects results in an increased fraction of remaining, nontransforming martensite. When the fraction of transforming material thus decreases for higher cycle numbers, the elastocaloric effect size must decrease likewise. In order to investigate the elastocaloric effect and its fatigue behavior, the temperature changes in freestanding TiCuNiSiSn alloys during stress induced forward and reverse MT were monitored in this study by means of IR thermography. These temperature changes were measured during 10^5 superelastic cycles and are related to their corresponding stress-strain curves.

The effects of Cu addition on the properties and the microstructure of TiNi based shape memory alloys are well known [68, 69], but in this study, the content of Cu increased extremely, so that the cyclic mechanical and functional stability during superelastic loading is further improved. Fig. 5.6 shows the mechanical energy dissipation of the $(Ti_{50}Cu_{40}Ni_{10})Si_1Sn_1$ alloy over 10^5 superelastic cycles through a stress-strain curve and shows the amount of exothermic heat through the temperature-time curve. It was confirmed that even when the superelasatic cycles of 10^5 was proceed, there was almost no change of the curve shape, and thus it had excellent fatigue resistance.

Fig. 5.7 shows the temperature change and relative COP value per strain of TiCuNiSiSn alloy composition compared with SMAs developed and studied as other elastocaloric materials [7, 70-87]. The TiCuNiSiSn alloy developed through this study is in as-cast state without heat treatment. It exhibits very high efficiency and excellent fatigue resistivity even though it has polycrystalline which does not have special texture. It is considered to be the most promising elastocaloric SMA reported to date do. Also, as the cycle is repeated, the relative COP value is further increased, which is considered to be a material suitable for energy efficiency in long - term use.
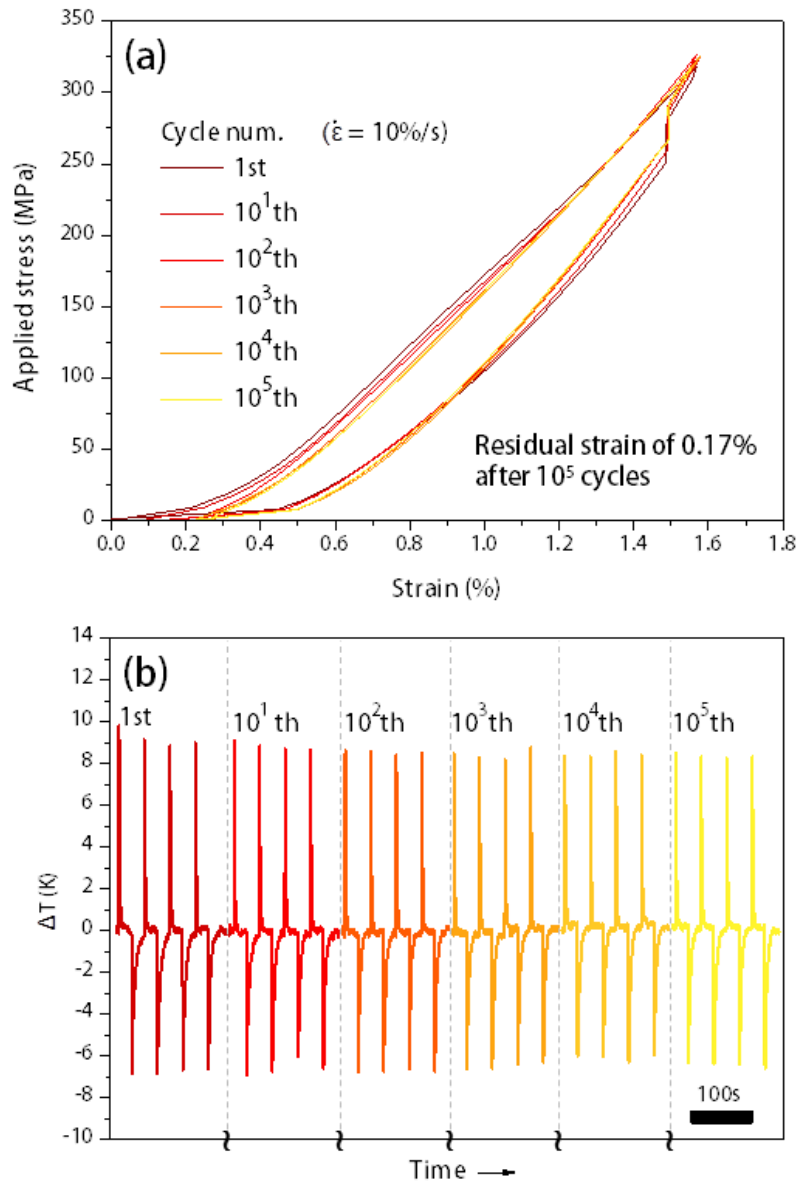
Fig. 5.6. Illustrations of adiabatic stress-strain curves(a) and the temperature vs. time curves(b) during fatigue test up to 10^5 cycles.
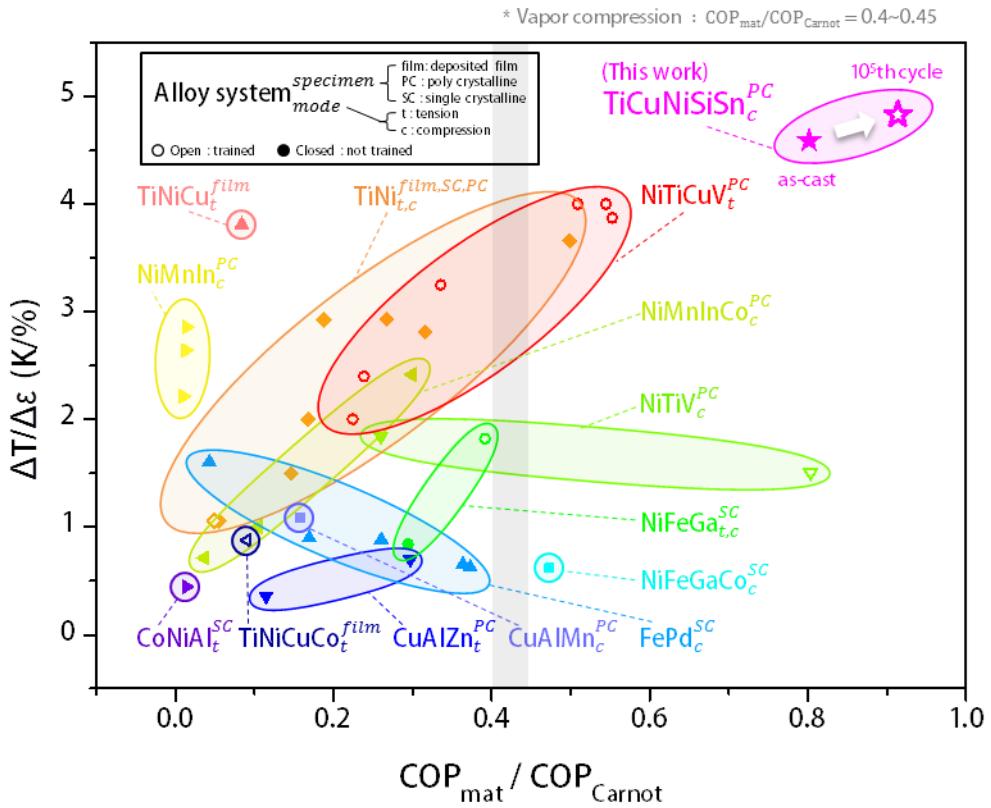
Fig. 5.7. ΔT/Δε vs. COPmat / COP$_{Carnot}$ map for elastocaloric SMAs.

5.2. Secondary phase in bulk metallic glass matrix composite

5.2.1. Glass forming ability of TiCu-based alloy system

In this study, we have designed a new amorphous alloy system based on the ternary systems of Ti, Cu, and Ni, which are the main three elements except for Be in the conventional alloy system with excellent amorphous formability (GFA). In general, in order to have a high amorphous forming ability of an alloy of a specific composition, high stability of a liquid phase should be ensured. In order to search for a composition having the highest stability of a liquid phase in a TiCuNi ternary alloy system, Thermo-Calc, which is one of typical programs of CALPHAD, To calculate the three-state state diagram (see Fig 5.8.).

It is possible to calculate the ternary state diagram in the temperature range not previously reported through the Thermo-Clac. From this, it is confirmed that the composition of the tertiary process (ternary eutectic) in which the liquid phase is the most stable in the Ti-rich composition has amorphous formation ability of 1 mm or more . Based on the trivalent state diagram, small amounts of Zr, Si, Sn and Nb (1 ~ 4 at%), which are known to increase the amorphous formability of the Ti-based alloy system, are added to the Ti-Cu-Ni ternary alloy. We have developed amorphous alloy system and investigated the change of amorphous formability according to the kinds of additive elements. We obtained excellent GFA over 4mm, which are larger than GFA reported in TiCuNi alloy system [88]. The size and shape of the specimen were controlled by controlling the cooling rate by

controlling the GFA by varying the kinds and amounts of the four added elements Zr, Si, Sn, and Nb. Amorphous matrix composites with various distributions were prepared. Also, it was confirmed by X-ray diffractometry that the second phase (Ti-Cu (Ni)) precipitated in the amorphous matrix regardless of composition and cooling rate.
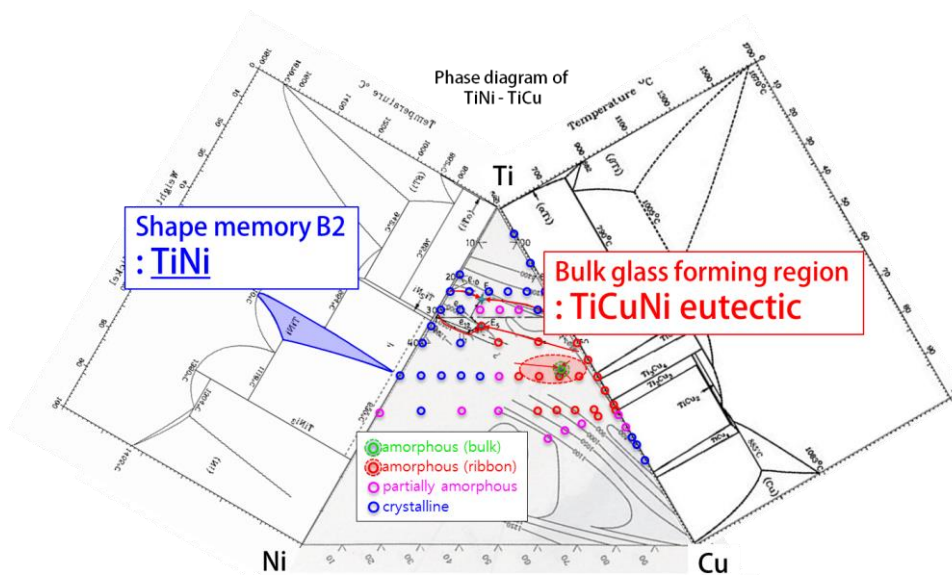
Fig. 5.8. Glass forming ability(GFA) map for Ti-Ni-Cu ternary alloy system is illustrated with the binary phase diagram of Ti-Ni and Ti-Cu, and liquidus projection of Ti-Ni-Cu alloy system. Wide range of glass forming alloy composition is around the ternary eutectic point.
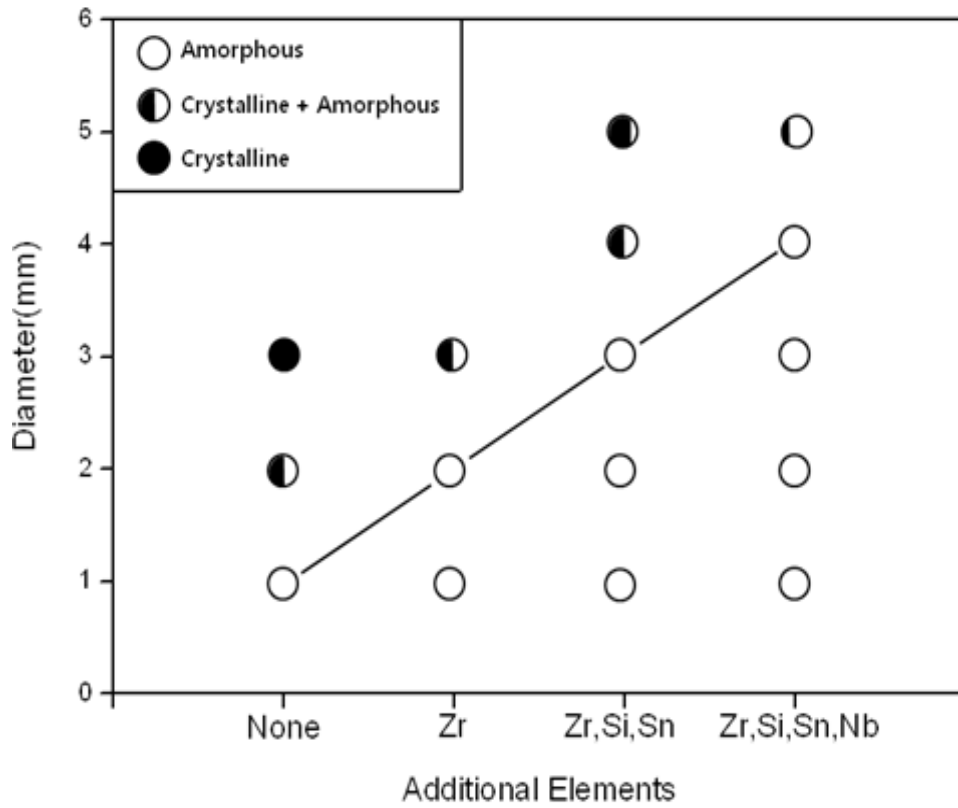
Fig. 5.9. Change of amorphous formability(GFA) of Ti-Cu-Ni alloy system with additive elements.

5.2.2. Development of TiCu-based bulk metallic glass composites

All of the bulk specimens of this study were produced by suction casting into a rod with a length of 50 mm. The larger the diameter of the rod in the horizontal direction, the slower the heat transfer rate and thus the slower the cooling rate. In particular, the closer to the center of the specimen, the lower the cooling rate, and the superstructure is likely to precipitate from the center of the specimen. The TiCuNiSnSi alloy was prepared with a diameter of 3 mm. When the alloy of the same composition was formed by suction casting with a smaller diameter, a specimen with a part of the specimen solidified into an amorphous structure can do. In order to improve the amorphous formation ability, addition of Zr element at 2 at.% Can increase the fraction of amorphous phase.

In this study, amorphous matrix composites were fabricated as shown in Fig. 5.9 (a). As a result of SEM - EDS measurement of the amorphous matrix of the same specimen and the SEM - EDS of the second phase of the shape memory primer, Fig. 5.9(B) shows that the composition phase of the two phases agree with each other within the error range, (C). As shown in Fig. 5.9(C), XRD measurement showed that a single crystalline phase (B2, 110 peak) in the amorphous base was precipitated. In particular, as can be seen from the EDS results, the precipitation of the second phase in the composite is achieved through polymorphic transformation, so that the characteristics of the second phase can be controlled by the composition design of the parent alloy. Figure 5.9(c) shows the X-ray diffraction pattern of the cross-section of the composite material and the cross-section of the 3 mm diameter specimen (complete crystalline microstructure), which is a comparative group. In

the composite material, the halo peak due to the amorphous structure and the sharp peak Were observed simultaneously. Since the mechanical properties of amorphous matrix are relatively less dependent on the content of additive elements, the effect of the characteristics of the second phase on the mechanical properties of the amorphous matrix composites can be clarified by using alloys designed through this concept.

3mm cylinder of BMG composite specimens were prepared by adding Zr2 at. %. In order to further increase the fraction of amorphous phase in the Ti-Cu-Ni-Sn-Si alloy. The second phase fraction of the composite material was controlled by controlling the amount of arc plasma injected into the molten metal during suction casting. It is thought that this is because the temperature of the molten metal before casting can be adjusted according to the intensity of arc plasma. In the casting device of this study, the current can be controlled to 50, 100, 150, 200, 250, 300A respectively. Fig 5.9 shows the cross section of the specimen prepared by injecting $(Ti_{50}Cu_{40}Ni_7Sn_2Si_1)Zr_2$ alloy at currents of 50, 100, 150, and 200A. Using this method, amorphous matrix composites with various phase fractions for the same alloy composition can be produced, so that the effect of the second phase fraction control can be confirmed by controlling the superelastic characteristics of the second phase in the composite material have.
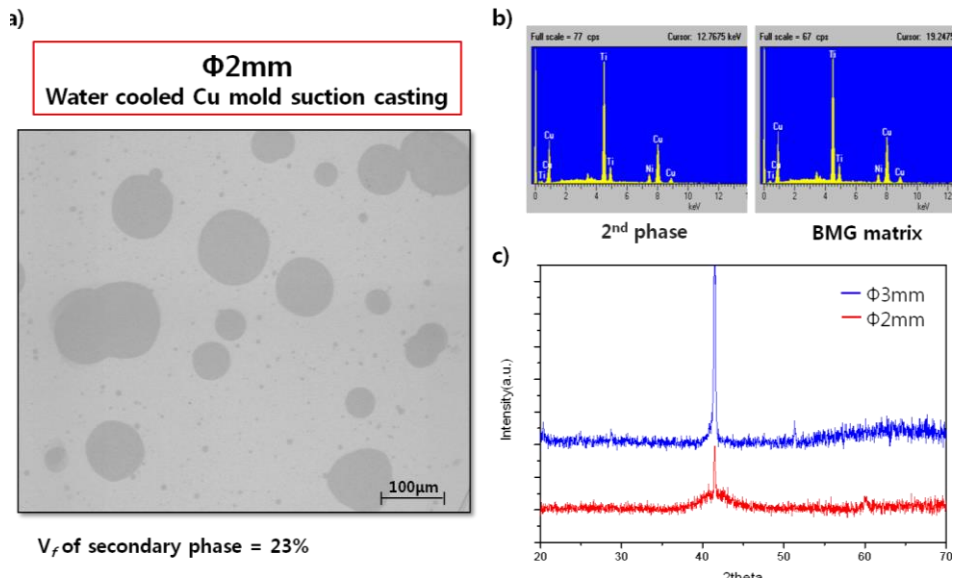
Fig. 5.10. An OM image (a), EDS result (b), and XRD patterns (b) of bulk metallic glass matrix composite specimen of $(Ti_{51}Cu_{41}Ni_7Si_1)Sn_2Zr_2$ prepared by suction casting.
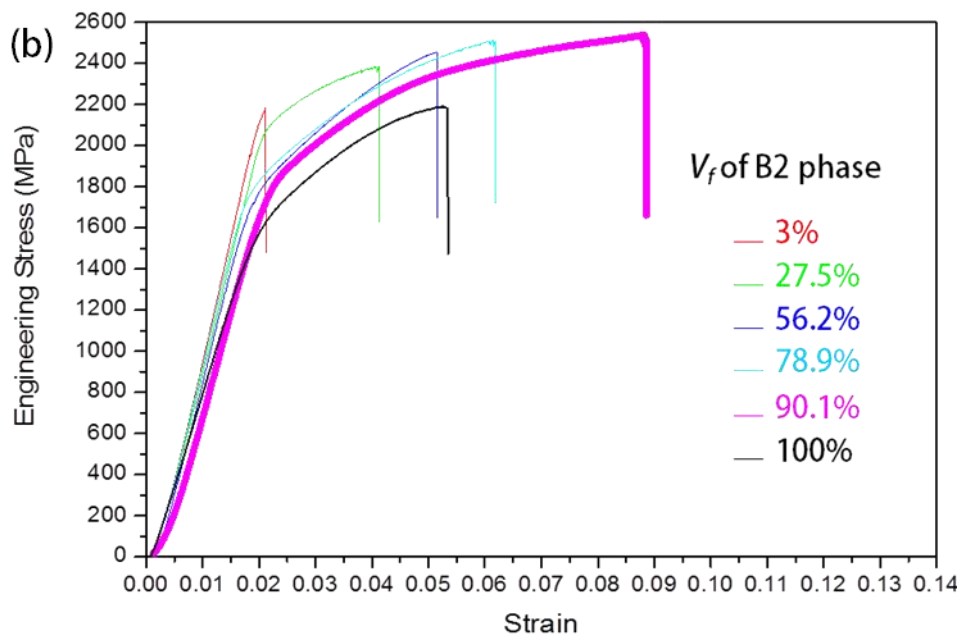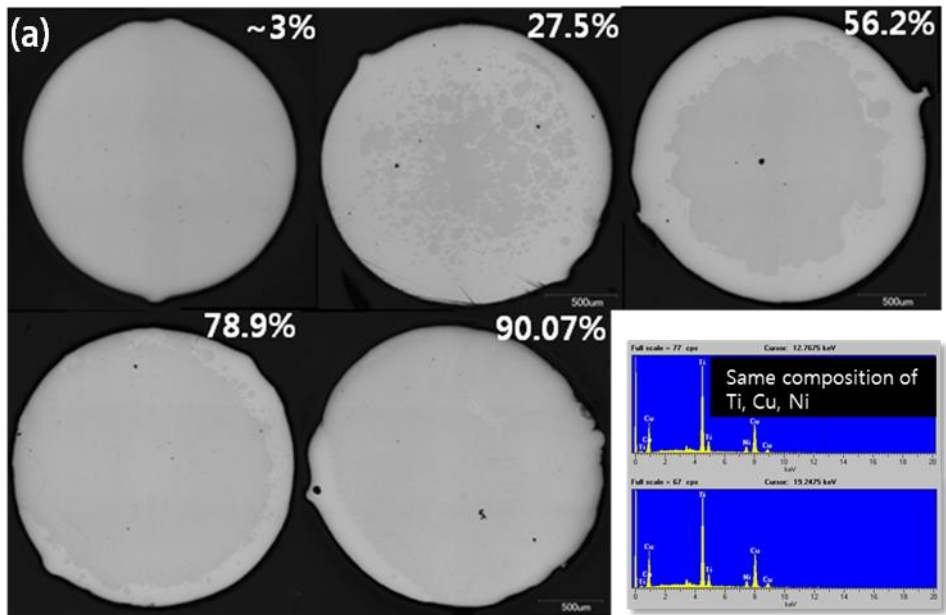
Fig. 5.11. Volume fraction of B2 secondary crystalline phase in amorphous matrix composites obtained by the modulation of electric current and casting pressure (a). The inset show the point EDS results for the glass matrix and B2 crystalline phase of samples with 56.2% of B2 phase.

5.2.3. Investigation of martensitic transformation of secondary phase in bulk metallic glass matrix composite

It is considered that the interaction between the amorphous matrix and the superelastic B2 phase is limited by the phase transformation stress. It is also necessary to analyze the deformation behavior considering the orientation of the crystal lattice with respect to the applied load direction. In consideration of these requirements, this study is intended to analyze the deformation behavior of superelastic phase 2 in amorphous matrix composites using in-situ high energy X-ray diffraction under cyclic uniaxial compressive strain. In the 11-ID-C beamline of the advanced photon source (synchrotron accelerator) of the Argonne national laboratory, the in-situ transmission diffraction pattern under uniaxial compressive strain is parallel to the longitudinal or vertical A diffraction pattern corresponding to all orientations as well as one direction (transverse) can be measured through a two-dimensional detector, and a schematic diagram thereof is shown in Fig. 5.10 In the first pressurization phase, no phase change occurred in the phase change stress 600 ~ 800MPa of the second phase, and the phase change start stress was analyzed to be about 1400MPa, which is close to the yield stress. It is confirmed that the phase transformation does not progress at a rapid rate like the crystalline specimen even after the start of the phase change but the gradual phase transformation continues until the time of the plastic deformation step after the yield point. In addition, the slope of the lattice strain change of B2 phase was almost constant before the phase transformation (before about 1400 MPa), but the slope of the lattice strain tended to increase rapidly after the phase change. This is because the strain due to load application is concentrated on the residual B2 phase as the

fraction of B19 martensite phase increases. In conclusion, it was confirmed that the phase transformation starting stress of B2 phase precipitated in the amorphous matrix greatly increased from 600 MPa to 1400 MPa, and the phase transformation process progressed gradually over a wide stress range. The interaction with the amorphous matrix increased stress - induced phase transformation initiation stress by more than 800 MPa, and the progress of phase transformation was also very low and occurred over a wide range of stresses. It can be deduced from the difference between the amorphous phase and the modulus of the second phase that the modulus of the amorphous phase is about 100 GPa and the modulus of B2 phase is about 90 GPa, which is higher than that of amorphous phase. When a deformation is applied to a composite structure of two materials having different modulus values, a stress-shielding phenomenon occurs in which deformation of a material having a low modulus is delayed due to concentration of stress on a material having a higher modulus. In addition, the second phase in the composite material is not uniformly distributed, but the second phase is agglomerated in the center portion, the second phase is surrounded by the amorphous matrix, and the second phase has different shapes. The grain size difference may also affect the deformation behavior Therefore, it is expected that the stresses in the shortage will be distributed in a very wide range, and thus the phase transformation will progress gradually over a very wide stress range. These local nonuniformities generally prevent shearband from plastic deformation of amorphous alloys from limiting propagation and growth into the main cracks leading to fracture
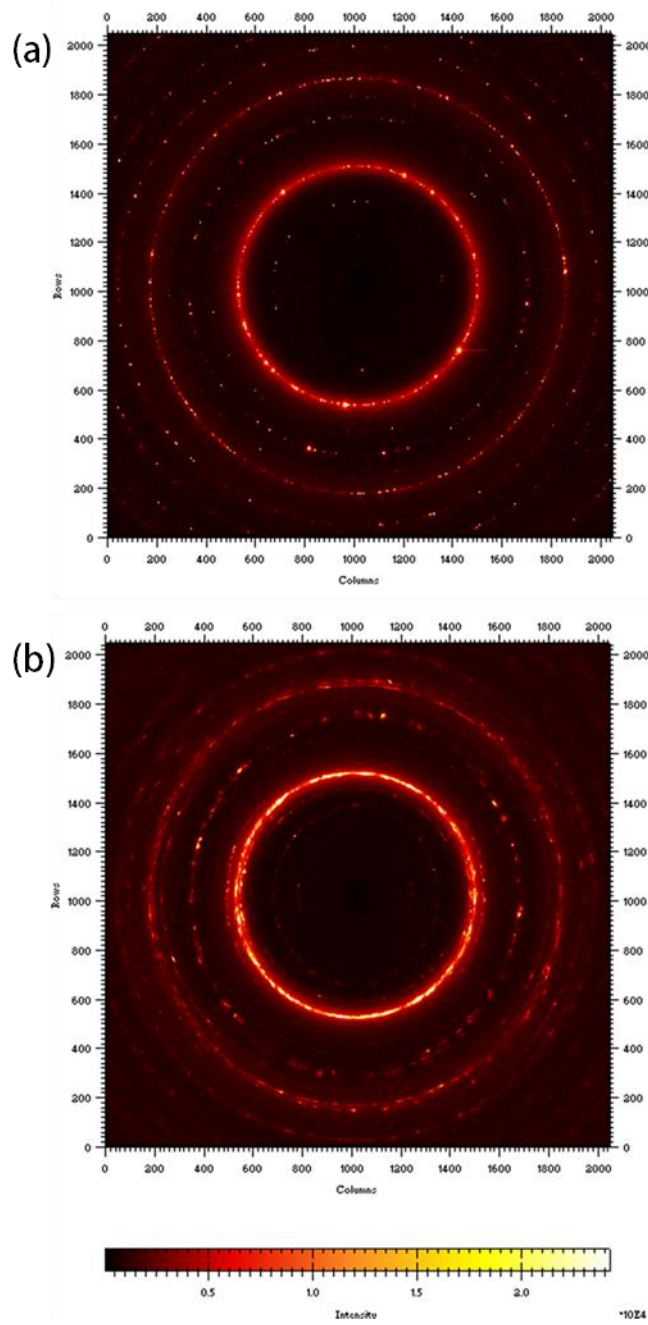
Fig. 5.12. Images of 2-D diffraction patterns obtained by in-situ HE-XRD under stress-free condition (a) and under compressive stress (b). (b) shows non-isotropic diffraction pattern representing preferential variant of martensite according to the loading direction.
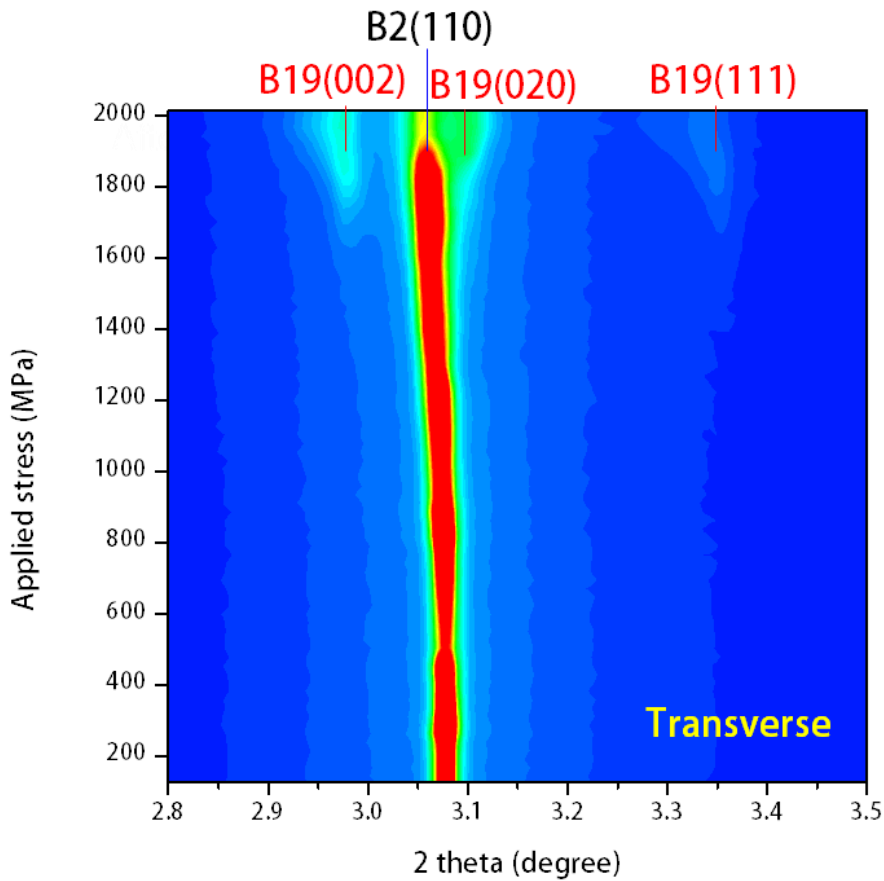
Fig. 5.13. Intensity map of the diffraction peak of in-situ measured diffraction patterns of bulk metallic glass matrix composite samples of $(Ti_{51}Cu_{41}Ni_7Si_1)Sn_2Zr_2$ under uniaxial compressive loading by high energy X-ray diffraction (APS 11-ID-C, USA). The measured HE-XRD patterns were plotted along the applied stress.
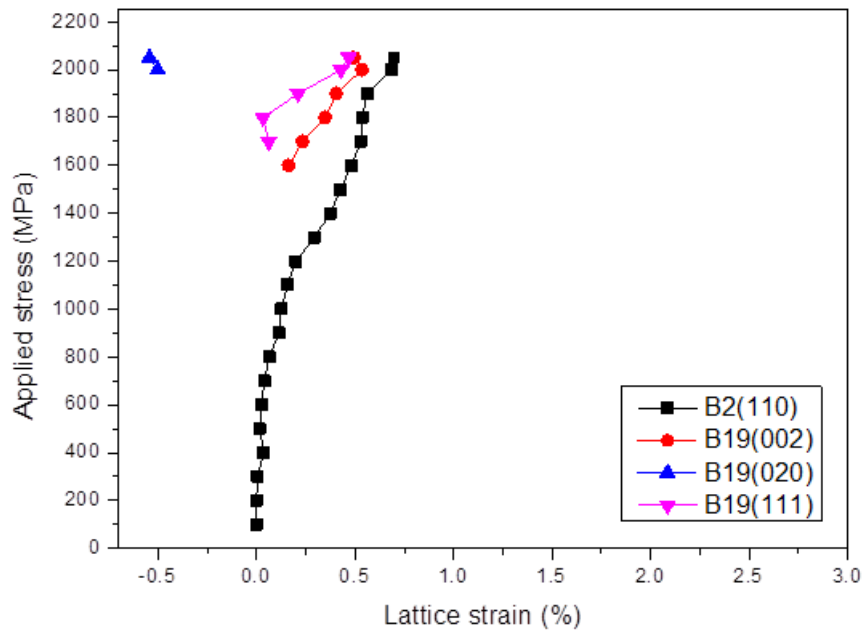
Fig. 5.14. The lattice strain changes of (110) plane of B2 parent phase and (002), (020), and (111) planes of B19 martensite phase of $(Ti_{51}Cu_{41}Ni_7Si_1)Sn_2Zr_2$ as-cast rod sample under uniaxial compressive loading, which is obtained by the analysis of HE-XRD patterns.

5.2.4. Effect of secondary phase on mechanical properties

In order to improve the amorphous forming ability in the $Ti_{51}Cu_{41}Ni_7Si_1$ four-component alloy, Zr element was added by 2 at.% And the content of Sn element was adjusted to 0, 2 at.% To control the phase change temperature (absorption energy) The specimens were prepared by 2mm / 3mm rod suction casting. In the case of the 3 mm rod specimen, phase crystallization starting temperature and absorbed energy were calculated by means of DSC analysis and uniaxial compression test with B2 crystal phase, which is shown in the fig. 5.12. In addition, the microstructure of the 2 mm rod specimen is shown in Fig. 5.12., which is fabricated in the form of an amorphous matrix composite containing the superelastic B2 phase 2 and observed under an optical microscope. According to these results, the amorphous matrix composites of the two compositions were fabricated to have absorption powers of different magnitudes (Sn0: 172J / m^3, Sn2: 138J / m^3) Phase transition temperature, or absorption energy, on the mechanical properties of amorphous matrix composites.

The uniaxial compression tests were performed on the two specimens. In order to compare the plastic deformation behavior obtained from the results, the strain due to plastic deformation was calculated using the following equation, and the plastic deformation sections after the yield point The stress-plastic strain curves obtained from the hardening zone.

$$\epsilon_p = \epsilon - \frac{\sigma - \sigma_y}{E}$$

(ϵ_p : Plastic strain, ϵ: Strain, σ: Stress, σ_y: Yield stress, E : Elastic modulus)

The plastic strain of both amorphous composites showed similar values of 6.5% and 5.8% for Sn0 and Sn2, respectively, but the slope of the stress-plastic strain curve in the work hardening zone showed a large difference. For more quantitative comparison, the absorbed energy was calculated from the curves shown in Table 3, and the absorbed energy ratio of the B2 phase of each composition and the work hardening zone of the composite was obtained. According to this, the work hardenability of the amorphous matrix composite is analyzed to be directly dependent on the absorption energy on the B2 phase introduced into the second phase. Accordingly, it was confirmed that to optimize the ultrahigh toughness characteristic, it is necessary to introduce the B2 phase having a super elastic property controlled to have the maximum absorbed energy. As shown in Fig. 5.16., ductility, work hardening, and absorbed energy of composite increased as that of B2 secondary phase increase. However, large volume fraction over 80% of secondary phase induced deterioration of yield strength.
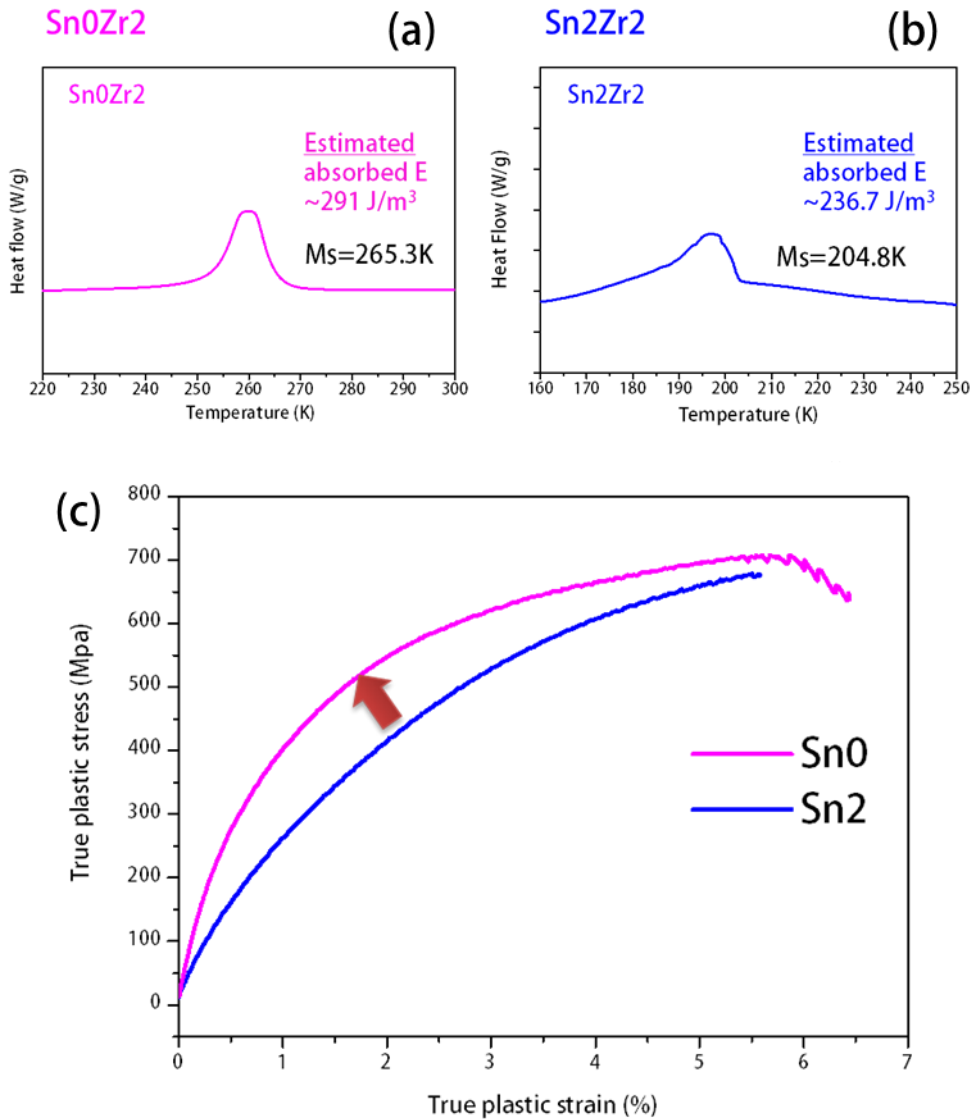
Fig. 5.15. Heat flow curves of $(Ti_{51}Cu_{41}Ni_7Si_1)Zr_2$ and $(Ti_{51}Cu_{41}Ni_7Si_1)Sn_2Zr_2$ as-cast specimens measured by differential scanning calorimetry (a, b). The B2 secondary phase of each sample has different absorption energy (Sn0: 172 J / m³, Sn2: 138 J / m³). The work hardening stress-plastic strain curves obtained from the work hardening zone of the plastic deformation section after the yield point are shown in (c).
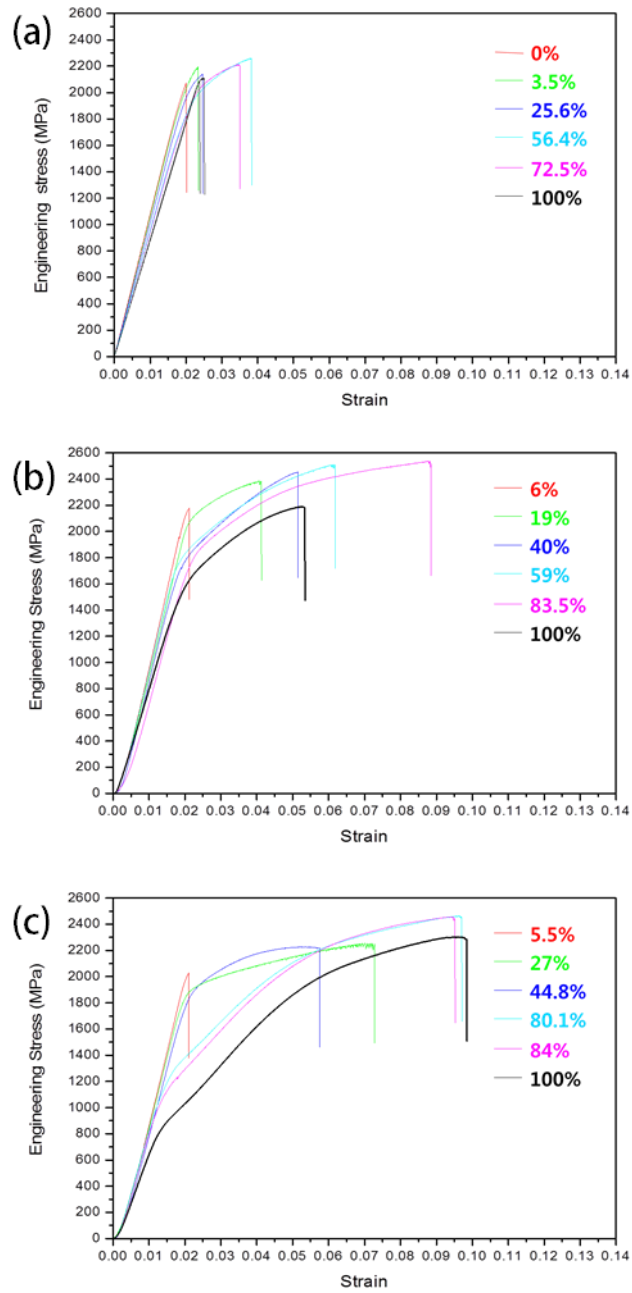
Fig. 5.16. Plots of stress-strain curves of three different compositions ($Ti_{44}Cu_{46}Ni_7Si_1Sn_2$ (a), $Ti_{46}Cu_{46}Ni_7Si_1Sn_2$ (b), $Ti_{49}Cu_{46}Ni_7Si_1Sn_2$ (c)) of bulk metallic glass matrix composites having various volume fraction of secondary phase; 100% of secondary phase indicate fully crystalline specimens.

5.2.5. Implementation of ultra-high toughness and strength of TiCuNiSiSn bulk metallic glass matrix alloys

According to the proposed method, the amorphous matrix composites were prepared by 2 mm suction casting in the $(Ti_{50}Cu_{40}Ni_7Si_1Sn_2)Zr_2$ composition, which was able to precipitate the B2 phase to the second phase, which exhibited superelastic properties capable of stress organic phase transformation at relatively low stress And a second phase fraction of about 56%. The stress-strain curves obtained by performing the uniaxial compression test are shown in Fig. 5.12., and the yield stress, the elongation at break, the maximum strength, and the stress increased through the work hardening of the plastic strain section are also shown. In the case of amorphous alloys of the same composition, yield strength was about 2 GPa. In the case of the composite, the yield strength was reduced by 17% compared with the amorphous alloy. However, by securing a high work hardening stress of 1.1 GPa, the maximum strength by work hardening was 2563 MPa, Respectively. In addition, it showed a high fracture elongation of 16.5%, which confirmed that ultra-high toughness characteristics were successfully implemented. In addition, the specific strength of this amorphous matrix composite material is 373 kNm / kg, which is comparable to that of Ti-6Al-4V, Al alloy (380 series) and Zr-based bulk amorphous alloy (LM1-b) .

The $(Ti_{50}Cu_{40}Ni_7Si_1Sn_2)Zr_2$ as-cast rod sample showed extraordinary work-hardening behavior and the fracture surface exhibits unique wavy boundary between transformation media (B2 crystalline 2nd phases) and amorphous matrix, which looks like a coastline due to a typical vein-like patterns of amorphous phase as well as dislocations file-up of crystalline phase (right bottom). Transformation

media (B2 crystalline 2nd phases) cause to branch minor shear bands and block propagation of major cracks, which can be observed in surface of the side of compression test sample with remarkable work hardening behavior, strength and ductility.
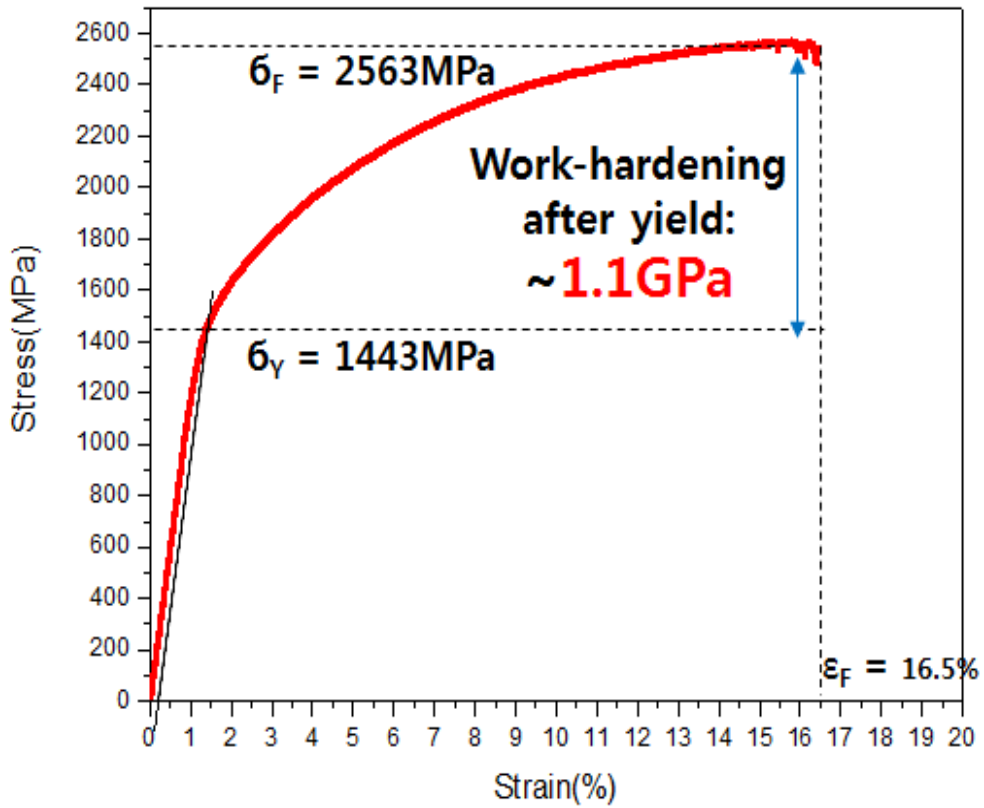
Fig. 5.17. Stress-strain curve of $(Ti_{50}Cu_{40}Ni_7Si_1Sn_2)Zr_2$ cylindrical specimen, which showed ultra-high strength and work hardening behavior over 1GPa.
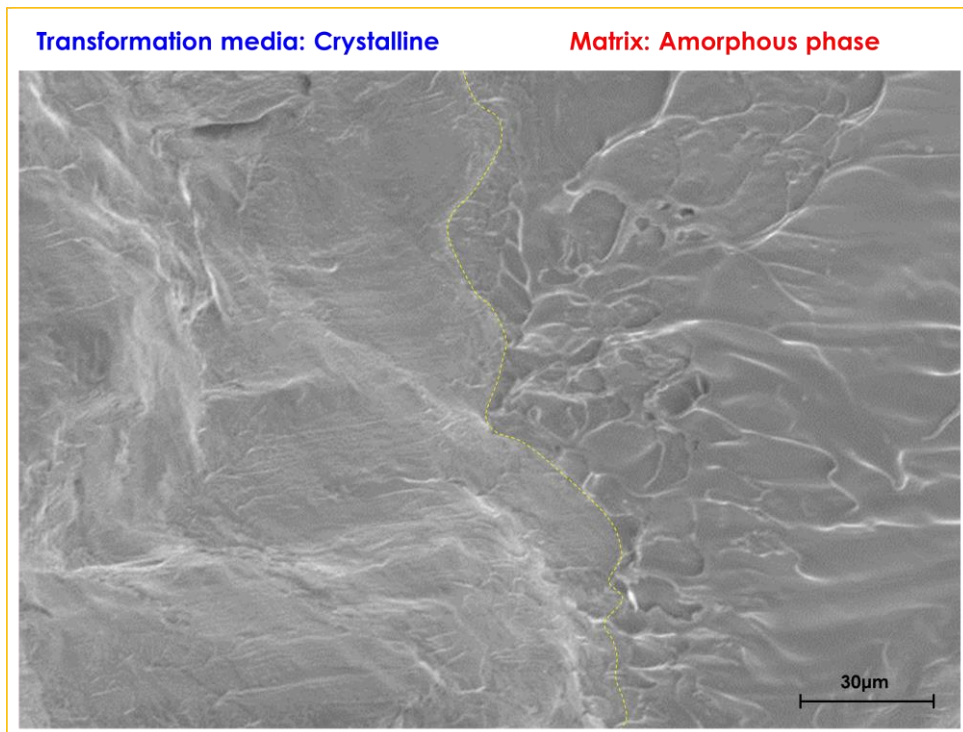
Fig. 5.18. FE-SEM image (SE) of fracture surface of $(Ti_{50}Cu_{40}Ni_7Si_1Sn_2)Zr_2$ bulk metallic glass matrix composite by stress induced martensitic transformation of polymorphically precipitated B2 secondary phases. Uniaxial compression test conducted on the as-cast 2mm rod sample.

Chapter 6.

Conclusions

Minor addition of Si inhibit the precipitation of intermetallic compounds other than the primary B2 phase in TiCuNi alloy system, and the maximum solubility of Cu was experimentally confirmed up to 43 at. %. It is considered that the effect of Si can be applied to other Ti-based SMAs to extend B2 solubility. By the analysis of XRD measurement, TiCuNiSi alloys were found to satisfy the cofactor condition even when the contents of Cu and Ni were greatly changed, resulting in very low hysteresis. In the $(Ti_{50+x}Cu_{43-x}Ni_7)Si_1$ alloy system, B2 stability is better on the Ti-rich side than on the Cu-rich side. Especially, alloys of Ti-rich composition showed very wide transformation interval with high ΔH, caused by the nano-scale compositional heterogeneity through precipitation of Ti_2Cu compound.

The additional defects caused by solute element, ASD and constitutional vacancy, can induce a severe hardening effect on SMA, and can be used to easily control MT as well as mechanical properties. The hardening effect is represented by the solute exponent t, which reflects the hybrid defect state of the solute defect, ASD and constitutional vacancy. This hardening phenomenon increases the shear modulus and shows a tendency to sharply decrease the Ms. In this respect, the point defect hardening mechanism can be utilized for the application at the ultra-cryogenic temperature. It was experimentally confirmed in a novel TiCuNiSiSn alloy system, that M_s is easily controlled from a temperature above RT to a cryogenic temperature below 14K. This study can be used as a guideline for

developing SMAs for applications such as aeronautics, space, and self-healing material. It is suggested that the solid solution hardening mechanism can be considered to modulate the transformation stress. The expressions of various parameters related to MT and mechanical properties are described including the equation of internal strength increase depending on the content of solute element Sn : $\Delta\tau_{Sn} = RX_{Sn}^{t}$. The correlations were well supported experimentally. We have attempted to realize novel properties of SMA with wide transformation temperature and stress level. As a result, TiCuNiSiSn SMAs exhibited a very wide range of ΔT from 12K to 113K, and ultra-high transformation stress of 1803 MPa.

The TiCuNiSiSn alloy system, achieved remarkably improved coefficient of performance compared to the conventional shape memory alloy system such as NiTi and CuZnAl. The efficiency of the alloy is determined by the ratio of the amount of heat generated during the phase transformation and the amount of mechanical energy consumed in the phase transformation. The increase in the Cu content in the Ti-based super-elastic alloy system reduces the amount of mechanical energy consumed as the internal friction and the martensitic phase transformation hysteresis decreases. It is expected that this alloy designing methodology can be used as a useful guideline for the optimization of characteristics through control of composition of super-elastic alloy in various systems in the future. It is considered that COP can be measured according to the adiabatic elastocaloric test condition, and the optimal experiment condition for achieving high COP is suggested. This work can contribute to design the heat exchange system with high heat exchange efficiency of appliances such as refrigerator and other products.

In the newly developed TiCuNiSiSn alloy system, bulk metallic glass matrix composites were fabricated by modulation of quenching rate. The volume fraction of the secondary phase in the bulk metallic glass matrix composite was modulated systematically by controlling the conditions of suction casting process (gas pressure, arc plasma current and inner diameter of Cu mold). Through compression test, the mechanical properties of the bulk metallic glass matrix composites investigated according to the volume fraction of the second phase. The methodology for realizing better mechanical properties of bulk metallic glass matrix composite in terms of strength, elongation, and work hardening was proposed. Our result indicates that macroscopic work hardening behavior of metallic glass matrix composite can be enhanced by casting process modulation which can be applied for various alloy systems.

Prior to this study, researchers have designed and developed alloys based on reported phase diagrams. However, if we discover the unknown SMA composition that the solid solubility of the alloying elements can be extended through alloy design methodology in this study, we can develop novel characteristics required in many applications. Although this study only studied TiCuNi-based alloys, we are able to develop other SMA systems with new characteristics by applying this concept to various conventional SMA system such as high-temperature TiNiHf and Cu-based SMA such as CuZnAl.

Bibliography

[1] A. Garcia-Junceda, C. Capdevila, F. Caballero, C.G. de Andres, Dependence of martensite start temperature on fine austenite grain size, Scripta Materialia 58(2) (2008) 134-137.

[2] H. Otsuka, H. Yamada, T. Maruyama, H. Tanahashi, S. Matsuda, M. Murakami, Effects of alloying additions on Fe-Mn-Si shape memory alloys, ISIJ international 30(8) (1990) 674-679.

[3] R.D. James, K.F. Hane, Martensitic transformations and shape-memory materials, Acta materialia 48(1) (2000) 197-222.

[4] K. Otsuka, X. Ren, Physical metallurgy of Ti–Ni-based shape memory alloys, Progress in materials science 50(5) (2005) 511-678.

[5] K. Ono, Proceedings of 3rd International Conference on Strenght of Metals and Alloys, Cambridge, England (1973).

[6] A. Chauhan, S. Patel, R. Vaish, C.R. Bowen, A review and analysis of the elasto-caloric effect for solid-state refrigeration devices: Challenges and opportunities, MRS Energy & Sustainability-A Review Journal 2 (2015).

[7] S.X. Qian, Y.L. Geng, Y. Wang, J.Z. Ling, Y.H. Hwang, R. Radermacher, I. Takeuchi, J. Cui, A review of elastocaloric cooling: Materials, cycles and, system integrations, Int J Refrig 64 (2016) 1-19.

[8] K. Otsuka, C.M. Wayman, Shape memory materials, Cambridge university press1999.

[9] F. Bruederlin, H. Ossmer, F. Wendler, S. Miyazaki, M. Kohl, SMA foil-based

elastocaloric cooling: from material behavior to device engineering, J Phys D Appl Phys 50(42) (2017) 424003.

[10] J. Friedrichs, P. Haasen, Ternary solution-hardening of copper single crystals, Philosophical Magazine 31(4) (1975) 863-869.

[11] L. JaniJm, Areviewofshapememory alloyresearch, applicationsandopportunities, materials& Design 56(4) (2014) 1078-1113.

[12] T.W. Duerig, K. Melton, D. Stöckel, Engineering aspects of shape memory alloys, Butterworth-Heinemann2013.

[13] L. An, W. Huang, Transformation characteristics of shape memory alloys in a thermal cycle, Materials Science and Engineering: A 420(1) (2006) 220-227.

[14] H. Rietveld, A profile refinement method for nuclear and magnetic structures, Journal of applied Crystallography 2(2) (1969) 65-71.

[15] N. Singh, A. Talapatra, A. Junkaew, T. Duong, S. Gibbons, S. Li, H. Thawabi, E. Olivos, R. Arróyave, Effect of ternary additions to structural properties of NiTi alloys, Computational Materials Science 112 (2016) 347-355.

[16] H.-S. Kim, W.-Y. Kim, S.-H. Lim, Microstructure and elastic modulus of Ti–Nb–Si ternary alloys for biomedical applications, Scripta materialia 54(5) (2006) 887-891.

[17] H. Kim, Y. Ikehara, J. Kim, H. Hosoda, S. Miyazaki, Martensitic transformation, shape memory effect and superelasticity of Ti–Nb binary alloys, Acta Materialia 54(9) (2006) 2419-2429.

[18] R. Labusch, A statistical theory of solid solution hardening, physica status solidi (b) 41(2) (1970) 659-669.

[19] R. Labusch, Statistical theories of solid solution hardening(Concentration of

solute atoms, interaction range between solute atoms and distortion, and interaction strength of solid solution hardening), Acta Met.,(London) 20 (1972) 917-927.

[20] Y. Lo, S. Wu, Compositional dependence of martensitic transformation sequence in Ti 50 Ni 50− x Pd x alloys with X≤ 15at%, Scripta metallurgica et materialia 27(8) (1992) 1097-1102.

[21] S. Malinov, W. Sha, Z. Guo, Application of artificial neural network for prediction of time–temperature–transformation diagrams in titanium alloys, Materials Science and Engineering: A 283(1) (2000) 1-10.

[22] L. Meng, Y. Li, X. Zhao, J. Xu, H. Xu, The mechanical properties of intermetallic Ni 50− x Ti 50 Alx alloys (x= 6, 7, 8, 9), Intermetallics 15(5) (2007) 814-818.

[23] S. Miyazaki, Y. Ohmi, K. Otsuka, Y. Suzuki, Characteristics of deformation and transformation pseudoelasticity in Ti-Ni alloys, Le Journal de Physique Colloques 43(C4) (1982) C4-255-C4-260.

[24] H. Neuhäuser, Problems in solid solution hardening, Physica Scripta 1993(T49B) (1993) 412.

[25] H. Tong, C. Wayman, Characteristic temperatures and other properties of thermoelastic martensites, Acta Metallurgica 22(7) (1974) 887-896.

[26] C. Wayman, H. Tong, On the equilibrium temperature in thermoelastic martensitic transformations, Scripta Metallurgica 11(5) (1977) 341-343.

[27] R.F. Strickland-Constable, Kinetics and Mechanism of Crystallization from the Fluid Phase and of the Condensation and Evaporation of Liquids, Academic P.1968.

[28] G. Ghosh, G. Olson, Kinetics of FCC→ BCC heterogeneous martensitic nucleation—I. The critical driving force for athermal nucleation, Acta Metallurgica et Materialia 42(10) (1994) 3361-3370.

[29] M. Morakabati, S. Kheirandish, M. Aboutalebi, A.K. Taheri, S. Abbasi, The effect of Cu addition on the hot deformation behavior of NiTi shape memory alloys, Journal of Alloys and Compounds 499(1) (2010) 57-62.

[30] S. Neelakantan, P. Rivera-Díaz-del-Castillo, S. van der Zwaag, Prediction of the martensite start temperature for β titanium alloys as a function of composition, Scripta Materialia 60(8) (2009) 611-614.

[31] S. Neelakantan, D. San Martin, P.E. Rivera-Díaz-del-Castillo, S. van der Zwaag, Plasticity induced transformation in a metastable β Ti-1023 alloy by controlled heat treatments, Materials Science and Technology 25(11) (2009) 1351-1358.

[32] R. Smialek, T. Mitchell, Interstitial solution hardening in tantalum single crystals, Philosophical Magazine 22(180) (1970) 1105-1127.

[33] A.B. Greninger, Transactions of American Society for Metals 30 (1942) 1.

[34] G. Olson, M. Cohen, A general mechanism of martensitic nucleation: Part I. General concepts and the FCC→ HCP transformation, Metallurgical Transactions A 7(12) (1976) 1897-1904.

[35] G. Ghosh, V. Raghavan, The kinetics of isothermal martensitic transformation in an Fe-23.2 wt.% Ni-2.8 wt.% Mn alloy, Materials Science and Engineering 80(1) (1986) 65-74.

[36] R.L. Fleischer, Solid-solution hardening, The strengthening of metals 93 (1964).

[37] H. Srikanth, J. Wiggins, H. Rees, Radio-frequency impedance measurements using a tunnel-diode oscillator technique, Review of scientific instruments 70(7) (1999) 3097-3101.

[38] G. Olson, M. Cohen, A general mechanism of martensitic nucleation: Part II. FCC→ BCC and other martensitic transformations, Metallurgical transactions A 7(12) (1976) 1905-1914.

[39] J. Hafner, Materials simulations using VASP—a quantum perspective to materials science, Computer physics communications 177(1) (2007) 6-13.

[40] P.E. Blöchl, Projector augmented-wave method, Physical review B 50(24) (1994) 17953.

[41] G. Kresse, D. Joubert, From ultrasoft pseudopotentials to the projector augmented-wave method, Physical Review B 59(3) (1999) 1758.

[42] K. Burke, J.P. Perdew, M. Ernzerhof, Why semilocal functionals work: Accuracy of the on-top pair density and importance of system averaging, The Journal of chemical physics 109(10) (1998) 3760-3771.

[43] M. Methfessel, A. Paxton, High-precision sampling for Brillouin-zone integration in metals, Physical Review B 40(6) (1989) 3616.

[44] D. Shin, R. Arróyave, Z.-K. Liu, A. Van de Walle, Thermodynamic properties of binary hcp solution phases from special quasirandom structures, Physical Review B 74(2) (2006) 024204.

[45] L. Pike, I. Anderson, C. Liu, Y. Chang, Site occupancies, point defect concentrations, and solid solution hardening in B2 (Ni, Fe) Al, Acta materialia 50(15) (2002) 3859-3879.

[46] T. Haraguchi, M. Kogachi, Point defect behavior in B2-type intermetallic

compounds, Materials Science and Engineering: A 329 (2002) 402-407.

[47] V. Recarte, R. Pérez-Sáez, J. San Juan, E. Bocanegra, M. Nó, Influence of Al and Ni concentration on the martensitic transformation in Cu-Al-Ni shape-memory alloys, Metallurgical and Materials Transactions A 33(8) (2002) 2581-2591.

[48] X. Ren, N. Miura, J. Zhang, K. Otsuka, K. Tanaka, M. Koiwa, T. Suzuki, Y.I. Chumlyakov, M. Asai, A comparative study of elastic constants of Ti–Ni-based alloys prior to martensitic transformation, Materials Science and Engineering: A 312(1) (2001) 196-206.

[49] T. Saburi, Ti-Ni shape memory alloys, Shape memory materials (1998) 49-97.

[50] K. Otsuka, C. Wayman, Mechanism of shape memory effect and superelasticity, Shape memory materials (1998) 27-49.

[51] F.B. Pickering, Physical metallurgy and the design of steels, Applied Science Publishers1978.

[52] M. Zarinejad, Y. Liu, Dependence of Transformation Temperatures of NiTi-based Shape-Memory Alloys on the Number and Concentration of Valence Electrons, Advanced Functional Materials 18(18) (2008) 2789-2794.

[53] T. Sourmail, C. Garcia-Mateo, Critical assessment of models for predicting the M s temperature of steels, Computational materials science 34(4) (2005) 323-334.

[54] T. Sourmail, C. Garcia-Mateo, A model for predicting the M s temperatures of steels, Computational Materials Science 34(2) (2005) 213-218.

[55] R. Fleischer, Substitutional solution hardening, Acta metallurgica 11(3) (1963)

203-209.

[56] C. Bechtold, C. Chluba, R.L. De Miranda, E. Quandt, High cyclic stability of the elastocaloric effect in sputtered TiNiCu shape memory films, Applied Physics Letters 101(9) (2012) 091903.

[57] E. Bonnot, R. Romero, L. Manosa, E. Vives, A. Planes, Elastocaloric effect associated with the martensitic transition in shape-memory alloys, Phys Rev Lett 100(12) (2008) 125901.

[58] C. Chluba, H. Ossmer, C. Zamponi, M. Kohl, E. Quandt, Ultra-Low Fatigue Quaternary TiNi-Based Films for Elastocaloric Cooling, Shape Memory and Superelasticity 2(1) (2016) 95-103.

[59] J. Cui, Y.M. Wu, J. Muehlbauer, Y.H. Hwang, R. Radermacher, S. Fackler, M. Wuttig, I. Takeuchi, Demonstration of high efficiency elastocaloric cooling with large Delta T using NiTi wires, Applied Physics Letters 101(7) (2012) 073904.

[60] K. Engelbrecht, J. Tusek, S. Sanna, D. Eriksen, O.V. Mishin, C.R.H. Bahl, N. Pryds, Effects of surface finish and mechanical training on Ni-Ti sheets for elastocaloric cooling, Apl Materials 4(6) (2016) 064110.

[61] Y. Huang, Q. Hu, N. Bruno, J.-H. Chen, I. Karaman, J.H. Ross, J. Li, Giant elastocaloric effect in directionally solidified Ni–Mn–In magnetic shape memory alloy, Scripta Materialia 105 (2015) 42-45.

[62] Y. Wu, E. Ertekin, H. Sehitoglu, Elastocaloric cooling capacity of shape memory alloys–Role of deformation temperatures, mechanical cycling, stress hysteresis and inhomogeneity of transformation, Acta Materialia   (2017).

[63] F. Xiao, T. Fukuda, T. Kakeshita, Significant elastocaloric effect in a Fe-31.2

Pd (at.%) single crystal, Applied Physics Letters 102(16) (2013) 161914.

[64] F. Xiao, T. Fukuda, T. Kakeshita, X. Jin, Elastocaloric effect by a weak first-order transformation associated with lattice softening in an Fe-31.2 Pd (at.%) alloy, Acta Materialia 87 (2015) 8-14.

[65] F. Xiao, M.J. Jin, J. Liu, X.J. Jin, Elastocaloric effect in Ni50Fe19Ga27Co4 single crystals, Acta Materialia 96(Supplement C) (2015) 292-300.

[66] F. Xiao, X. Liang, X.J. Jin, Z.H. Nie, T. Kakeshita, T. Fukuda, Stable elastocaloric effect under tensile stress of iron-palladium alloy and its in situ X-ray observation, Acta Materialia 118 (2016) 88-94.

[67] Y. Xu, B.F. Lu, W. Sun, A. Yan, J. Liu, Large and reversible elastocaloric effect in dual-phase Ni54Fe19Ga27 superelastic alloys, Applied Physics Letters 106(20) (2015) 201903.

[68] Z. Yang, D.Y. Cong, X.M. Sun, Z.H. Nie, Y.D. Wang, Enhanced cyclability of elastocaloric effect in boron-microalloyed Ni-Mn-In magnetic shape memory alloys, Acta Materialia 127 (2017) 33-42.

[69] D.W. Zhao, J. Liu, X. Chen, W. Sun, Y. Li, M.X. Zhang, Y.Y. Shao, H. Zhang, A.R. Yan, Giant caloric effect of low-hysteresis metamagnetic shape memory alloys with exceptional cyclic functionality, Acta Materialia 133 (2017) 217-223.

[70] Y. Kim, M.G. Jo, J.W. Park, H.K. Park, H.N. Han, Elastocaloric effect in polycrystalline Ni50Ti45.3V4.7 shape memory alloy, Scripta Materialia 144(Supplement C) (2018) 48-51.

[71] Y. Li, W. Sun, D. Zhao, H. Xu, J. Liu, An 8K elastocaloric temperature change induced by 1.3% transformation strain in Ni 44 Mn 45− x Sn 11 Cu x

alloys, Scripta Materialia 130 (2017) 278-282.

[72] Y. Li, D. Zhao, J. Liu, Giant and reversible room-temperature elastocaloric effect in a single-crystalline Ni-Fe-Ga magnetic shape memory alloy, Sci Rep 6 (2016) 25500.

[73] B.F. Lu, F. Xiao, A. Yan, J. Liu, Elastocaloric effect in a textured polycrystalline Ni-Mn-In-Co metamagnetic shape memory alloy, Applied Physics Letters 105(16) (2014) 161905.

[74] L. Manosa, S. Jarque-Farnos, E. Vives, A. Planes, Large temperature span and giant refrigerant capacity in elastocaloric Cu-Zn-Al shape memory alloys, Applied Physics Letters 103(21) (2013) 211904.

[75] S.A. Nikitin, G. Myalikgulyev, M.P. Annaorazov, A.L. Tyurin, R.W. Myndyev, S.A. Akopyan, Giant elastocaloric effect in FeRh alloy, Physics Letters A 171(3) (1992) 234-236.

[76] H. Ossmer, C. Chluba, M. Gueltig, E. Quandt, M. Kohl, Local evolution of the elastocaloric effect in TiNi-based films, Shape Memory and Superelasticity 1(2) (2015) 142-152.

[77] H. Ossmer, C. Chluba, S. Kauffmann-Weiss, E. Quandt, M. Kohl, TiNi-based films for elastocaloric microcooling—Fatigue life and device performance, APL Materials 4(6) (2016) 064102.

[78] H. Ossmer, F. Lambrecht, M. Gultig, C. Chluba, E. Quandt, M. Kohl, Evolution of temperature profiles in TiNi films for elastocaloric cooling, Acta Materialia 81(Supplement C) (2014) 9-20.

[79] G.J. Pataky, E. Ertekin, H. Sehitoglu, Elastocaloric cooling potential of NiTi, Ni2FeGa, and CoNiAl, Acta Materialia 96(Supplement C) (2015) 420-427.

[80] C. Picornell, J. Pons, E. Cesari, Stress-temperature relationship in compression mode in Cu-Al-Ni shape memory alloys, Mater Trans 45(5) (2004) 1679-1683.

[81] S. Qian, Y. Geng, Y. Wang, T.E. Pillsbury, Y. Hada, Y. Yamaguchi, K. Fujimoto, Y. Hwang, R. Radermacher, J. Cui, Y. Yuki, K. Toyotake, I. Takeuchi, Elastocaloric effect in CuAlZn and CuAlMn shape memory alloys under compression, Philos Trans A Math Phys Eng Sci 374(2074) (2016) 20150309.

[82] Y.H. Qu, D.Y. Cong, X.M. Sun, Z.H. Nie, W.Y. Gui, R.G. Li, Y. Ren, Y.D. Wang, Giant and reversible room-temperature magnetocaloric effect in Ti-doped Ni-Co-Mn-Sn magnetic shape memory alloys, Acta Materialia 134 (2017) 236-248.

[83] M. Schmidt, A. Schutze, S. Seelecke, Elastocaloric cooling processes: The influence of material strain and strain rate on efficiency and temperature span, Apl Materials 4(6) (2016) 064107.

[84] M. Schmidt, J. Ullrich, A. Wieczorek, J. Frenzel, A. Schütze, G. Eggeler, S. Seelecke, Thermal stabilization of NiTiCuV shape memory alloys: observations during elastocaloric training, Shape Memory and Superelasticity 1(2) (2015) 132-141.

[85] W. Sun, Y. Dai, Y. Ji, P. Zhou, Y. Wan, Vessel target tracking exploiting frequency diversity for dual-frequency HFSWR, Radar (RADAR), 2016 CIE International Conference on, IEEE, 2016, pp. 1-4.

[86] J. Tusek, K. Engelbrecht, L.P. Mikkelsen, N. Pryds, Elastocaloric effect of Ni-Ti wire for application in a cooling device, J Appl Phys 117(12) (2015) 124901.

[87] E. Vives, S. Burrows, R.S. Edwards, S. Dixon, L. Mañosa, A. Planes, R. Romero, Temperature contour maps at the strain-induced martensitic transition of a Cu–Zn–Al shape-memory single crystal, Applied Physics Letters 98(1) (2011) 011902.

[88] X. Wu, Z. Suo, Y. Si, L. Meng, K. Qiu, Bulk metallic glass formation in a ternary Ti–Cu–Ni alloy system, Journal of Alloys and Compounds 452(2) (2008) 268-272.

Abstract in Korean

초 록

TiCu계 초탄성 합금 및 복합재의
마르텐사이트 상변태 거동 제어

류욱하

서울대학교 공과대학

재료공학부

형상기억합금은 가역적 마르텐사이트 상변태를 활용하여 온도, 응력장 및 자기장 변화에 따라 다양한 목적으로 활용이 가능하다. 그 마르텐사이트 상변태를 활용하는 형태의 하나로, 상변태 온도를 동작환경보다 낮추어, 응력이 가해질 때 정방향 마르텐사이트 상변태가 발생하고, 응력이 완화될 때 역방향 마르텐사이트 상변태가 발생하는 경우, 이를 초탄성이라 한다. 최근 초탄성 합금을 비정질 합금의 제2상으로 석출시켜 인성 및 가공경화 거동을 유발하려는 연구 및 상변태 시 발생하는 잠열의 출입을 통해 탄성칼로리효과를 활용하고자 하는 연구가 크게 각광받고 있다. 그러나, 기존에 이미 개발된 합금을 적용하고자 하는 연구가 주로 이루며, 특성이 최적화된 새로운 초탄성 합금 조성의 개발에 관한 연구는 미미한 실정이다. 이것은 가역 마르텐사이트 상변태를 나타내는 합금 시스템이 주로 금속간 화합물 상을 형성하기 때문에 NiTi, CuZn, 및 NiMgGa 등 소수의 특정한 합금

시스템을 기반으로 할 뿐만 아니라, 제 3, 4 합금화 원소의 고용도가 매우 제한적이기 때문에 가능한 합금 설계의 폭이 좁기 때문이다.

본 연구에서는 이러한 합금 설계 상의 한계를 극복하기 위하여 기존 합금계 상태도상에 보고된 초탄성 상(B2, BCC 등)의 조성영역을 확장할 수 있는 방안을 고안하여, 기존 합금 설계 방안으로는 제조가 불가능한 새로운 조성의 합금을 설계할 수 있는 가이드라인을 제시하였다. B2 및 BCC 등 가역 마르텐사이트 상변태를 나타내는 상은 대부분 고온 안정상으로, 특히 합금 시스템이 복잡해짐에 따라서 석출물이 발생하기 쉽다. 이 석출물을 억제하여 기지 상을 더욱 안정화 시킬 수 있으면 보다 넓은 조성 영역에서 초탄성 합금의 제조가 가능하다. 탄성칼로리효과 및 비정질 기지 복합재로서 활용이 가능하다고 알려진 NiTiCu 합금 시스템에서는 Si의 소량 첨가로 인하여 초탄성 모상인 B2상 외 기타 중간화합물 상의 석출을 효과적으로 억제할 수 있음을 규명하였다. 특히 Cu함량이 증가함에 따라서 마르텐사이트 상변태 시 발생하는 내부마찰에 의한 에너지 소산량이 감소하여 초탄성 적용에 있어 유리하므로, Cu함량을 최대한 증가시키고자 하였다. 그 결과 기존에 알려진 최대 Cu 고용도인 30at. %에서 약 13%증가한 43at. %까지 Cu를 고용시킨 초탄성 신합금을 개발하였고, 기존의 초탄성 합금과 비교하여 매우 낮은 상변태 이력 및 기계적 에너지 소산량을 나타냄을 확인하였다.

높은 Cu함량을 가지는 TiCuNiSi 초탄성 합금을 실제로 활용하기 위해서는 상변태 온도 및 기계적 특성을 최적화하는 것이 필수적인데,

본 연구에서는 Ti계 합금의 중성 원소인 Sn을 첨가하여 상변태 온도를 제어하고자 하였다. Sn은 최대 5at. %까지 B2상에 고용되었는데, 일반적인 고용현상과는 달리 매우 급격한 고용강화 경향을 나타내었다. 제 1원리 계산을 통하여 그 메커니즘이 antisite defect에 의한 강화 효과라는 것을 규명하였고, 또한 일반적인 고용강화 및 Ti합금의 고용강화 현상과 비교 분석하였다. 고용강화에 의한 상변태 온도 변화는 기계적 특성과도 관련이 있으며, 그 중 특히 응력유기 상변태의 임계응력 및 항복강도와의 상관관계를 분석하여 수식화 하였다. 이를 통해 Sn원소의 첨가량에 따른 TiCuNiSiSn 초탄성 합금의 상변태 온도 및 강도를 수식을 통하여 용이하게 제어할 수 있는 방안을 제시하였다.

Si첨가에 의한 고용한계 확장, Cu함량 증가를 통한 상변태 이력 감소, 그리고 Sn함량 제어를 통한 상변태 온도를 조절하는 과정을 거쳐 우수한 효율의 탄성칼로리효과를 나타낼 수 있는 합금 조성을 TiCuNiSiSn 합금계에서 설계하였고, 효율 및 피로 특성을 측정하였다. 그 결과, 본 연구를 통해 개발된 합금이 현재까지 보고된 모든 초탄성 합금 시스템에 비하여 가장 우수한 효율의 탄성칼로리효과를 나타내었다. 뿐만 아니라, 용해 후 주조공정만을 통해 얻어진 시편에서 전혀 석출물이 발견되지 않는 매우 우수한 B2 상 안정성을 확보할 수 있었으며, 이에 따라 압연 및 용체화 처리 등의 후 공정이 전혀 없이 벌크 시편을 제조할 수 있는 장점을 가짐을 확인하였다.

TiCuNi계 3원계 공정점 주변 조성에서는 벌크 비정질 합금의

제조가 가능하며, 이에 Si, Sn, Zr, 및 Nb등의 첨가원소를 조절하여 4mm이상의 벌크 비정질 합금설계가 가능하였다. 또한 비정질 상을 기지상으로 하고, 초탄성 B2상을 제 2상으로 하는 복합재를 개발하였고, 냉각 속도를 조절하여 제 2상의 상분율을 제어하였다. Sn첨가에 의하여 발생하는 antisite defect에 의한 고용강화 현상은 복합재 내 제 2상에도 적용할 수 있었으며, 제2상의 가공경화능이 증가함에 따라서 비정질 기지 복합재의 기계적 특성이 향상되는 상관관계를 규명하였다. 결과적으로 높은 항복강도와 약 1GPa이상의 우수한 가공경화능을 가지는 비정질 기지 복합재를 개발하였다.

이상의 연구결과를 종합할 때, 본 논문에서는 기존에 시도되지 않았던 독특한 합금 설계 방법과 이론적 고찰을 바탕으로 새로운 조성영역의 초탄성 합금을 개발하고, 그 마르텐사이트 상변태를 제어하는 방안 및 해석을 제시하였다. 이에 더 나아가 탄성칼로리효과 및 비정질 기지 복합재에 실제 적용되어 최적화된 특성을 나타내는 재료를 개발할 수 있었다. 따라서 학문적 측면뿐만 아니라 산업적 측면에서도 중요한 의미를 가지는 것으로 판단된다. 특히, 석출물 억제를 통해 상 안정성을 확보할 수 있으므로, 스퍼터링 및 3-D 프린팅을 활용하여 제 4차 산업혁명을 선도할 핵심 기술이 될 것으로 생각된다. 본 논문에서 제시한 TiCuNi 합금계뿐만 아니라, 다른 합금계에 같은 개념의 합금 설계 방안을 적용할 수 있어 후속연구를 위한 가이드라인으로 활용될 수 있을 것으로 기대된다.

,

핵심어 : 초탄성 합금, 마르텐사이트 상변태, 고용도, 고용강화, 탄성칼로리효과, 비정질기 지 복합재

학 번 : 2011-20637